UNCLASSIFIED

AD NUMBER
AD349214
CLASSIFICATION CHANGES
TO: unclassified
FROM: confidential
LIMITATION CHANGES
TO: Approved for public release, distribution unlimited
FROM: Distribution authorized to U.S. Gov't. agencies and their contractors; Administrative/Operational Use; MAR 1964. Other requests shall be referred to US Air Force Research and Technology Division, Wright-Patterson AFB, OH 45433.
AUTHORITY
AFFDL ltr, 17 Mar 1978; AFFDL ltr, 17 Mar 1978

THIS PAGE IS UNCLASSIFIED

GENERAL DECLASSIFICATION SCHEDULE

IN ACCORDANCE WITH

DOD 5200.1-R & EXECUTIVE ORDER 11652

AD 349214

RTD-TDR-63-4197
Part II

CONFIDENTIAL

Pro[illegible]edings of Sy[illegible]osium on Ae[illegible]lastic & Dy[illegible]nic Mo[illegible]ling Tech[illegible]ology

23-24-25 [illegible]TEMBER 1963
DAYTON, O[illegible]

RESEARCH &
TECHNOLOGY
DIVISION

AEROSPACE
INDUSTRIES
ASSOCIATION

63FD-193

CONFIDENTIAL

MARCH 1964

NOTICES

Qualified requesters may obtain copies of this report from the Defense Documentation Center (DDC), (formerly ASTIA), Cameron Station, Bldg. 5, 5010 Duke Street, Alexandria, Virginia, 22314.

FOREWORD

The Symposium on Aeroelastic and Dynamic Modeling Technology, sponsored by the Air Force Flight Dynamics Laboratory of the Research and Technology Division, Air Force Systems Command, in association with the Dynamics and Aeroelasticity Research Panel of the Aerospace Industries Association, was held in Dayton, Ohio, on 23-24-25 September 1963. The purposes of the Symposium were to: (a) review the state-of-the-art, (b) present the latest developments and applications for solution of current problems, (c) determine the maximum extent to which modeling techniques can be employed for efficient design and substantiation of full scale vehicle safety and reliability and (d) provide a basis for future applied research for aeroelastic and dynamic modeling technology. The symposium subject matter covers the theory, design and testing of both static and dynamic elastic models used in the development of aircraft, missiles, aerospace vehicles and equipment.

The proceedings are arranged in two parts: Part I contains the unclassified papers grouped by subject as presented, and Part II contains the classified papers and is Confidential. The authors' names and company affiliation are given at the beginning of each paper.

An effort has been made to minimize errors and omissions, however, if any serious discrepancies are noted, they should be brought to the attention of Mr. M. H. Shirk, FDDS, AF Flight Dynamics Laboratory, WPAFB, Ohio. Necessary errata sheets will be prepared and distributed.

The success of the Symposium in attaining its purposes and the subsequent compilation of this report for wide distribution as a reference document were made possible by the fine contribution of the Symposium speakers, session chairmen and authors of the technical papers. The AFFDL and the AIA gratefully acknowledge these contributions and express their appreciation.

This report is classified CONFIDENTIAL because it contains information from which performance of military weapon systems under development can be obtained, the unauthorized disclosure of which is considered prejudicial to the defense interests of the United States.

ABSTRACT

The Confidential proceedings of the Air Force Flight Dynamics Laboratory and Aerospace Industries Association Symposium on Aeroelastic and Dynamic Modeling Technology are presented in this report.

Modern day aerospacecraft requirements are calling more and more for systems which are greatly influenced by aero and thermoelastic effects. In line with this trend, model testing technology has been required to keep pace by advancing the state-of-the-art in the simulation of elastic, thermal, aerodynamic and dynamic effects. The objective of this symposium was to bring together the members of the scientific community who are intimately concerned with this area of endeavor, thereby promoting a mutual understanding of current developments and problem areas. The papers presented at the symposium were divided into appropriate technical area sub-groups and individual sessions were devoted to each. These sub-groups were: Theory and Design, Model Testing Techniques, Dynamic Loads and Aeroelastic Applications, and Structural Design Applications with two classified sessions on Aerospace Vehicle Applications and Aircraft Applications.

PUBLICATION REVIEW

The publication of this report does not constitute approval by the Air Force of the findings or conclusions contained herein. It is published only for the exchange and stimulation of ideas.

William C. Nielsen

WILLIAM C. NIELSEN
Colonel, USAF
Symposium Chairman

TABLE OF CONTENTS

PAGE

PART I

UNCLASSIFIED PROCEEDINGS

SESSION III 299

DYNAMIC LOADS AND AEROELASTIC APPLICATIONS

Chairman: Mr. Martin Goland
Southwest Research Institute

SESSION IV

STRUCTURAL DESIGN APPLICATIONS

Chairman: Mr. Howard A. Magrath
AF Flight Dynamics Laboratory

SESSION V [illegible]

LAUNCH AND AEROSPACE VEHICLE APPLICATIONS

Chairman: Dr. William R. Laidlaw
North American Aviation

AIRCRAFT APPLICATIONS

Chairman: Dr. Holt Ashley
Massachusetts Institute of
Technology

PART II

PAGE

CLASSIFIED PROCEEDINGS

CONFIDENTIAL

(U) LAUNCH AND AEROSPACE VEHICLE APPLICATIONS

(U) AIRCRAFT APPLICATIONS

SYMPOSIUM COMMITTEE ORGANIZATION

Symposia Director: Dr. John E. Keto, Chief Scientist

Symposium Chairman: Colonel William C. Nielsen, Director, AF Flight Dynamics Laboratory

Symposium Deputy Chairman: Howard A. Magrath, Chief, Vehicle Dynamics Division, AF Flight Dynamics Laboratory

Technical Committee:

Mr. E. F. Baird, Chairman, Grumman Aircraft Engineering Corp.
Mr. W. J. Mykytow, Co-Chairman, AFFDL
Mr. H. M. Davis, AFFDL
Mr. L. I. Mirowitz, McDonnell Aircraft Corp.
Mr. R. F. Hoener, AFFDL
Mr. L. A. Tolve, Lockheed Aircraft Company
Mr. M. H. Shirk, AFFDL
Mr. H. A. Wood, AFFDL
Mr. W. G. Williams, AFFDL

Arrangements Committee:

Mr. A. J. Cannon, Executive Manager, RTD
Mr. J. P. Reese, Executive Manager, AIA
Mrs. F. R. Dempsey, Secretary
Mr. J. M. Kelly, Registration and Security Manager
Mr. I. L. Schwartz, Protocol
Mr. R. C. Kahelin, Financial Manager
Mr. R. Maltby, Publicity Manager
Mr. C. High, Press Relations Manager
Mr. C. E. Sondergelt, Printing Manager
Miss M. McMurtrie, Technical Publications Manager
Mr. T. F. Cherwin, Visual Communications Manager
S/Sgt. C. R. Knifley, Chief Projectionist
Mr. R. E. Hendrickson, Transportation Manager
Capt. William F. Bozich, Senior Escort Officer

SESSION V

LAUNCH AND AEROSPACE VEHICLE APPLICATIONS

Chairman: Dr. William R. Laidlaw
North American Aviation

DYNAMIC STABILITY EQUIPMENT AND TECHNIQUES FOR TESTING AT HYPERSONIC SPEEDS*

By

L. K. Ward and R. H. Urban
von Kármán Gas Dynamics Facility
ARO, Inc.

ABSTRACT

Dynamic stability balances, both free and forced oscillation, developed at the VKF specifically for hypersonic measurements are described and discussed. Problems encountered in measuring hypersonic model damping, and their solutions, are mentioned in addition to defining areas in data reduction procedures where caution should be exercised. Data obtained on several re-entry configurations, primarily at Mach number 10, are reviewed, pointing out trends found with variation of Reynolds number, model frequency of oscillation, model amplitude of oscillation, and model geometry. Finally, areas of interest for future dynamic stability research programs are discussed.

ILLUSTRATIONS

---

*The research reported in this paper was sponsored by the Arnold Engineering Development Center, Air Force Systems Command, under Contract No. AF 40(600)-1000 with ARO, Inc. Further reproduction is authorized to satisfy needs of the U.S. Government.

NOMENCLATURE

A	Reference area $(\pi d^2/4)$, ft^2
C_m	Pitching moment/q_∞Ad
C_{m_q}	$\partial C_m/\partial(qd/2V_\infty)$, damping-in-pitch derivative, 1/rad
C_{m_α}	Slope of the pitching-moment curve, 1/rad
$C_{m_{\dot\alpha}}$	$\partial C_m/\partial(\dot\alpha d/2V_\infty)$, damping-in-pitch derivative, 1/rad
C_{y_R}	Cycles to damp to amplitude ratio R, cycles
d	Reference length (noted model diameter), ft

f	Frequency, cycles/sec
I	Mass moment of inertia, slug-ft^2
ℓn	Natural logarithm
M_∞	Free-stream Mach number
M_θ	Angular restoring-moment parameter, ft-lb/rad
$M_{\dot{\theta}}$, $M'_{\dot{\theta}}$	Angular viscous-damping parameters, ft-lb-sec/rad
q	Angular velocity
q_∞	Free-stream dynamic pressure, lb/ft^2
R	Ratio of the amplitude of a damped oscillation at a given time to the initial amplitude
Re	Reynolds number, based on model reference length, d
r_b	Model base radius, in.
r_n	Model nose radius, in.
T	Input torque, ft-lb
t	Time, sec
V_∞	Free-stream velocity, ft/sec
α	Angle of attack, rad
$\dot{\alpha}$	Time rate of change of angle of attack, rad/sec
θ	Angular displacement, rad or deg
$\dot{\theta}$	Angular velocity, rad/sec
$\ddot{\theta}$	Angular acceleration, rad/sec^2
ω	Angular frequency, rad/sec

SUBSCRIPTS

a	Atmospheric conditions
o	Maximum conditions
v	Vacuum conditions
w	Wind-on conditions

1.0 INTRODUCTION

The need to simulate the dynamic motion of proposed flight and re-entry vehicles in the supersonic and hypersonic speed regimes and thus provide data to properly evaluate the damping characteristics of such vehicles has led to the development of several dynamic stability balances at the von Kármán Gas Dynamics Facility (VKF), Arnold Engineering Development Center (AEDC), Air Force Systems Command (AFSC) for use in the supersonic and hypersonic wind tunnel facilities.

Initial development provided sting-supported, low amplitude, forced oscillation balances for use in the supersonic wind tunnels. Modification of this equipment by the addition of air and water cooling allowed testing in the hypersonic tunnels. Parallelling this hypersonic capability was the development of several free oscillation balances which provided model oscillation amplitudes ranging up to ±90 deg. Problems encountered with balance tare damping in the hypersonic speed regime prompted development of a high amplitude forced oscillation balance and a gas bearing pivot for free oscillation measurements.

Dynamic stability data have been successfully obtained for numerous test configurations in the Mach number range from 1.5 to 10 in tests sponsored by the Ballistic Systems Division (BSD) and the Aeronautical Systems Division (ASD) of the AFSC, the Army Ballistic Missile Agency (ABMA), now known as the Army Missile Command, and the National Aeronautics and Space Administrations Manned Spacecraft Center (NASA-MSC). Results of some of these test programs will be presented.

Dynamic damping data obtained in the hypersonic speed regime have indicated several areas of disagreement with the predicitions of the Newtonian impact theory (Ref. 1). These data are presented and briefly discussed along with work programs now in progress at the VKF.

2.0 APPARATUS

2.1 WIND TUNNELS

The 40-in. supersonic and 50-in. hypersonic wind tunnels are closed-circuit, variable density wind tunnels, whereas the 12-in. supersonic and 12-in. hypersonic wind tunnels are of the intermittent, variable density type.

The 40-Inch Supersonic Tunnel (A) (Fig. 1) has a flexible-plate-type nozzle which is automatically controlled to produce Mach numbers from 1.5 to 6. The tunnel operates at maximum stagnation pressures ranging from 29 to 200 psia at $M_\infty = 1.5$ to 6, respectively, and at stagnation temperatures up to 300°F ($M_\infty = 6$). Minimum operating pressures are about one-tenth of the maximum.

The 50-Inch Mach 8 Tunnel (B) (Fig. 2) and the 50-Inch Mach 10 Tunnel (C) (Fig. 3) have contoured axisymmetric nozzles. Tunnel B operates at stagnation pressures ranging from 100 to 900 psia and at stagnation temperatures up to 900°F. Tunnel C operates at stagnation pressures ranging from 200 to 2000 psia and at stagnation temperatures up to 1450°F.

The 12-Inch Supersonic Tunnel (D) (Fig. 4) has a manually adjusted, flexible-plate-type nozzle. The tunnel operates at Mach numbers from 1.5 to 5, at stagnation pressures from about 5 to 60 psia, and at stagnation temperatures of about 80°F.

The 12-Inch Hypersonic Tunnel (E) (Fig. 5) has a nozzle formed by manually adjusted contoured throat blocks and flexible plates. The tunnel operates at Mach numbers from 5 to 8 at maximum stagnation pressures from 400 to 1600 psia, respectively, and at stagnation temperatures up to about 940°F.

A complete description of the tunnels and airflow calibration information may be found in Ref. 2.

2.2 DYNAMIC BALANCES

Several one-degree-of-freedom dynamic balances are available at the VKF and are summarized in Table. 1. Both the free oscillation and forced oscillation techniques are used for measuring the damping-in-pitch or damping-in-yaw derivatives.

2.2.1 Forced Oscillation

Figure 6 shows the sting-balance assembly of the low amplitude, forced oscillation balance. In the case of the high amplitude, forced oscillation balance the identical sting support system is used. Each system is forced to oscillate through linkage by an electromagnetic shaker motor located in the enlarged portion of the sting. The low amplitude (±3 deg) system (Fig. 7) uses a cross-flexure pivot which provides exceptionally low values of structural damping. The angular displacement of the model is measured by the use of a strain-gage bridge mounted on a cross-flexure. The input torque to the system is measured with a strain-gage bridge mounted on the torque beam (Fig. 7); hence, the damping torque contributed by the shaker motor, push rod, and linkage assembly is not measured.

The high amplitude (±12 deg), forced oscillation balance (Fig. 8) has an oscillating shaft, supported by two angular contact bearings, for the model pivot axis. The bearings are spring loaded axially to eliminate bearing free-play. The shaft is forced to oscillate by a flexure-connected push rod which is driven by the shaker motor previously mentioned. The push-rod-to-shaft connection is made by means of a small flexure, thus eliminating the use of pin joints. Removable I-beam section torque members are connected to the shaft on the model side of the bearings and support the model mounting bulkhead. Balance restoring moments are produced by the two tapered beams which are fixed to the sting and connected to the model mounting bulkhead by two sets of flexures. Points B are the attachment points of one set of flexures to the bottom restoring-moment beam, and points B′ are the attachment points of these flexures to the model mounting bulkhead. This connecting flexure arrangement was designed to minimize the high stress levels that are present in flexures of a shorter length when forced to bend through the large displacement angles required in this system. View AA shows the balance displaced 12 deg. Model angular displacement is measured with a strain-gage bridge mounted on the restoring-moment beam, and the input torque to the system is measured by a strain-gage bridge mounted on the "I" section of the torque member.

Both forced oscillation balance systems are equipped with an electronic feedback control system (Ref. 3) to provide positive amplitude control for either dynamically stable or unstable models.

2.2.2 Free Oscillation

Several free oscillation balances have been developed at the VKF capable of both low and high amplitude measurements. Both cross-flexures and bearings have been used as the pivot. Ball bearings may be used at the lower Mach numbers for configurations having a sizable amount of damping, but their adverse damping characteristics make ball bearings unsuitable for hypersonic measurements.

Because of the need for a more feasible free oscillation pivot, a gas bearing (Ref. 4) was developed at the VKF.

Figure 9 shows a sketch of the bearing, and as may be noted, the plenum is located in the fixed portion of the assembly and the gas escapes through eight equally spaced orifices to "float" the outer ring to which the model may be attached. The bearing will easily support a 300-lb axial load at a plenum pressure of 300 psig and may be sting mounted or mounted by a transverse rod support to allow free oscillation measurement of model damping. The tare damping of the bearing is extremely low, as may be seen by inspection of Fig. 10 which shows that for a typical re-entry configuration at $M_\infty = 10$ the gas bearing damping is two orders of magnitude lower than the tare damping of a cross-flexure pivot. The gas bearing balance, when mounted on a sting support, is restricted in oscillation amplitude only by the model's physical size with respect to the bearing. By supporting the bearing on a transverse rod, there are no amplitude restrictions on the model, as may be seen in Fig. 11.

The angular transducer (Fig. 12) designed for the bearing is similar to the one used in previous VKF free-oscillation balances. The transducer simply consists of an eccentric mounted on the movable portion (outer ring) of the bearing and the two "E" cores mounted 180 deg apart and over the eccentric. As the bearing is rotated, the air gap between the eccentric and the coils in the "E" cores changes and produces an analog signal proportional to the angular displacement. No torque is produced by the transducer.

3.0 PROCEDURE

3.1 FORCED OSCILLATION

The motion of a single-degree-of-freedom, forced oscillation system may be defined by the equation

$$I\ddot{\theta} - M_{\dot{\theta}}\dot{\theta} - M_{\theta}\theta = T \cos \omega t \qquad (1)$$

It may readily be shown that, for constant amplitude motion at the undamped natural frequency of the model-balance system, the required forcing torque ($T \cos \omega t$) is precisely equal to the damping torque ($M_{\dot{\theta}}\dot{\theta}$). The method for computing the dimensionless damping-in-pitch derivatives for constant amplitude, forced oscillation tests is as follows:

$$M_{\dot{\theta}}\dot{\theta} = T \cos \omega t \text{ (at the undamped natural frequency of the system)} \qquad (2)$$

$$M_{\dot{\theta}}\theta_o\omega = T \qquad (3)$$

$$M_{\dot{\theta}} = T/\theta_o\omega \qquad (4)$$

$$M'_{\dot{\theta}} = M_{\dot{\theta}_w} - M_{\dot{\theta}_v} \cdot \omega_v/\omega_w \qquad (5)$$

$$C_{m_q} + C_{m_{\dot{\alpha}}} = M'_{\dot{\theta}} \cdot 2V_\infty/q_\infty Ad^2 \qquad (6)$$

The expression for obtaining the aerodynamic viscous damping parameter $M_{\dot{\theta}}$ is based on the fact that the structural damping of a flexure pivot varies inversely with the frequency of oscillation, as was shown by Welsh and Ward in Ref. 5. Further experiments at the VKF have revealed that all pivot systems investigated, having structural stiffness, have this inverse relationship with frequency.

All forced oscillation balance systems are equipped with transducers which provide continuous time resolved outputs which are proportional to the model oscillation amplitude and input torque of the system. The signals are digitized by a Beckman 210 high-speed digitizer and relayed to an IBM 7070 computer for data reduction.

Operation of balances in the hypersonic tunnels requires that balance and balance support assembly be adequately cooled to withstand the necessarily high stagnation temperatures. Water jackets provide sufficient cooling for the balance supports; however, water may not be used to cool the balance since the structural damping of the system would be affected. Cooling of the balance has been done with the use of high pressure air sprays directed on the model attachment bulkhead, as indicated in Fig. 13. The cooling air is turned off during time periods when data are being obtained. In the case of tunnel C the model is retracted from the airflow during the air cooling periods.

As indicated by Eq. (5), structural damping values are evaluated at vacuum conditions. This is done to eliminate the still-air contribution encountered at atmospheric conditions. Normally, the still-air contributions may be ignored when testing at the lower Mach numbers ($M_\infty < 4$) but must be considered when testing at the higher Mach numbers because the results will be in error, as is indicated in Fig. 14.

3.2 FREE OSCILLATION

The equation of motion of a model suspended in an airstream and restricted to one degree of freedom and small amplitudes can be written as

$$I\ddot{\theta} - M_{\dot{\theta}}\dot{\theta} - M_\theta\theta = 0 \qquad (7)$$

This equation, of course, is true only for a completely linear system with viscous damping. The damping parameter for motion defined by Eq. (7) can be written as

$$M_{\dot{\theta}} = \frac{2If\ell nR}{C_{yR}} \tag{8}$$

From this expression it is seen that, knowing the model moment of inertia, it is only necessary to determine the number of cycles to damp to a given ratio (C_{yR}) and the frequency of oscillation (f) to evaluate the damping parameter $M_{\dot{\theta}}$.

In a true, viscous, damped system the amplitude of the motion will decrease exponentially, e.g., a plot of the natural logarithm of the envelope curve against cycles of oscillation will be linear. In reducing data for models oscillating over large amplitudes and subject to non-linearities, it is necessary to ensure that the amplitude range can be approximated by the linear expression in Eq. (8).

In the case of ball bearing damping, the procedures for evaluating their damping characteristics is given in Ref. 6. After the damping has been evaluated at the proper frequency and amplitude, the subtraction may be made from the wind-on value to yield the aerodynamic value.

To this point it has been assumed that the model balance system has no structural stiffness. In the case where structural stiffness is present the aerodynamic value must be determined as follows

$$M'_{\dot{\theta}} = 2I\ell nR[(f/C_{yR})_w - (f/C_{yR})_v \cdot f_v/f_w] \tag{9}$$

This expression provides the necessary correction for the variation of structural damping with frequency as previously discussed.

Most free oscillation measurements to be made in the future will be made using the gas bearing pivots; therefore, the balance tare damping will be extremely low and in most cases may be ignored.

As with the forced oscillation systems the full data reduction may be done on the IBM 7070. Cooling of the free oscillation equipment is also handled in the manner previously described.

4.0 EXPERIMENTAL RESULTS

Numerous dynamic stability test programs have been conducted at the VKF over the past several years on ballistic re-entry vehicles, and, in general, results obtained at the higher Mach numbers have agreed reasonably well with the Newtonian impact theory (Ref. 1). In addition, no appreciable effect was found on the damping derivatives which was attributable to changing the reduced frequency parameter ($\omega d/2V_\infty$). Tests conducted on a model of the Pershing re-entry vehicle configuration (Ref. 7) in the 12-Inch Hypersonic Tunnel (E) showed excellent agreement with impact theory, as may be noted in Fig. 15.

Data obtained on models of a typical, second generation re-entry vehicle in the VKF tunnels A, B, D, and E at Mach numbers 4 through 8 are presented in Fig. 16. The reduced frequency parameter, $\omega d/2V_\infty$, was varied by changing both model scale and frequency and ranged from 0.0039 to 0.007. No apparent effect was noted. A point of interest here is that, in order to produce a dynamically stable configuration at the lower Mach numbers, nose roughness was needed to provide a turbulent boundary layer and eliminate the flow separation on the cylinder caused by the 10-deg flare.

Investigations of three model configurations of the Skybolt re-entry vehicle at Mach 10 in the 50-Inch Mach 10 Tunnel (C) (Ref. 8) indicated a pronounced Reynolds number effect (Fig. 17). During the tests the distance from the model base forward to the pivot axis was held constant while the model nose radius was varied. The impact theory for Models A, B, and C shown in the band did predict a reduction in stability with increasing nose radius although not of the magnitude found by experiment. The theory should become increasingly valid as Reynolds number increases, yet the disagreement with the experimental data is the greatest at the higher Reynolds numbers.

In a more recent test program, damping derivatives were measured on a proposed re-entry vehicle and variations caused by Reynolds number, angle of attack, and model oscillation frequency were investigated for low oscillation amplitudes (±2 deg) at Mach number 10 in Tunnel C. Data were obtained at model frequencies ranging from about 4 to 18 cycles per second and over the full Reynolds number range of the tunnel. These data are reported in full in Ref. 9, and the zero angle-of-attack values are presented in Fig. 18. As may be noted, the higher value of $C_{m_q} + C_{m_{\dot{\alpha}}}$ occurs at the lowest Reynolds number and the highest oscillation frequency and is an order of magnitude higher than data obtained at the reverse of these conditions. These data show that, for values of $\omega d/2V_\infty \leq 0.0019$, Reynolds number has no appreciable effect on the damping derivatives. As $\omega d/2V_\infty$ is increased above 0.0019 the damping derivatives increase and, in addition, increase with decreasing Reynolds number. The dotted line, representing a "plane" corresponding to the impact theory, shows fair agreement at all Reynolds numbers corresponding to values of $\omega d/2V_\infty \leq 0.0019$.

It should again be pointed out that the above variations with the reduced frequency parameter ($\omega d/2V_\infty$) were made by holding the model scale (d) constant and the free-stream velocity (V_∞) essentially constant. Additional experiments should be conducted to determine if the abovementioned trends with $\omega d/2V_\infty$ are valid for conditions where model frequency is held constant and geometry is varied.

5.0 FUTURE TEST PROGRAMS

In a continuing effort to provide necessary test equipment for use in obtaining dynamic damping data at the VKF, several internal development programs have been initiated. One such program proposes the measurement of model damping by obtaining continuous, time-resolved, model surface pressures on a model oscillating at constant oscillation amplitudes. Data will be obtained at amplitudes ranging from ±2 to ±10 deg with initial testing being done in the tunnel A facility at Mach 4. Variable reluctance, dual coil, pressure transducers, as described in Ref. 2, will be used and will be located at the model surface to minimize lag times.

The effects of ablation on the aerodynamic characteristics of re-entry vehicles has prompted the study of a method to provide damping data using mass injection at the model surface. Investigations are currently being conducted to determine a means of transporting the mass across the balance pivot axis without appreciably effecting the tare damping.

6.0 SUMMARY

A relatively large selection of test equipment is available at the VKF for obtaining model damping data at Mach numbers ranging from 1.5 through 10. Both the free oscillation and the forced oscillation techniques are employed. The models may be supported by either a sting or a transverse rod. Experimental dynamic stability data obtained at hypersonic speeds point out the inadequacies in the present-day theory and indicate the need for continued wind tunnel investigations in support of the development of proposed flight and re-entry vehicles.

REFERENCES

1. Fisher, Lewis R. Equations and Charts for Determining the Hypersonic Stability Derivatives of Combinations of Cone Frustums Computed by Newtonian Impact Theory. NASA TN D-149, November 1959.

2. Test Facilities Handbook (5th Edition). "von Kármán Gas Dynamics Facility, Vol. 4." Arnold Engineering Development Center, July 1963.

3. Welsh, C. J., Hance, Q. P., and Ward, L. K. A Forced-Oscillation Balance System for the von Kármán Gas Dynamics Facility 40- by 40-Inch Supersonic Tunnel. AEDC-TN-61-63, May 1961.

4. Hodapp, A. E. Evaluation of a Gas Bearing Pivot for a High Amplitude Dynamic Stability Balance. AEDC-TDR-62-221, December 1962.

5. Welsh, C. J. and Ward, L. K. Structural Damping in Dynamic Stability Testing. AEDC-TR-59-5, February 1959.

6. Welsh, C. J., Ledford, R. L., Ward, L. K., and Rhudy, J. P. Dynamic Stability Tests in Hypersonic Tunnels and at Large Model Amplitudes. AEDC-TR-59-24, December 1959.

7. Ashmush, G. R. and Ward, L. K. (U) Dynamic Stability Tests of a 0.074-Scale Model of a Pershing Missile Re-Entry Configuration at Hypersonic Speeds. AEDC-TN-60-200, October 1960.. (Confidential Report)

8. Ward, L. K. and Hodapp, A. E. (U) Dynamic Stability Tests on Three Models of the Skybolt Re-Entry Vehicle at Mach 10. AEDC-TDR-62-95, May 1962. (Confidential Report)

9. Ward, L. K., Hodapp, A. E., and Uselton, B.L. (U) "Dynamic Stability Tests on a 0.217-Scale Model of the CS-1FT Re-Entry Vehicle at Mach 10." AEDC-TDR-63-98, May 1963. (Confidential Report)

Table 1
Summary of Balances Currently Available for Dynamic Stability Testing

Balance Designation	Balance Type	AEDC-VKF Tunnel Use	Amplitude Range, deg	Pivot Type	Pivot Support	Restoring Moment, in.-lb/deg
1 Small Amplitude	Forced or Free Oscillation	40-Inch Supersonic	±1 → ±3	Cross Flexure	Sting	9.75, 25.5, 51.1, 177.0*
2 Small Amplitude	Forced Oscillation	40-Inch Supersonic 50-Inch Mach 8 50-Inch Mach 10	±1 → ±3	Cross Flexure	Sting	15.4, 30.0, 96.2, 224*
3 Large Amplitude	Forced Oscillation		±1 → ±12	Ball Bearing	Sting	22.4*
4 Large Amplitude	Free Oscillation		±3 → ±20	Ball Bearing	Sting	Function of Model Moment of Inertia and C_{m_α}
5 Transverse Rod	Free Oscillation	50-Inch Mach 8	±5 → ±180	Ball Bearing	Transverse Rod	
6 Large Amplitude	Free Oscillation	40-Inch Supersonic 50-Inch Mach 10	±1 → ±12	Gas Bearing	Sting	
7 Large Amplitude	Free Oscillation	40-Inch Supersonic 50-Inch Mach 10	±5 → ±180	Gas Bearing	Transverse Rod	

*Maximum Values

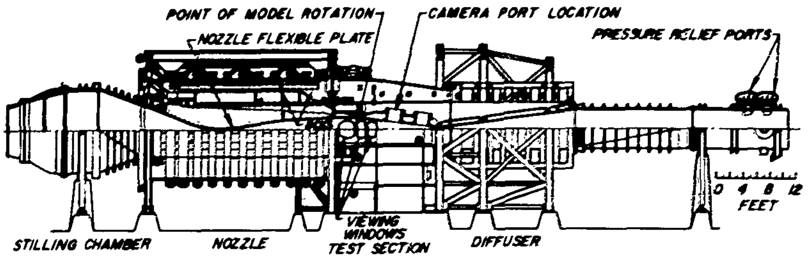

Assembly

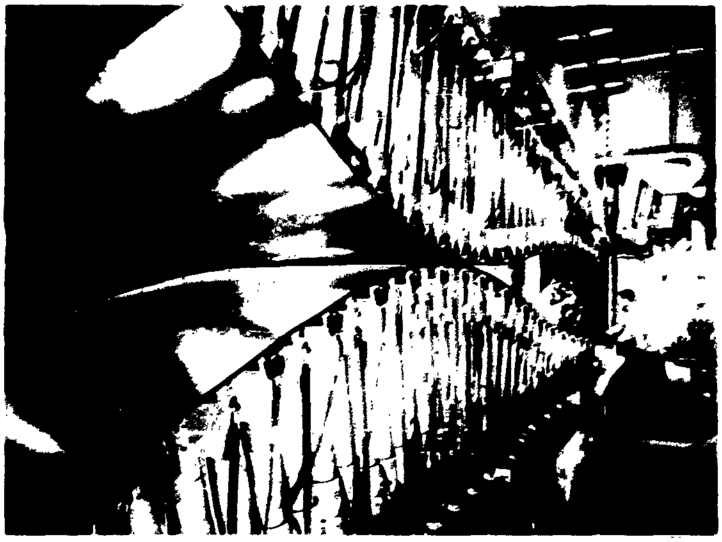

Nozzle and Test Section

Fig. 1 The 40-Inch Supersonic Tunnel (A)

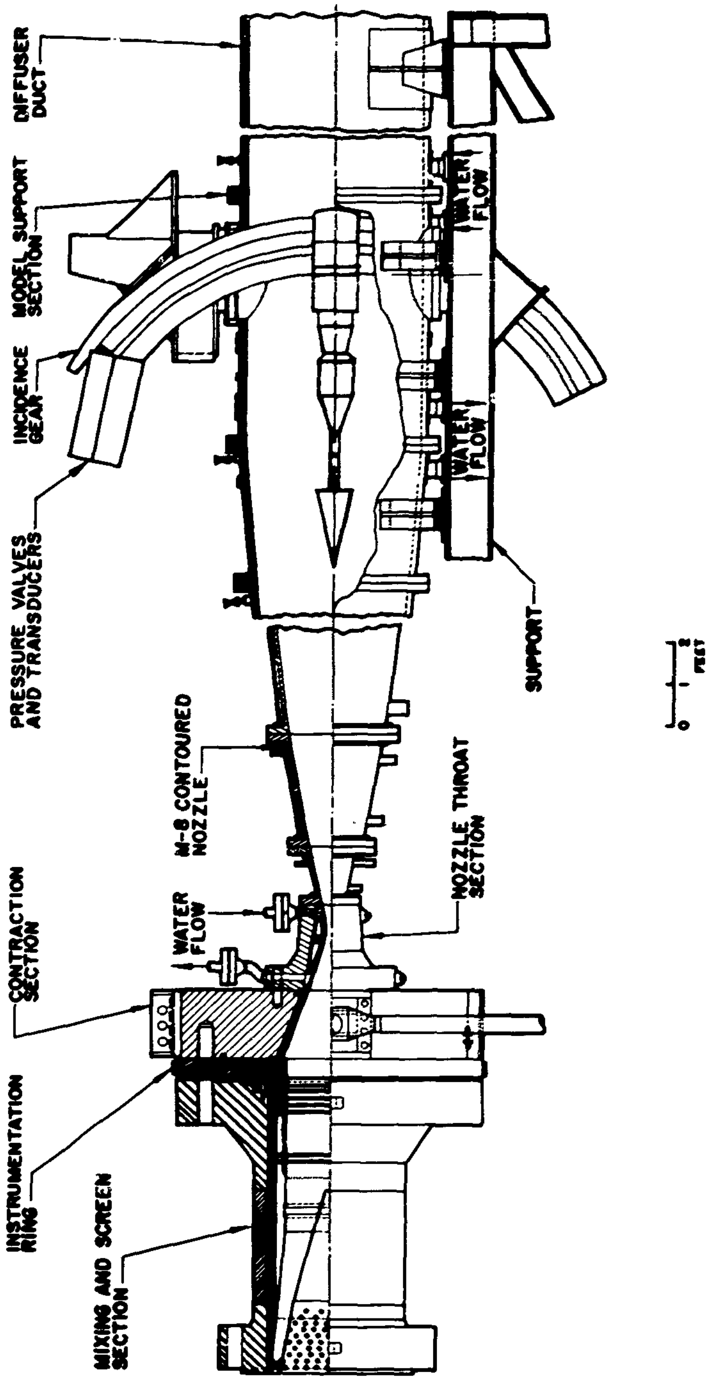

Fig. 2 The 50-Inch Mach 8 Tunnel (B)

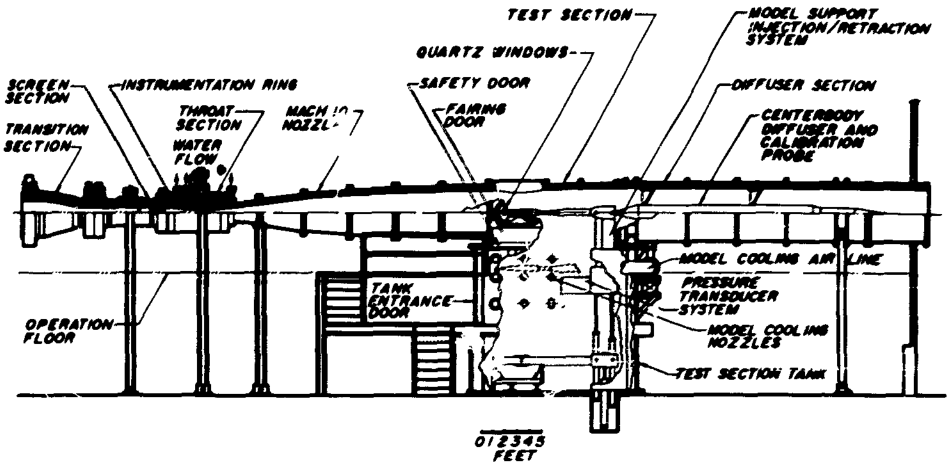

Tunnel Assembly

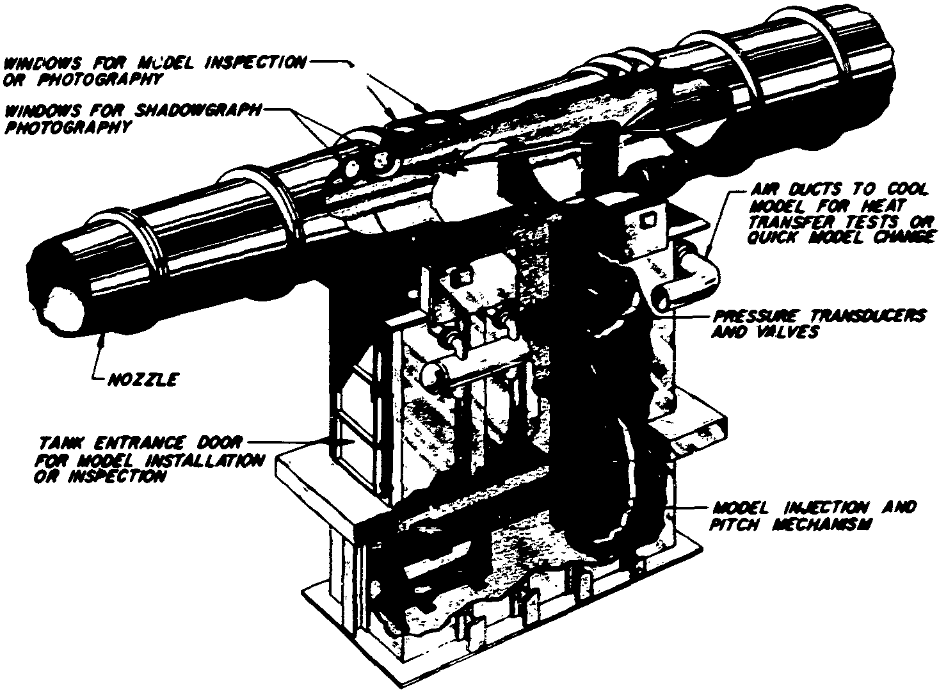

Tunnel Test Section

Fig. 3 The 50-Inch Mach 10 Tunnel (C)

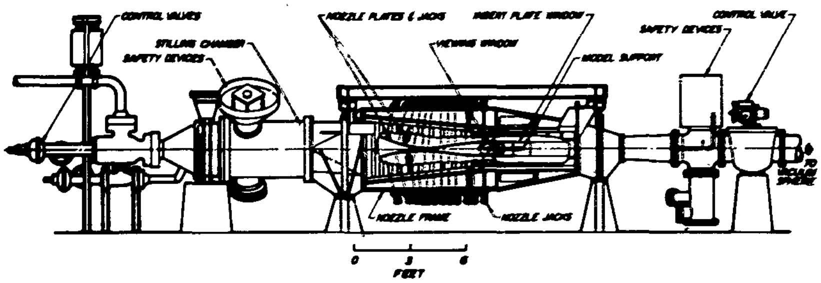

Assembly

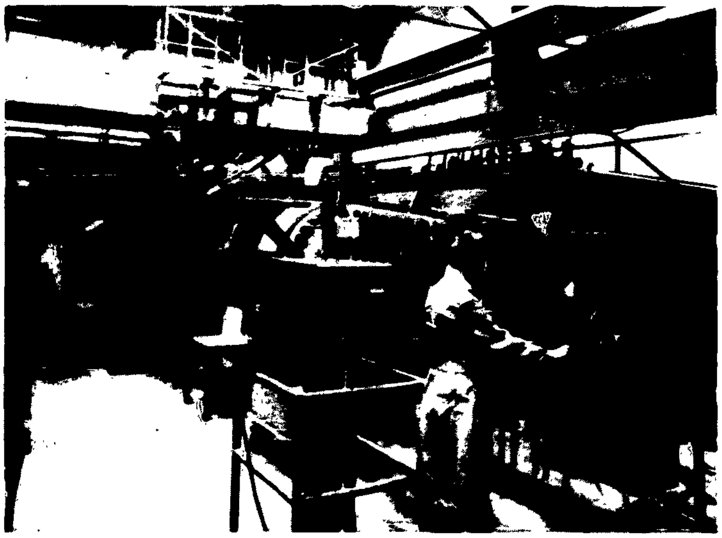

Nozzle and Test Section

Fig. 4 The 12-Inch Supersonic Tunnel (D)

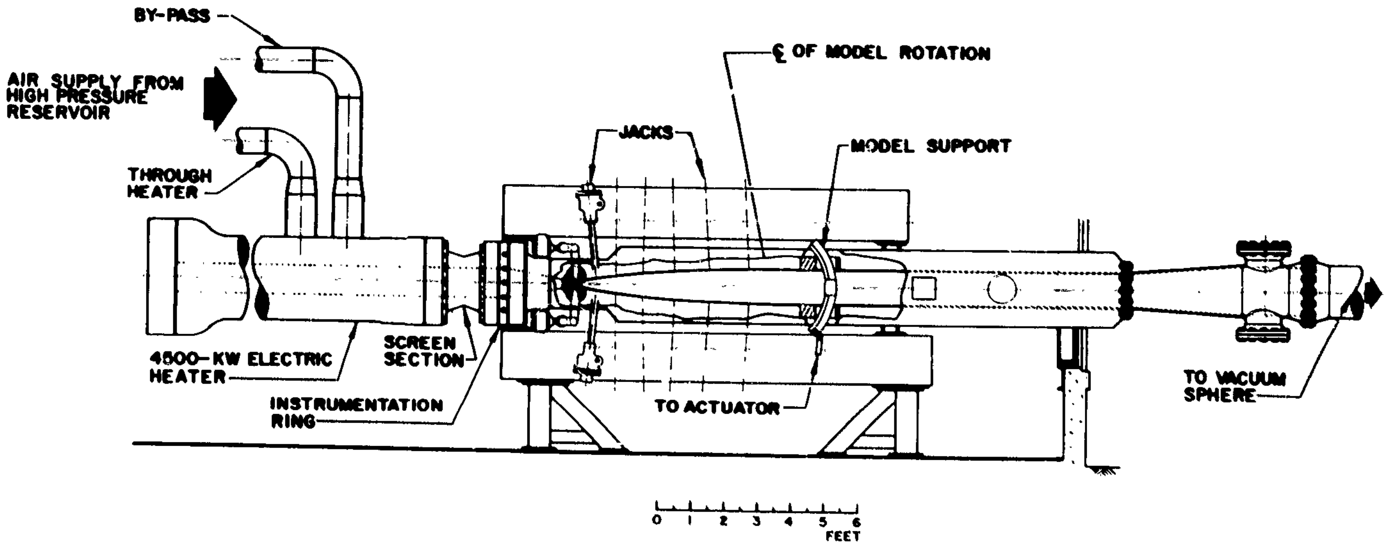

Fig. 5 The 12-Inch Hypersonic Tunnel (E)

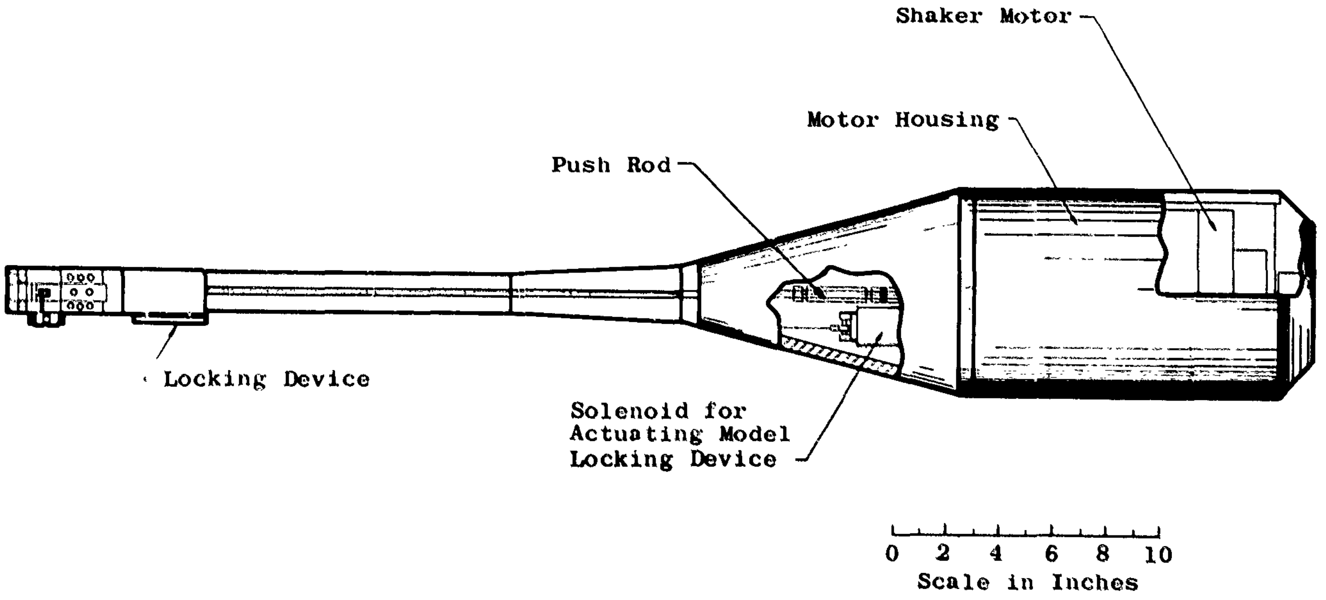

Fig 6 Sting Balance Assembly of the Low Amplitude Forced Oscillation Balance

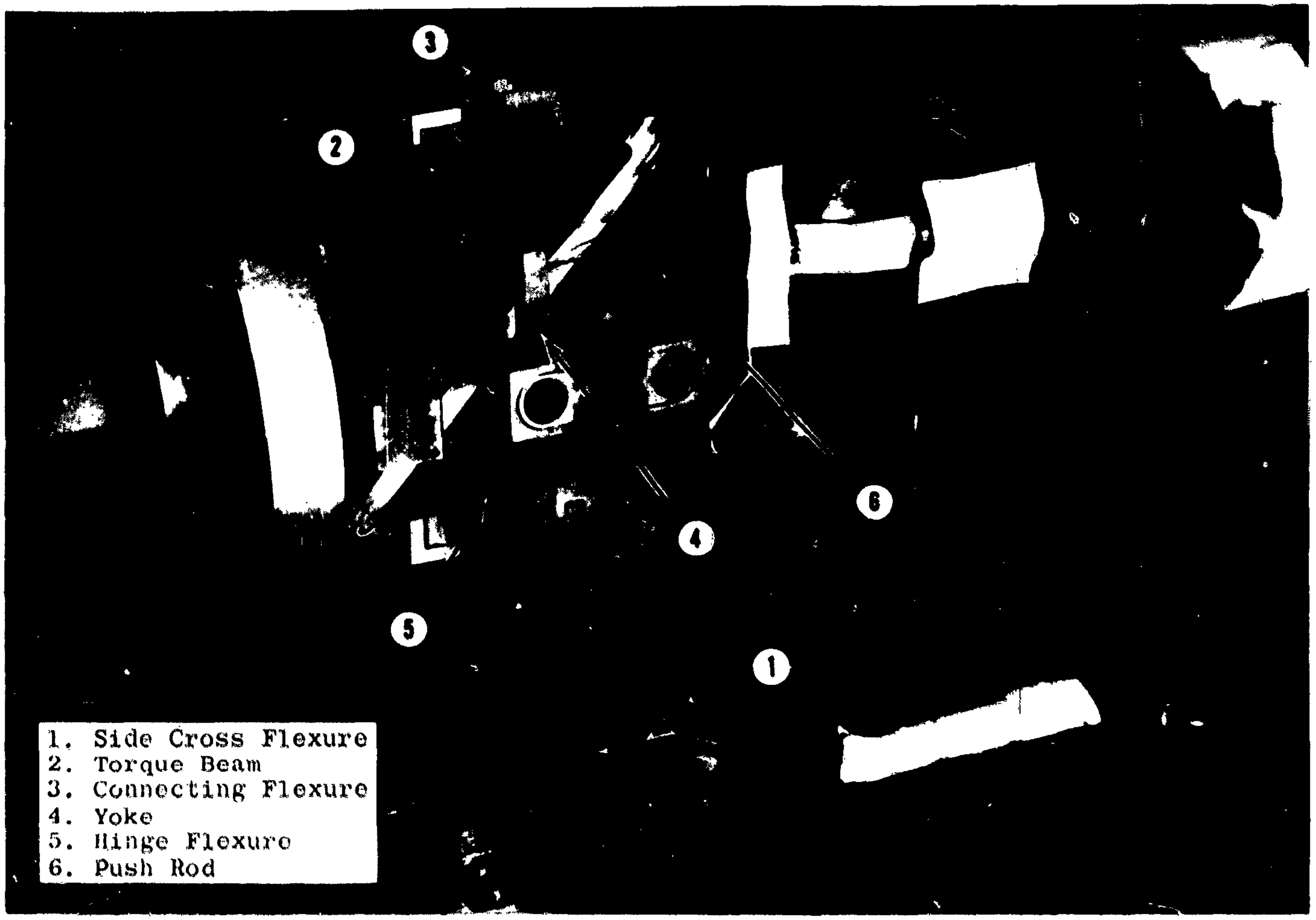

1. Side Cross Flexure
2. Torque Beam
3. Connecting Flexure
4. Yoke
5. Hinge Flexure
6. Push Rod

Fig. 7 Small Amplitude Forced Oscillation Balance

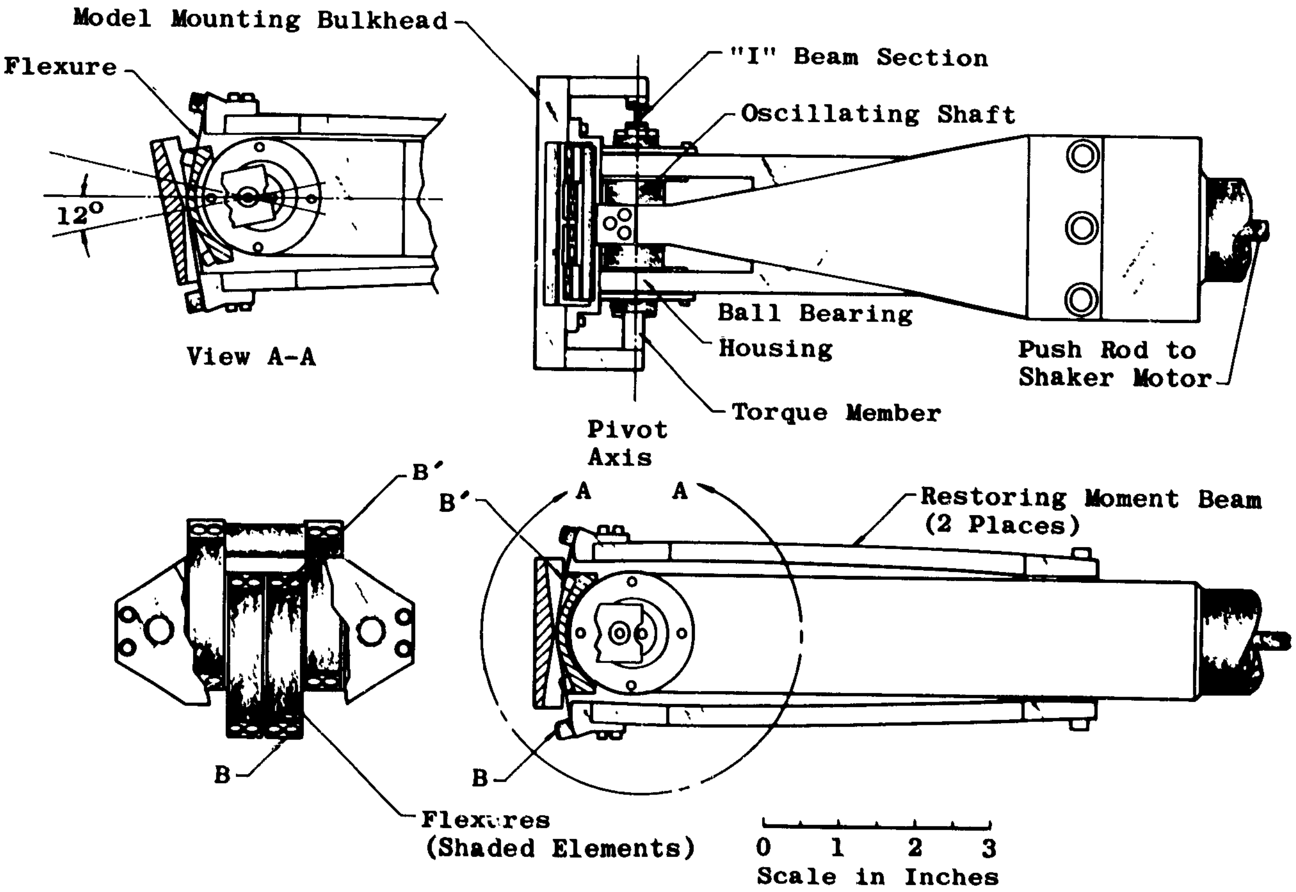

Fig. 8 Sketch of the High Amplitude Forced Oscillation Balance

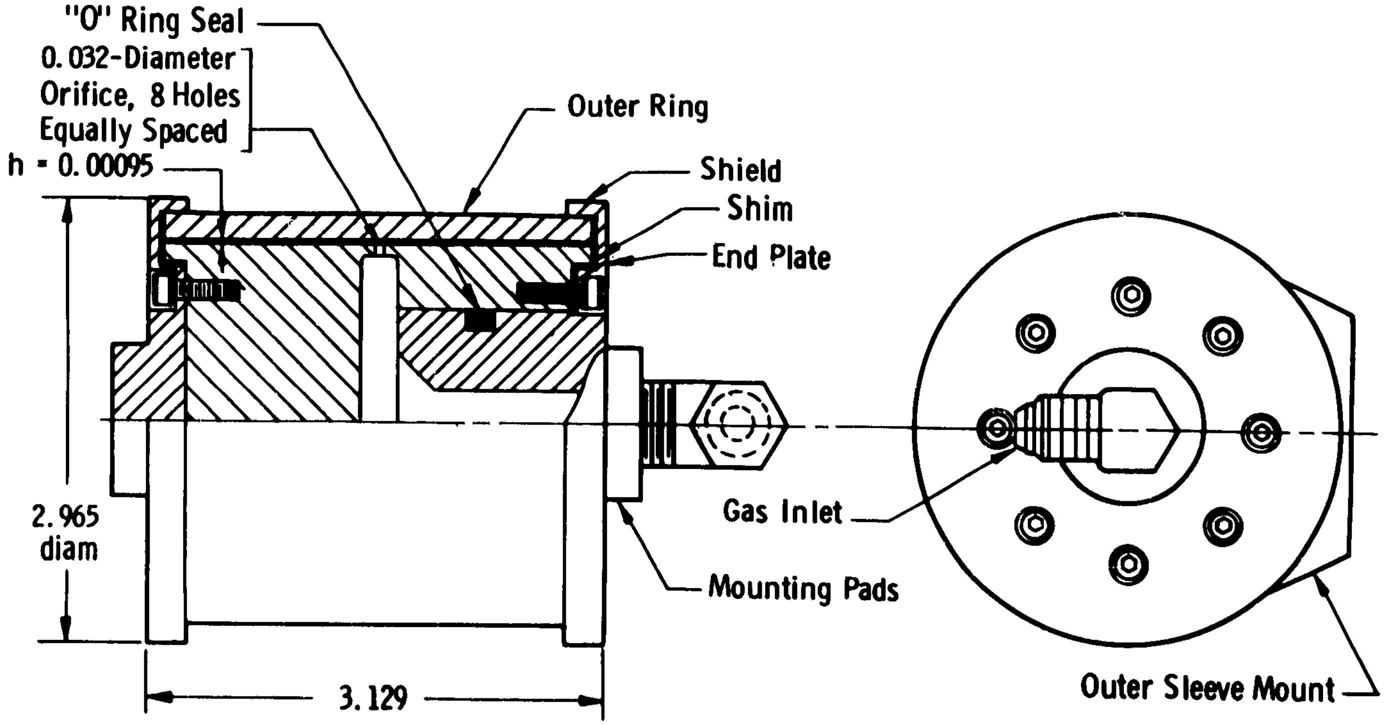

All dimensions in inches

Fig. 9 Sketch of the Gas Bearing

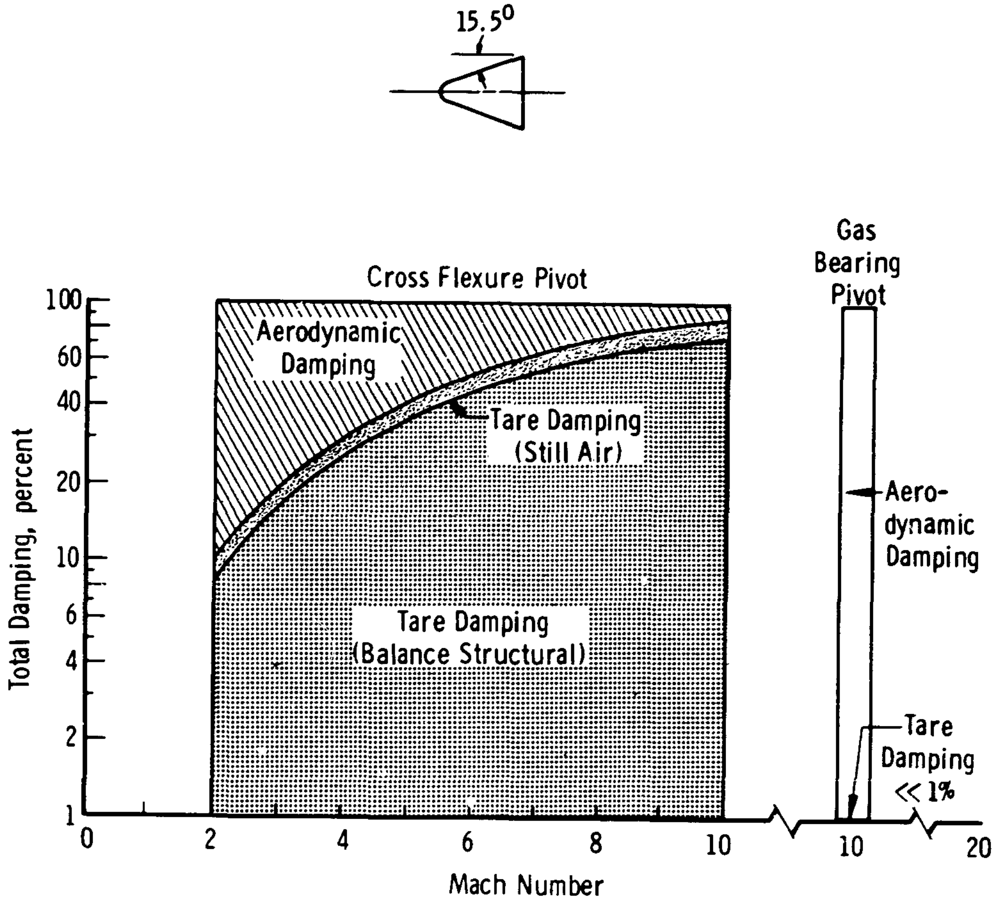

Fig. 10 Variation of Total System Damping versus Mach Number

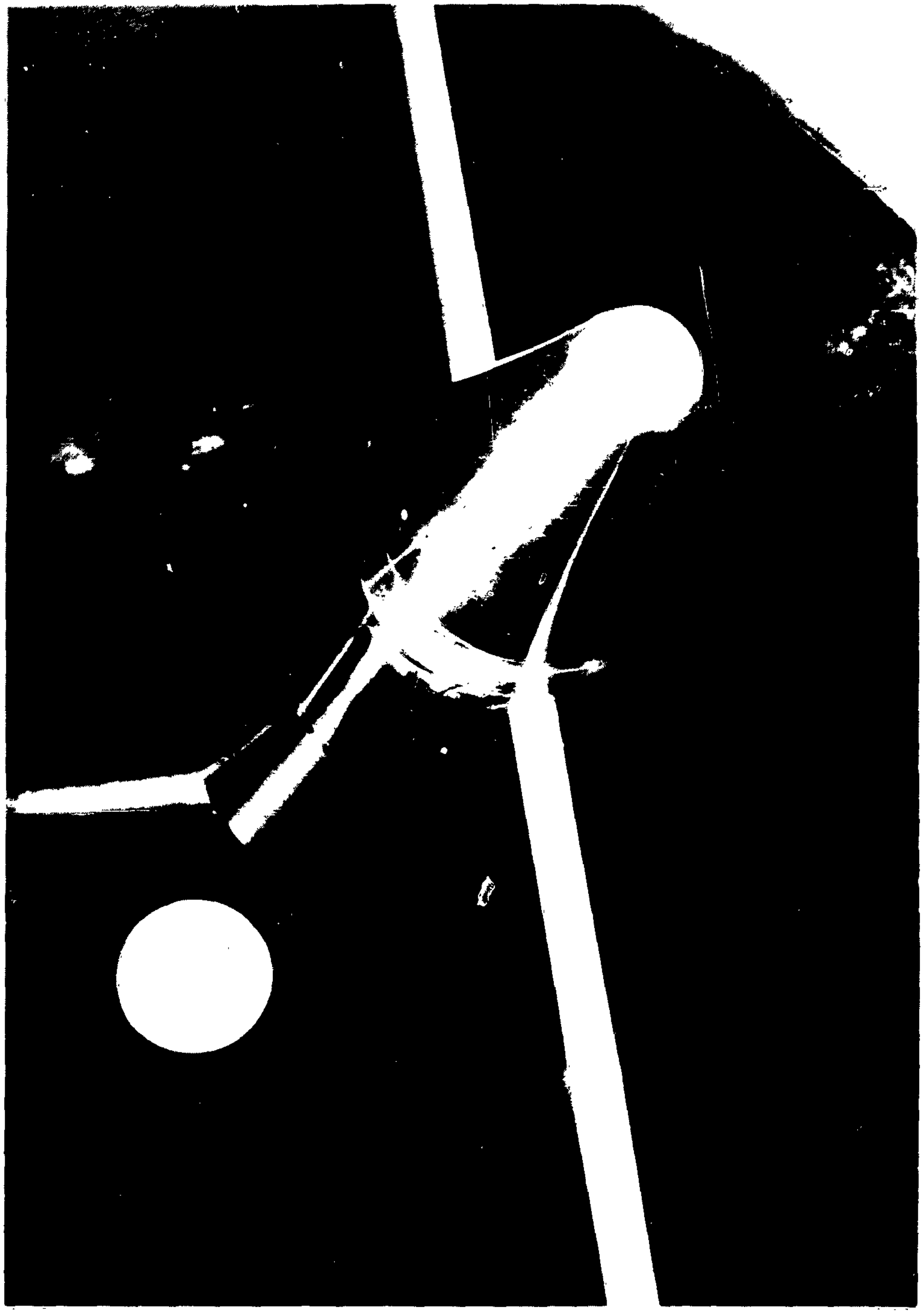

Fig. 11 Bearing Pivot, Free Oscillation, Transverse Rod Supported Balance System, Mounted in the 50-Inch Mach 8 Tunnel (B)

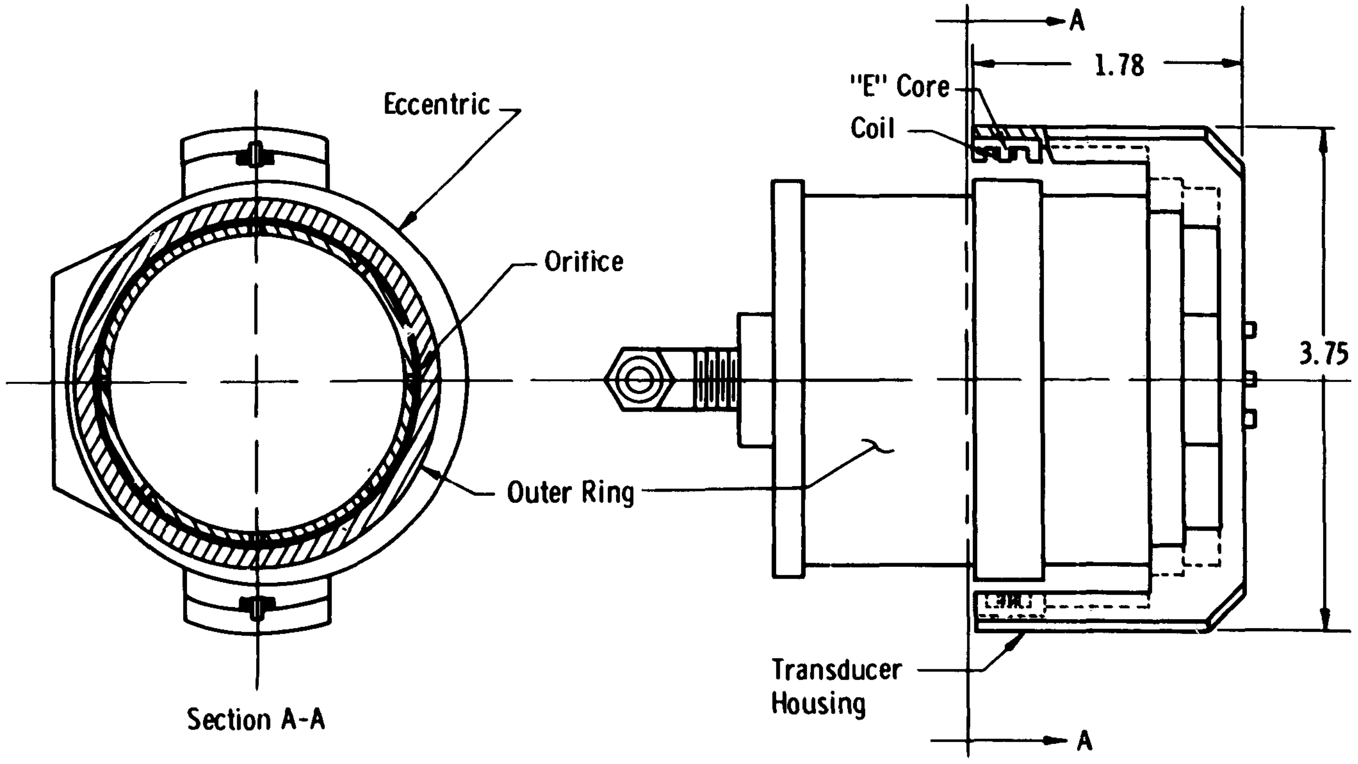

All dimensions in inches

Fig. 12 Angular Transducer Bearing Assembly

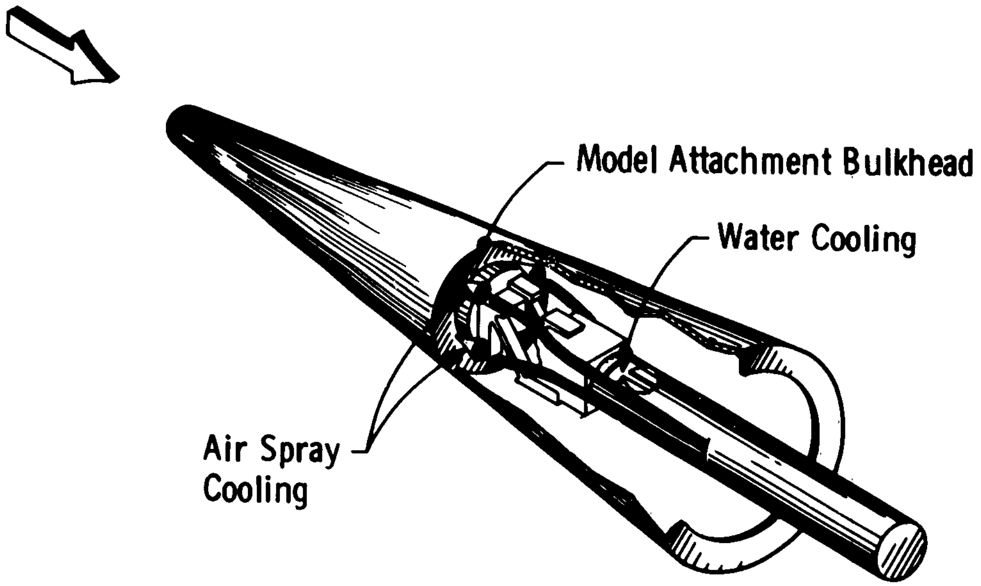

Fig. 13 Cooling of Model Balance Systems for Hypersonic Dynamic Stability Measurements

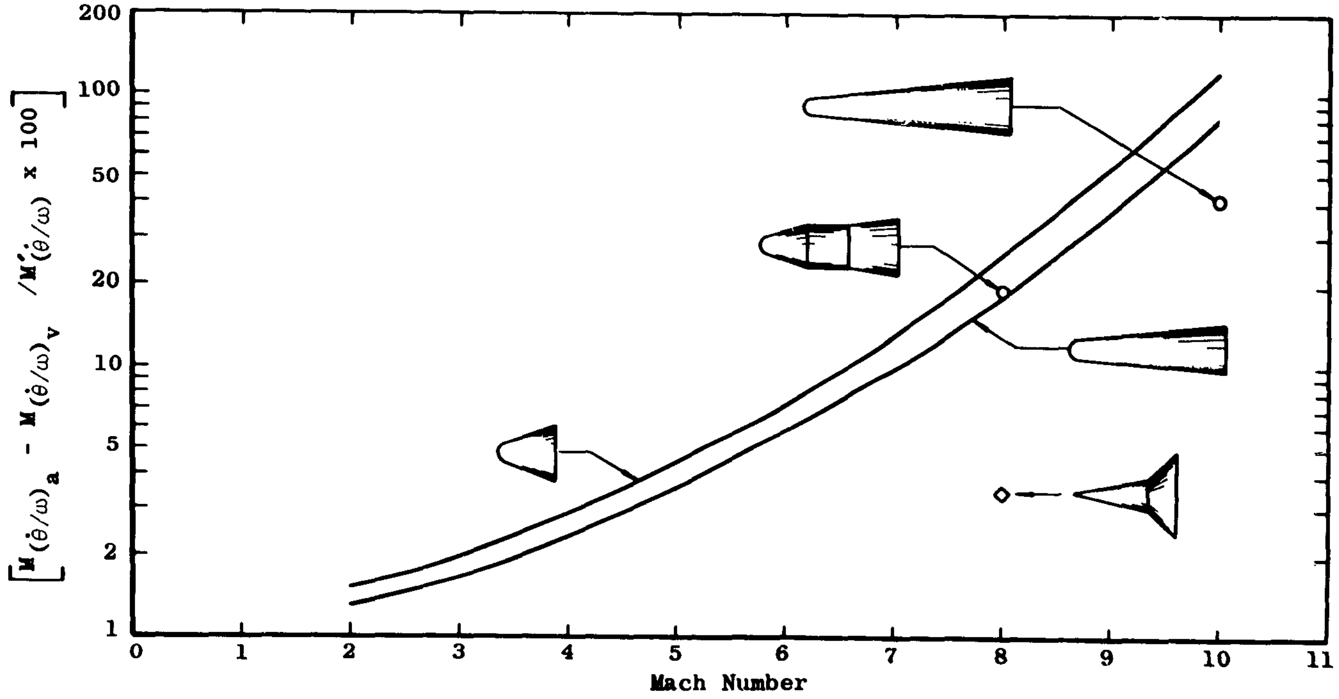

Fig. 14 Variation of the Ratio of Model Still-Air Damping to Model Aerodynamic Damping with Mach Number

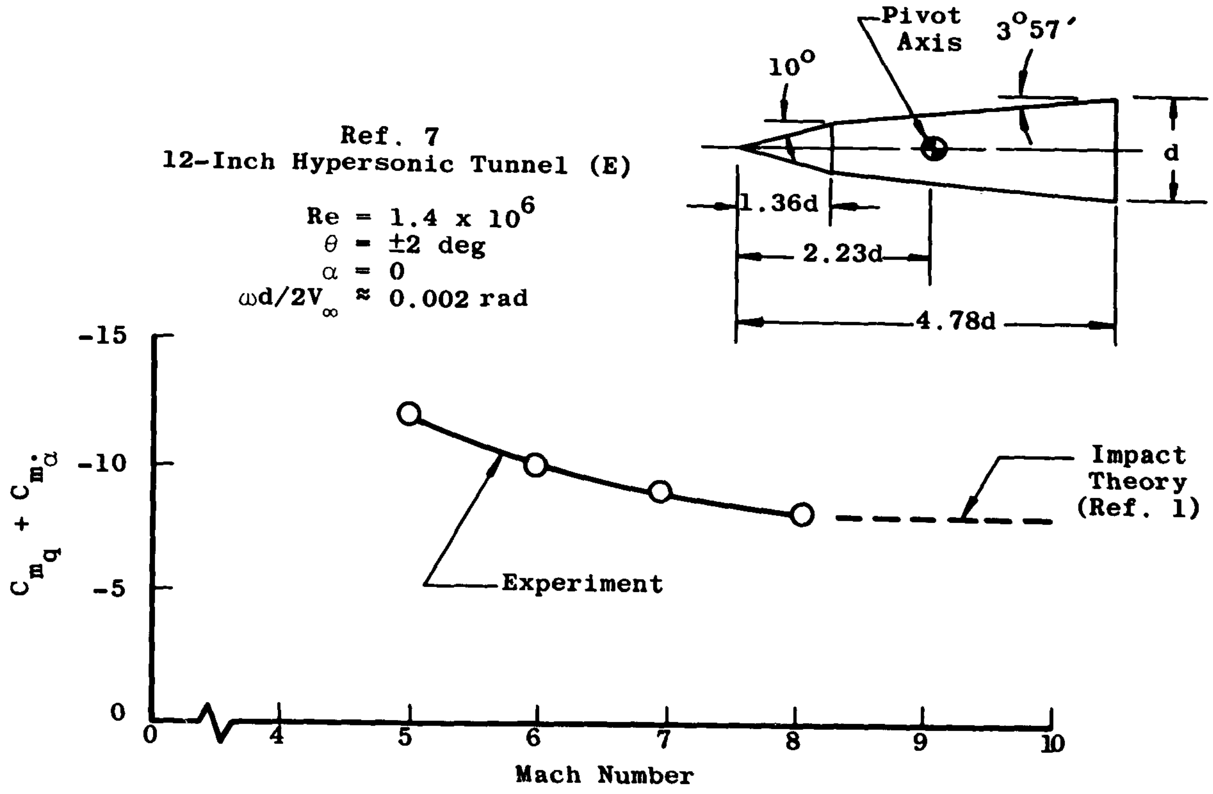

Fig. 15 Variation of the Damping-in-Pitch Derivatives with Mach Number for the Pershing Re-entry Vehicle

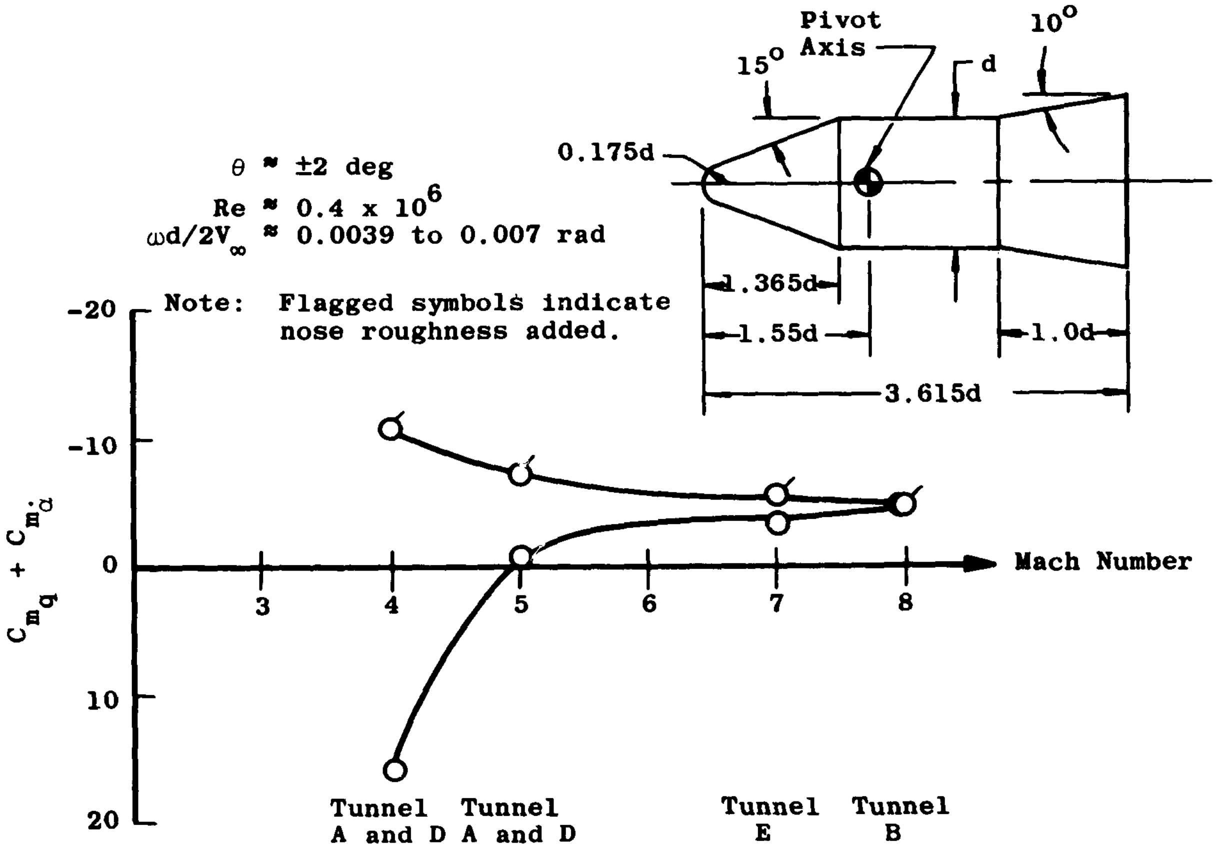

Fig. 16 Variation of the Damping-in-Pitch Derivatives with Mach Number for a Typical Re-entry Configuration

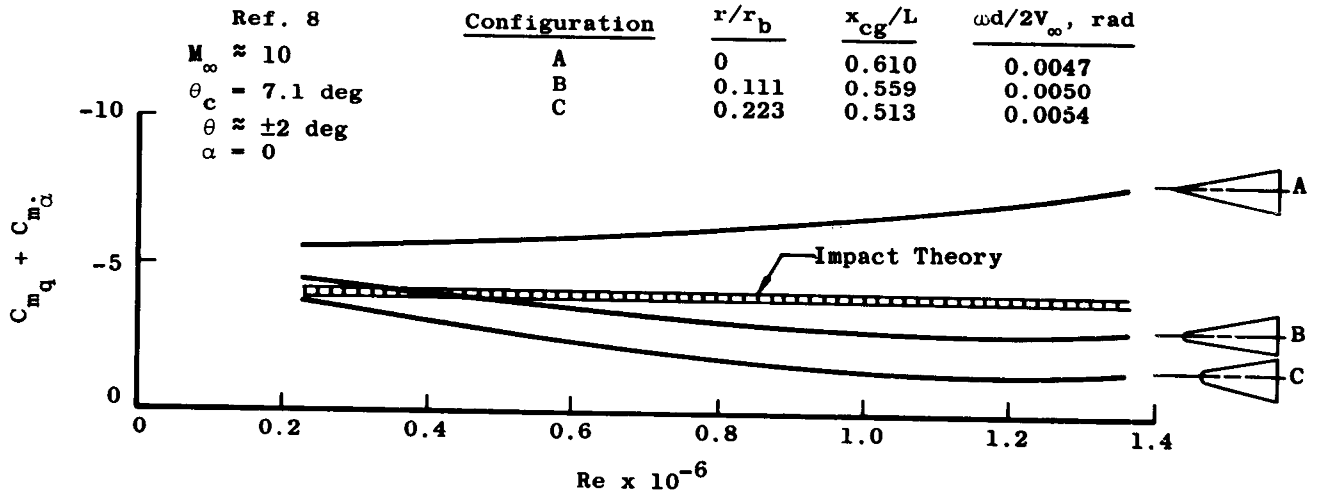

Fig. 17 Variation of the Damping-in-Pitch Derivatives with Reynolds Number for Three Skybolt Re-entry Vehicle Configurations

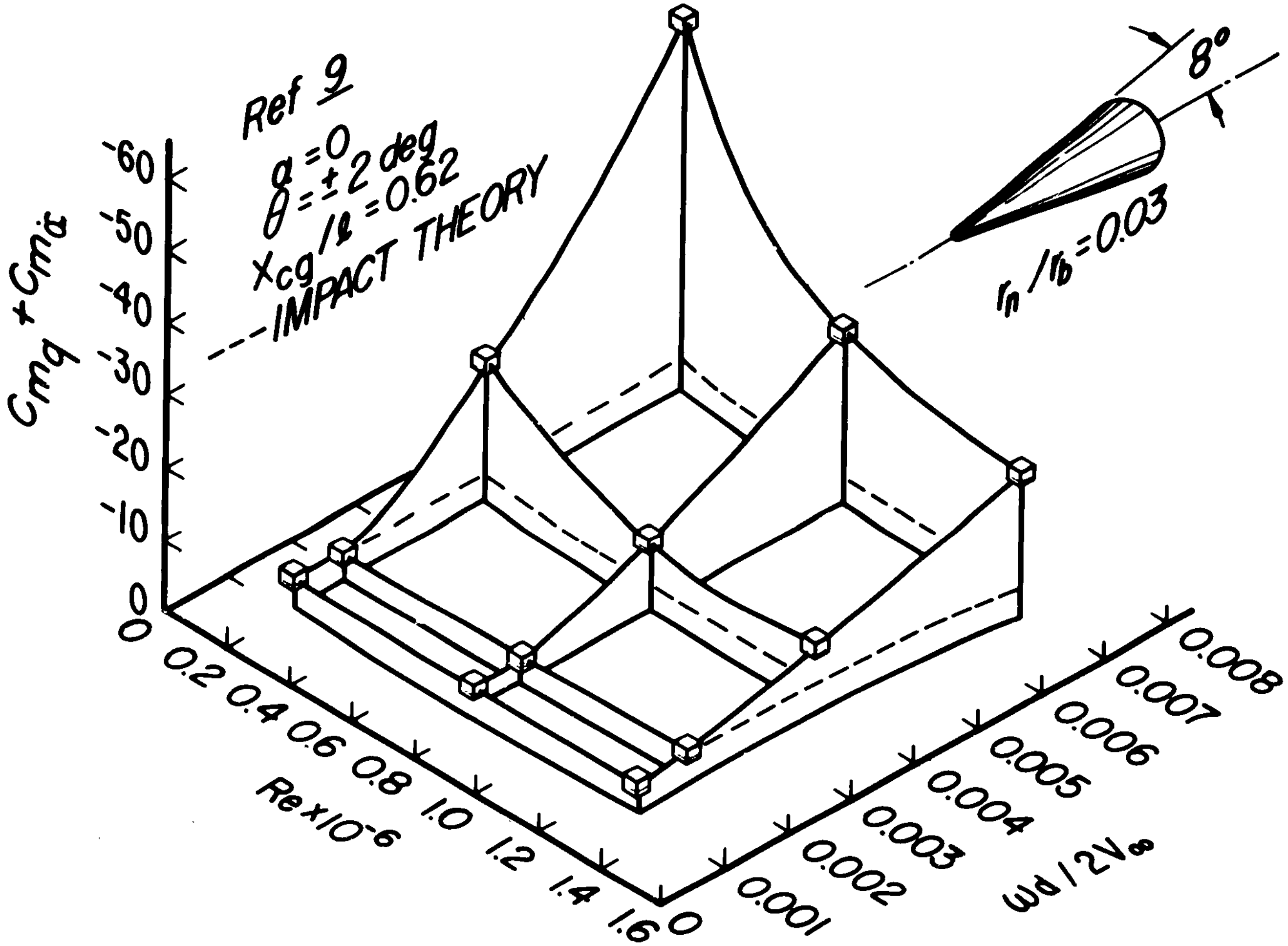

Fig. 18 Damping-in-Pitch Derivatives versus Reynolds Number and Reduced Frequency Parameter for a Blunted 8 deg Cone

A SIMPLIFIED INERTIA-COMPENSATED BALANCE TECHNIQUE FOR WIND TUNNEL MEASUREMENT OF LAUNCH VEHICLE RANDOM BUFFET EXCITATION

by C. V. Stahle, C. G. Stouffer and W. Silver

Space Systems Division
Martin Company
Baltimore 3, Maryland

Abstract

A simplified technique for measurement of launch vehicle random buffet excitation is presented which uses a rigid model of the forward portion of the vehicle. The technique combines the signals from a standard two-point moment balance with the signals from two strategically located accelerometers to provide an inertia compensated measurement of the aerodynamic moment at two points on the model. By proper design of the model and balance, the forward accelerometer will completely compensate for the inertia effects at the forward balance location, and the aft accelerometer will compensate for the inertia effects of the first three model-sting modes at the aft balance location. For the frequency range usually investigated, this provides adequate compensation of the model inertia effects permitting the moment of oscillatory aerodynamic forces to be measured by the Inertia Compensated Balance.

It is shown that, with a linearized partial mode representation of the vehicle bending modes, the modal excitation can be approximated by the integrated moment of oscillatory aerodynamic forces over the forward portion of the vehicle about the nodal points. These moments are determined from the balance measurements. Both the Power Spectral Density of the modal excitation and the Cross Spectral Density of the excitation between modes are obtained. From these spectra, the mean square loads can be evaluated using an extension of the Thompson-Barton approximation which includes the effects of the correlation in the vehicle response resulting from the simultaneous excitation of the modes.

The adequacy of the technique is verified experimentally by comparing the random moment applied to the model by an electromagnetic shaker with that measured by the balance. The close comparison of NASA Model 8 wind tunnel buffet measurements with previous pressure integration measurements verifies the adequacy of the pressure approach over the frequency range investigated. The Inertia Compensated Balance technique can be extended to measure simultaneously the excitation in two planes and is applicable to other similar investigations.

LIST OF ILLUSTRATIONS

Nomenclature

$C_{M_n M_m}$	Cross spectral density of the aerodynamic moment about the node of mode n and mode m
$C_{Q_n Q_m}$	Cross spectral density of the generalized modal excitation of mode n and mode m
g_n	Structural damping coefficient in mode n
K	Constant relating the inertia moment at the bridge location to the acceleration at the accelerometer location
ℓ_n	Distance from the nose of the vehicle to the node of mode n
M_n	$\int m(x)\, h_n^2(x)\, dx$, the equivalent mass for the nth mode
$M_n'(x)$	Moment at station X in the nth mode
$M_A(xb, t)$	Aerodynamic moment at the balance location
$M_I(xb, t)$	Inertia moment at the balance location due to model vibration
$M_T(xb, t)$	Total moment sensed by the balance bridge
$F_p(\omega, x)$	Fourier transform of the effective pressure force acting on an axial element at X
$F_p^*(\omega, x')$	Complex conjugate of the Fourier transform of the effective pressure force on an axial element at X'
T	Time, used to denote limiting process
t	Time, used to denote time variations
$W_{BM}(\omega)$	Power spectral density of the bending moment
$W_{Q_n}(\omega)$	Power spectral density of the generalized modal excitation
$W_{M_n}(\omega)$	Power spectral density of aerodynamic moment about the nodal point of mode n
$\ddot{\omega}(xa, t)$	Acceleration of the model at the accelerometer location
X	Distance aft of the nose of the prototype vehicle or the model
$\lvert Z_n(W) \rvert$	Impedance of the nth mode of the prototype vehicle
$\phi_n(x)$	Deflection shape of the nth mode
ϕ_n'	Effective modal slope over forward portion of the vehicle

θ_n	$\mathrm{Tan}^{-1}\, g_n / 1 - \frac{\omega^2}{\omega_n^2}$ the phase angle associated with the impedance of the nth mode
ω_n	Resonant frequency of the nth mode
$\xi_n(t)$	Modal coordinate indicating time variation

Introduction

This paper presents a simplified experimental technique for the measurement of the random buffet excitation of launch vehicle transverse bending modes using a rigid model. As a launch vehicle passes through the transonic region, it is subjected to large random pressure fluctuations due to boundary layer separation and shock wave interaction. These pressure fluctuations occur primarily over the forward portion of the vehicle and particularly at locations of abrupt change in shape. Because the effects of these fluctuating pressures cannot be predicted to the required degree of accuracy by analytical methods, they are investigated experimentally by wind tunnel tests using scaled models. The model similitude requirements and the scaling of the test results have been the subject of other papers presented at this symposium and will not be discussed in this paper.

There are two fundamentally different approaches to the wind tunnel investigation of the transonic buffet excitation of launch vehicle bending modes. One approach is to use dynamically scaled models; the other is to measure separately the modal excitation due to fluctuating pressures and the motion dependent unsteady aerodynamic effects. This paper is concerned only with the first part of the latter approach, the measurement of the modal excitation due to random pressure fluctuations.

The excitation of the vehicle bending modes is defined by the integral of the instantaneous pressure fluctuations over the surface of the vehicle, weighing each area element by its associated modal deflection. The Power Spectral Density and Cross Spectral Density of these integrated pressure fluctuations provide the desired measure of the modal excitation. The approach used in previous wind tunnel tests has been to determine this modal excitation from measurements of the fluctuating pressures acting on the vehicle. Although pressure fluctuation measurements are necessary for the determination of local structural excitation, these measurements are not amenable to analysis of the overall vehicle response. It becomes an impossible task to determine the modal excitation if only uncorrelated pressure measurements are made.

To provide more meaningful data than offered by the measurement of pressures alone, Cole and Coe developed a pressure integration technique for measurement of the integrated modal excitation, Ref. 1. Their technique utilized the signals from a large number of pressure transducers located over the forward portion of the model. By assigning effective areas to the transducers and electronically summing these signals, the integrated modal excitation was obtained. The difficulties with this technique are due to the approximations made in assigning effective areas to the transducers and to the complexity of the instrumentation and data reduction systems. A large number of pressure transducers and associated electronic equipment must be used even for measurements on simple bodies of revolution and cannot be confidently applied to more complicated payload shapes such as the Dyna-Soar. Because the excitation of only one mode at a time can be determined with this system without doubling the already complex data reduction system, the cross spectra of the excitation between the various vehicle modes cannot be obtained.

Because of these difficulties and the necessary approximations made, a simplified technique for more accurately measuring the integrated excitation of the vehicle modes and the cross spectra of the excitation between modes was desired. Extending the work of the Cornell Aeronautical Laboratory (which had developed an Inertia-Compensated Balance for measurement of static moments in a hypersonic shock tunnel) and in conjunction with the Aerospace Corporation, an Inertia-Compensated Balance (ICB) technique has been developed by Martin which fulfills these requirements.

The present Inertia-Compensated Balance technique uses the combined signals from two strategically located accelerometers and a two-point moment balance to measure the modal excitation of the vehicle bending modes. The arrangement of the model and the instrumentation is shown in Fig. 1. The accelerometers provide inertia compensation. Each accelerometer is located and its signal sensitivity is adjusted such that its electrical signal is equivalent to the inertia bending moment at its associated balance bridge location. Hence, the difference between the signals from one balance bridge and one accelerometer provides a measure of the integrated moment of the aerodynamic pressures acting over the forward portion of the model, compensated for the model inertia effects. From the simultaneous measurement of the integrated moment of the fluctuating pressures about two points on the model, the Power Spectral Density and the Cross Spectral Density of the modal excitations can be determined using a linearized partial mode representation of the prototype bending modes similar to that of Ref. 1.

In the first section of this paper, the determination of the modal excitation from moment measurements will be discussed. Then, the principle of operation of the Inertia-Compensated Balance and the final adjustment and calibration of the ICB system at the wind tunnel will be presented. Random vibration test results verifying the adequacy of the system will be presented. Measurements of buffet excitation obtained from wind tunnel tests using the ICB technique will be compared with data obtained previously by NASA Ames for a similar model using the pressure integration technique. The use of the ICB measurements for the determination of mean square loads will be discussed and, finally, the use of this technique for similar investigations and possible extensions of it will be mentioned.

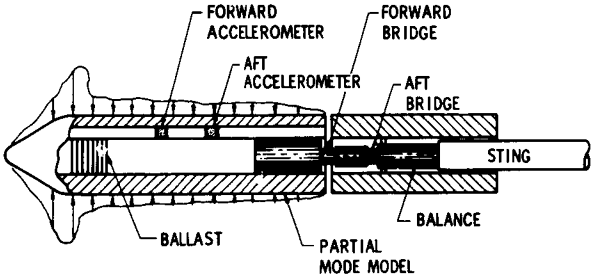

FIG. 1. TYPICAL MODEL ARRANGEMENT FOR INERTIA COMPENSATED BALANCE MEASUREMENTS

Determination of the Modal Excitations from Moment Measurements

The vehicle load due to random buffet excitation in which the designer is generally interested is the magnitude of the mean square bending moment. To determine this load, the power spectral density of the bending moment due to the response of the vehicle in its bending modes must be known. This bending moment power spectral density, $W_{BM}(\omega, x)$, can be defined by the following equation from Ref. 2:

$$W_{BM}(\omega, x) = \sum_{n} \sum_{m} \frac{M'_n(x)\, M'_m(x)\, e^{-i(\theta_n - \theta_m)}}{|Z_n(\omega)|\, |Z_m(\omega)|}$$

$$\cdot \iint \frac{2}{T} F_p(\omega, x)\, F_p^*(\omega, x')\, \phi_n(x)\, \phi_m(x')\, dx\, dx' \qquad (1)$$

The first portion of the right-hand side of this equation represents the "bending moment admittance" of the vehicle's structure in its various modes, while the second portion defines the generalized modal excitation. The modal excitation due to random forces can be further defined as:

$$\iint \frac{2}{T} F_p(\omega, x)\, F_p^*(\omega, x')\, \phi_n(x)\, \phi_m(x')\, dx\, dx' = \begin{cases} W_{Q_n}(\omega) & n = m \\ C_{Q_n Q_m}(\omega) & n \neq m \end{cases} \qquad (2)$$

Hence, the Power Spectral Density of the bending moment is equal to the sum over all modes of the "bending moment admittance" times the Power Spectral Density or Cross Spectral Density of the modal excitation. The purpose of the ICB technique is to experimentally evaluate these Spectral Densities of the modal excitation.

The integral of Eq (2) can be approximated by integrating only over the forward portion of the vehicle because the pressure fluctuations and the modal deflections are generally large only over this portion of the vehicle. In addition, the vehicle mode shape can be represented by a straight line for the forward portion of the vehicle with reasonable accuracy as shown in Fig. 2. With this linearized partial mode representation, the integral of Eq (2) can be written as:

$$\iint \frac{2}{T} F_p(\omega, x)\, F_p^*(\omega, x')\, \phi'_n\, \ell_n \left[1 - \frac{X}{\ell_n}\right] \phi'_m\, \ell_m \left[1 - \frac{X'}{\ell_m}\right] dx\, dx' = \begin{cases} \left[\phi'_n\right]^2 W_{M_n}(\omega) & n = m \\ \phi'_n\, \phi'_m\, C_{M_n M_m}(\omega) & n \neq m \end{cases} \qquad (3)$$

where

$$W_{M_n}(\omega) = \iint \frac{2}{T} F_p(\omega, x) \; F_p^*(\omega, x') \, \ell_n^2 \left[1 - \frac{X}{\ell_n}\right] \left[1 - \frac{X'}{\ell_n}\right] dx \, dx'$$

$$C_{M_n M_m}(\omega) = \iint \frac{2}{T} F_p(\omega, x) \, F_p^*(\omega, x') \, \ell_n \left[1 - \frac{X}{\ell_n}\right] \ell_m \left[1 - \frac{X'}{\ell_m}\right] dx \, dx'$$

Hence, with a linearized partial mode representation of the full-scale vehicle modes, the modal excitation is proportional to the Power Spectral Density of the moment of fluctuating pressure forces about the nodal points of the modes and the Cross Spectral Density of the moments about the nodal points of two different modes.

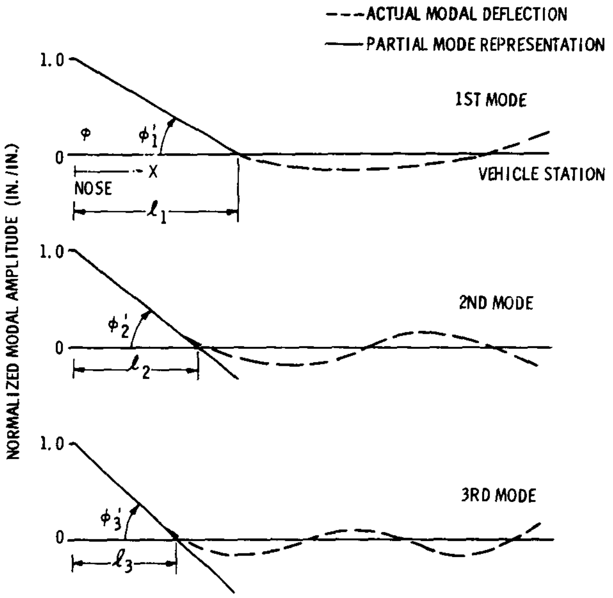

FIG. 2. LINEARIZED PARTIAL MODE REPRESENTATION

Having established the properties of the buffet pressure fluctuations that are required to define the modal excitation using a linearized partial mode representation of the prototype bending modes, now consider the capability of the ICB system to measure these properties. In Appendix A of this paper, it is shown that the Power Spectral Density and Cross Spectral Density of the moments at the two ICB balance locations can be used to determine the Power Spectral Density of the moment about any other point as well as the Cross Spectral Density between the moments at any two points. Because the modal excitations have been defined in terms of the Power Spectral Density and the Cross Spectral Density of the moments about the nodal points of the modes, these modal excitations can be completely determined from the ICB measurements at the balance locations.

A method for determining the mean square vehicle loads from the Power Spectral Density and Cross Spectral Density of the modal excitations is presented in Appendix B which extends the Thompson-Barton approximation to include the load contributions due to the simultaneous excitation of the vehicle modes.

Principle of Operation of the ICB System

If a standard balance without inertia compensation were used to measure the moment at a point on the model, the balance would measure both the integrated moment of pressure fluctuations and the moment due to vibration of the model. The dynamic sensitivity of the balance would reflect the impedance of the model-sting dynamic system having peaks at model resonances and low points between resonances as shown in Fig. 3. If the model inertia effects were compensated, the calibration curve would be approximately a horizontal line with the input and output moments of the balance system being nearly equal. This type of compensation is accomplished by electronically combining an accelerometer signal with a balance signal to eliminate the inertia effects of model vibration on the measured moment.

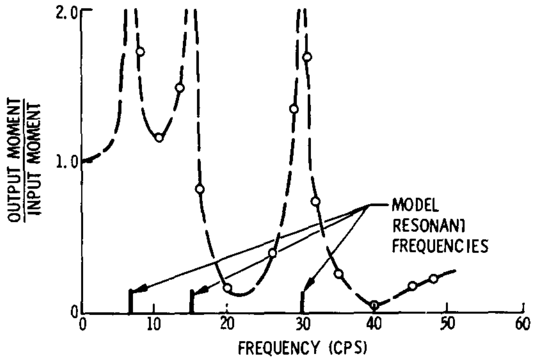

FIG. 3. DYNAMIC SENSITIVITY OF UNCOMPENSATED BALANCE

The principle of operation of the ICB system can be explained by considering one accelerometer-bridge combination of the typical model arrangement shown in Fig. 1. The moment measured by the strain gage bridge of the balance will be the sum of the aerodynamic moment and the moment due to model inertia effects. This can be written as:

$$M_T(X_b, t) = M_A(X_b, t) + M_I(X_b, t) \tag{4}$$

where the effects of damping are neglected because the damping is generally small and would affect the bridge moment only in narrow frequency bands near the model resonances. Considering a flexible model, the inertia moment at the bridge location, X_b, can be written in terms of the model modes and the acceleration at a point on the model, X_a, as:

$$M_I(X_b, t) = \sum_i \frac{M_i'(X_b)}{\omega_i^2} \ddot{\xi}_i = \sum_i \left[\frac{M_i'(X_b)}{\omega_i^2 \, \phi_i(X_a)}\right] \ddot{w}_i(X_a, t) \tag{5}$$

where $\ddot{w}_i(X_a, t)$ is the modal acceleration at X_a.

If by proper selection of an accelerometer location, the term in parentheses can be made constant for all modes, Eq (5) can be written as:

$$M_I(X_b, t) = K \sum_i \ddot{w}_i(X_a, t) = K \, \ddot{w}_T(X_a, t) \tag{6}$$

where

$$K = \frac{M_1'(X_b)}{\omega_1^2 \, \phi_1(X_a)} = \frac{M_2'(X_b{*})}{\omega_2^2 \, \phi_2(X_a)} = \frac{M_3'(X_b{*})}{\omega_3^2 \, \phi_3(X_a)} = \ldots \tag{6a}$$

That is, the inertia moment at the balance bridge will be proportional to the total acceleration at a point on the model. Then, from Eq (4), the aerodynamic moment can be obtained by subtracting the inertia moment which is proportional to the model acceleration at X_a:

$$M_A(X_b, t) = M_T(X_b, t) - K \, \ddot{w}_T(X_a, t) \tag{7}$$

Hence, by subtracting the acceleration measured by a properly located accelerometer and multiplied by an appropriate "gain constant," K, from the moment measured by the balance, the moment of aerodynamic pressure fluctuations is obtained.

The instrumentation system used to accomplish this is relatively simple and is presented in Appendix C. Of prime importance are the amplitude and phase characteristics of the transducers which must be carefully matched to assure adequate compensation.

If only one mode of the system is to be compensated, the requirement of Eq (6a) can be relaxed and Eq (6) becomes:

$$M_1(X_b, t) = \left[\frac{M_1'(X_b)}{\omega_1^2 \, \phi_1(X_a)}\right] \ddot{w}_1(X_a, t) = K_1 \, \ddot{w}_1(X_a, t) \tag{6b}$$

This means that for any point of acceleration measurement, X_a, the inertia effects due to model motion can be compensated by proper determination of a "gain constant," K_1, relating the moment at the balance bridge location, X_b, to the point at which the acceleration is measured. This, in effect, is what was accomplished previously by the Cornell Aeronautical Laboratory.

In order to provide compensation of two modes, the requirement imposed is that:

$$\frac{M_1'(X_b)}{\omega_1^2 \, \phi_1(X_a)} = \frac{M_2'(X_b)}{\omega_2^2 \, \phi_2(X_a)} \tag{6c}$$

For a given model and balance configuration, this relation determines the location of the accelerometer. The accelerometer must be positioned at a point such that the ratio of modal moment at the balance location to the modal acceleration at the accelerometer location is the same for both modes. If the modal bending moment at the balance bridge location is considered to be fixed (i. e., the model dynamic characteristics and the balance geometry are not variable), a unique accelerometer location is determined.

Extending the compensation to include three modes, the requirement indicated by Eq (6a) becomes

$$\frac{M_1'(X_b)}{\omega_1^2 \, \phi_1(X_a)} = \frac{M_2'(X_b)}{\omega_2^2 \, \phi_2(X_a)} = \frac{M_3'(X_b)}{\omega_3^2 \, \phi_3(X_a)} \tag{6d}$$

Now, to provide compensation of three modes, the modal moment at the balance location must be a variable. During the design of the model, the solution to Eq (6d) can be determined using analytical mode shapes to evaluate the modal moment at the bridge location, $M_i'(X_b)$. The accelerometer and bridge locations at which the ratio of modal moment to modal acceleration are equal for the first and second modes and for the first and third modes are determined for the model-balance configuration being considered using relations similar to that of Eq (6c). The results are plotted as shown in Fig. 4 and the design is varied until the first three modes are compensated at the balance locations as indicated in the figure.

If the portion of the model forward of the balance bridge location is effectively rigid, the accelerometer will be located at the center-of-percussion of the model about the bridge location and the inertia effects of all modes will be compensated. By proper model design, this can be accomplished for the forward balance bridge location for the frequency range of interest. However,

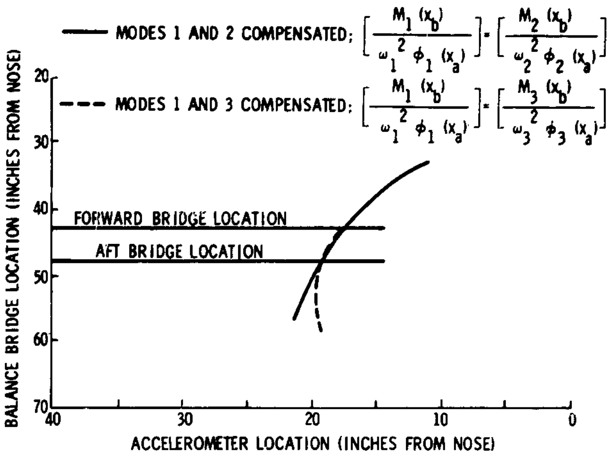

FIG. 4. CALCULATED MODEL COMPENSATION POINTS

Fig. 5. METHOD OF EXCITATION FOR LOCATING ACCELEROMETERS AND ADJUSTING SENSITIVITIES

the flexibility introduced by the forward balance flexure is sufficient to invalidate this center-of-percussion relation for the aft bridge. Since the low frequency range is of interest, compensation of only the first three model modes will generally be adequate for the aft balance bridge. This is accomplished by varying the model and balance configuration as discussed previously. Although guided by the design analysis for compensation of the first three model modes, final adjustments of the accelerometer locations and the mass of the model are made at the wind tunnel to achieve optimum inertia compensation.

Final Adjustment and Calibration

After assembling the model and balance on the sting in the wind tunnel, final adjustments and calibrations of the Inertia Compensated Balance system are accomplished. First, the accelerometers are located for a nominal mass of the model and the adequacy of the compensation determined. If the compensation is not within acceptable limits, the model mass is altered by the addition or removal of ballast and the first step repeated. Finally, the dynamic sensitivity of the balance is determined over the frequency range of interest. The procedure and results obtained are discussed below.

To determine the optimum accelerometer location, the model-sting system is sinusoidally excited at its first three resonances with an electromagnetic shaker attached to the sting aft of the balance. With the model excited at the sting as shown in Fig. 5, the moments measured by the balance bridges are due entirely to model inertia forces. With the system excited in its fundamental mode, the amplitudes of the accelerometer signals are adjusted so that the difference between each accelerometer signal and its corresponding strain gage signal is zero, i. e., the amplitudes of the accelerometer signal and the bridge signal are made equal. The second and third resonances are then excited in the same manner and the signals recorded. The accelerometers are then relocated and the procedure repeated. The optimum locations of the accelerometers are then determined by plotting the ratio of acceleration to strain as shown in Fig. 6. As mentioned previously, an accelerometer location at which this ratio is equal for all three modes is desired. Although there will be some response due to nonresonant modes (i. e., first mode response when the system is excited at the third mode resonance), this should be unimportant in that the ratio is finally made equal for the first three modes, the modes which should contribute the majority of nonresonant response.

If the compensation is within acceptable limits, the gains and locations of the accelerometers are fixed and remain so for the duration of the test. Otherwise, the model ballast is varied and the preceding steps repeated until adequate compensation is obtained.

With the proper position of the accelerometers established and the gains adjusted and locked into position, the dynamic sensitivity of the Inertia Compensated Balance can now be determined. The shaker is attached to the model, forward of the balance, through a calibrated force transducer. The output of the ICB system (the difference between the balance bridge and accelerometer signals) should measure only the oscillatory moment applied to the model, since inertia effects should be cancelled. Hence, by sinusoidally forcing the model through the frequency range of interest, the dynamic sensitivity of the system can be obtained.

Typical results are shown in Fig. 7, which indicates that the sensitivity of the system is constant well above the first three resonant modes of the model and sting support system. A maximum deviation of 10% is indicated throughout the frequency range of 10 to 140 cps, which was the range of interest for this particular model. Similar results were obtained for both sums for two different shaker locations. In contrast to the ICB system, the inability of an uncompensated balance to measure the sinusoidal input moment was shown in Fig. 3.

Verification of the ICB System

A final verification of the adequacy of the ICB system to compensate for inertia effects was accomplished by applying a random excitation force to the model forward of the balance through the calibrated force transducer. A typical comparison of the Power Spectral Density of the random input moment measured with the force transducer and the output moment measured with the Inertia Compensated Balance is shown in Fig. 8. Similar results were obtained for both balance locations with excitation at two different model locations. The results indicated the capability of the ICB system to measure the Power Spectral Density of the applied random moment within approximately ± 1 db. The adequacy of the system calibration is also verified by this comparison.

Comparison with Pressure Integration Measurements

Having proven the capability of the ICB system to compensate for model inertia effects, wind tunnel tests were conducted to obtain buffet excitation measurements comparable to those obtained previously by NASA Ames using the pressure integration technique. For this comparison, the NASA Model 8 hammerhead configuration was selected because of the large buffet excitation measured by Ames. The model was of the same scale and was tested in the same wind tunnel facility, the Ames 14-foot transonic tunnel, as was the model used for the pressure integration measurements.

The model configurations are shown in Fig. 9, which compares the two measurement systems. The pressure integration measurements utilized the signals from 76 pressure transducers located at 17 stations over the forward portion of the model. Four or eight pressure transducers were used at each station and combined in a bridge to give the moment contribution over a small span. The transducer locations were selected to provide approximately equal area moment contributions about station 64.85, one point about which the moment was measured. The signals from each section were then combined through a series of operational amplifiers to give the total integrated time correlated moment about either of the two reference points indicated in Fig. 9. The frequency range of interest was from approximately 20 to 140 cps, which would cover the simulated frequency range of structural bending modes for typical flight vehicles.

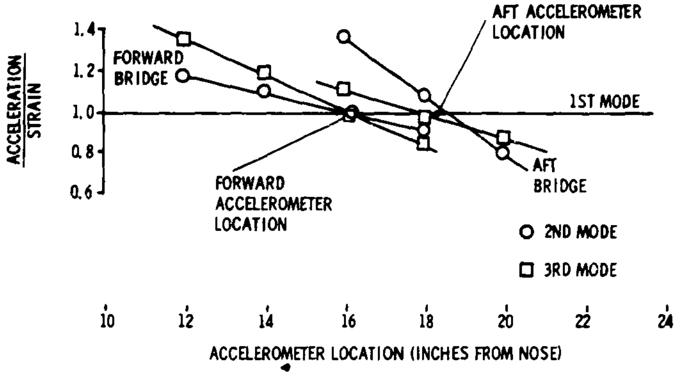

FIG. 6. SURVEY OF ACCELEROMETER LOCATIONS FOR BOTH MODEL STRAINGAGES

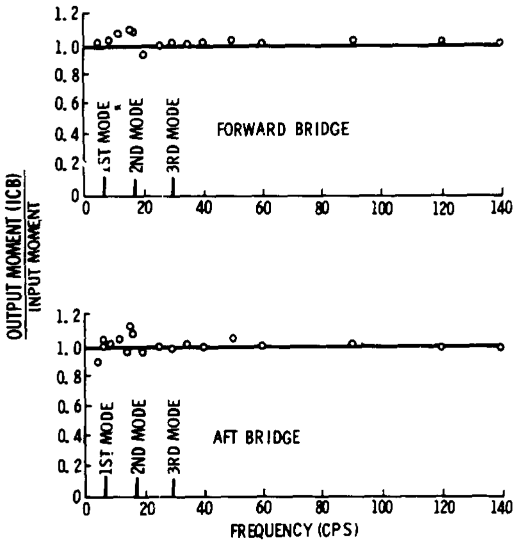

FIG. 7. DYNAMIC SENSITIVITY OF INERTIA COMPENSATED BALANCE

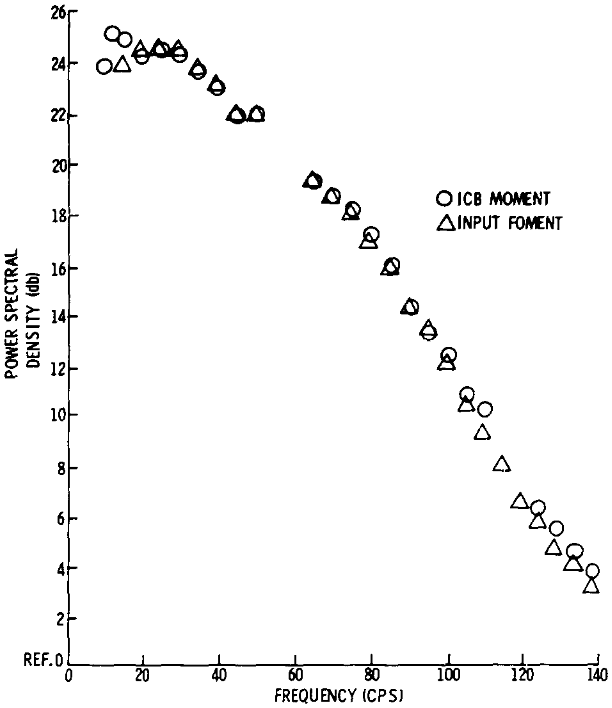

FIG. 8. COMPARISON OF RANDOM MOMENT PSD MEASURED WITH THE INERTIA COMPENSATED BALANCE AND A FORCE TRANSDUCER

The relative simplicity of the Inertia Compensated Balance is evident from Fig. 9. Only four transducers are required to measure simultaneously the moment at two model locations as compared to a single location with the pressure integration technique. In order to be assured that the buffet excitation was the same, pressure measurements were made at the three model locations indicated in Fig. 9 for comparison with previous measurements.

The Power Spectral Density of the aerodynamic moment about the forward reference point, Station 43.25, is shown in Fig. 10 for Mach 0.90. Comparison of the ICB data and the pressure integration data indicates negligible differences in the low frequency range (10 to 80 cps) and a maximum difference of 2 db at 110 cps. This is considered to be well within the expected accuracies of the data considering the necessary approximations included in the pressure integration technique and could possibly be due to differences in the pressure fluctuations as indicated by the comparison of pressure measurements shown in Fig. 11. The Power Spectral Density of the pressure fluctuations at this measurement location also differed by approximately 2 db at 110 cps. Good repeatibility of the ICB data is evident in Fig. 10 which includes data points obtained from two test runs. Similar comparisons were also made at Mach 0.95 with comparable results.

A comparison of the Power Spectral Density of the aerodynamic moment at the aft end of the model, Station 64.85, is shown in Fig. 12 and was ob-

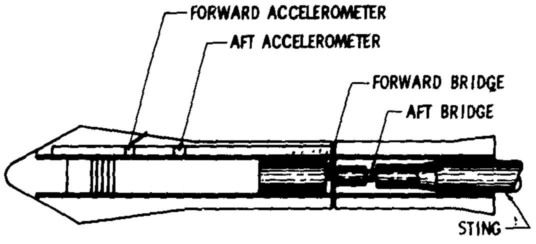

MARTIN INERTIA COMPENSATED BALANCE

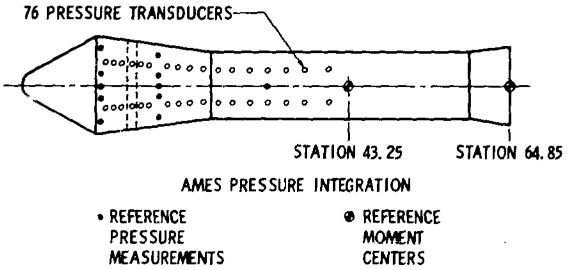

FIG. 9. COMPARISON OF ICB INSTRUMENTATION AND PRESSURE INTEGRATION INSTRUMENTATION

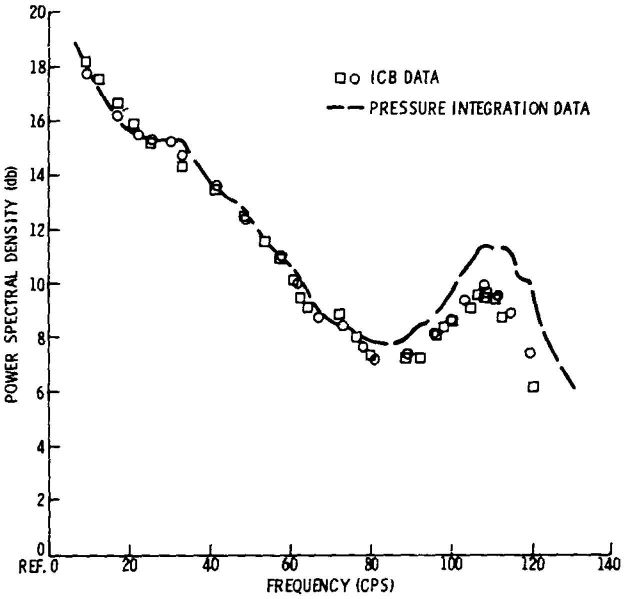

FIG. 10. COMPARISON OF AERODYNAMIC MOMENT PSD AT STATION 43.25

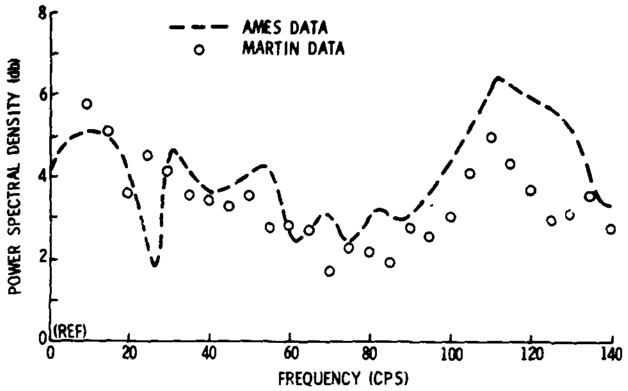

FIG. 11. COMPARISON OF PRESSURE POWER SPECTRAL DENSITY AT STATION 32.60, MACH 0.90

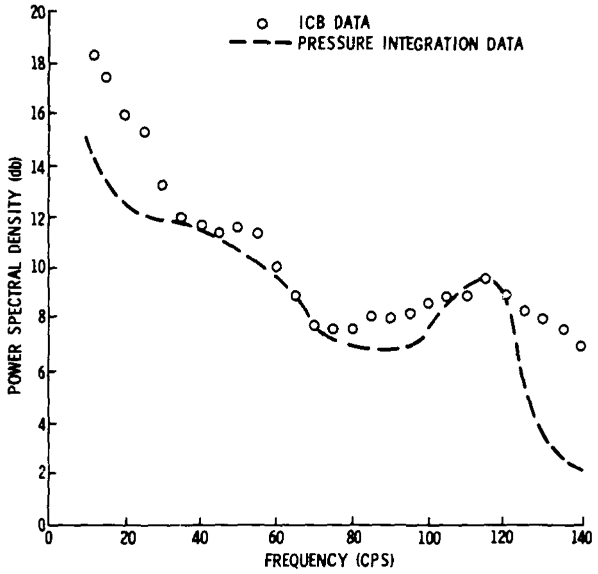

FIG. 12. COMPARISON OF AERODYNAMIC MOMENT PSD AT STATION 64.85, MACH 0.90

tained by transferring the ICB data to that point. Although the comparison with the pressure integration data is not as close as for Station 43.25 (having larger differences below 30 cps and above 120 cps), it is considered to compare favorably.

On the basis of these tests, it is evident that the Inertia Compensated Balance technique provides a considerable reduction in the complexity of the instrumentation even for a simple body of revolution. The comparison of the buffet excitation as measured by the two techniques provides increased confidence in the ICB system and verifies the capability of the pressure integration technique to measure the integrated buffet excitation over the frequency range investigated. For more complicated shapes such as a glider configuration, the Inertia Compensated Balance provides the only practical approach. In addition, more meaningful data is obtained with the Inertia Compensated Balance,since the simultaneous measurement of the moment at two points is obtained enabling the modal excitations to be completely determined as discussed in the first section of this paper.

Conclusions

On the basis of the theoretical and experimental results of this investigation, the following conclusions can be made regarding the Inertia Compensated Balance technique:

(1) A relatively simple experimental technique has been developed for the wind tunnel measurement of the modal excitations due to random buffet pressures which reduces by more than an order of magnitude the number of transducers and amplifiers required.

(2) This technique enables the simultaneous determination of the excitation of several modes as well as the correlation of the excitation between modes.

(3) The adequacy of this technique has been verified by several vibration tests of a model indicating an accuracy of approximately ± 1 db for the Power Spectral Density of the measured moment.

(4) Wind tunnel measurements of the NASA Model 8 buffet excitation agree almost identically with previous measurements using the pressure integration technique verifying the adequacy of that technique over the frequency range investigated.

(5) A method of analysis has been indicated for use with the experimental data obtained and includes the correlation effects between modes in one plane.

Extensions and Applications

This paper has been directed at the specific problem of determining launch vehicle transverse bending loads due to transonic buffeting and has considered loads in only one plane. However, the ICB technique can be applied to other investigations which impose similar measurement requirements and can readily be extended to include two planes of measurement. Generally, this technique is applicable to any investigation in which the integrated effects of random excitation are to be determined for modes that can be linearized. Wind tunnel investigations of oscillatory ground wind loads present an almost identical measurement problem and could be investigated with this technique. By simply duplicating the balance system in an orthogonal plane, the modal excitations in both the pitch and yaw planes could be investigated simultaneously. This would enable the correlation of the modal excitations between planes to be determined, which would be of prime importance for vehicles having axial symmetry when the modal frequencies in two directions are equal. Hence, the Inertia Compensated Balance technique can be used for investigations other than buffet and can be extended to measure the correlation between modal excitations in two directions.

References

1. Cole, H. A. Jr., and Coe, C.F. (U)"Dynamic Response of Hammerhead Launch Vehicles to Transonic Buffeting," Transactions of Seventh Symposium on Ballistic Missile and Space Technology, Vol. IV, August 1962. (Secret Report)

2. Powell, A., "On the Response of Structures to Random Pressures and to Jet Noise in Particular," Random Vibration, Technology Press of MIT, John Wiley & Sons, 1958.

3. Thompson, W. T. and Barton, M. V., "The Response of Mechanical Systems to Random Vibration," Journal of Applied Mechanics, 1957.

Appendix A

Determination of the Power Spectral Density and Cross Spectral Density of the Modal Excitation from ICB Measurements

The ICB system provides the moment at two locations as indicated in Fig. A-1.

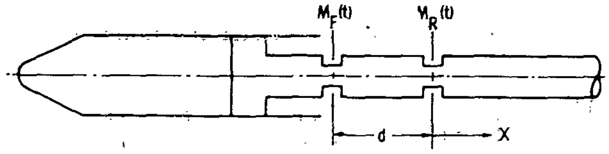

FIG. A-1. MODEL BALANCE SYSTEM

The modal excitation has been defined in terms of the Power Spectral Density and Cross Spectral Density of the moment about the prototype nodal points. Because the points at which the moments are measured with the ICB system do not necessarily correspond to the prototype nodal points, it is necessary to define the spectral densities at the nodal points in terms of the spectral densities at the measurement locations. This is developed in this appendix for two arbitrary nodal points, X_1 and X_2.

The moment at any point, X, can be defined in terms of the measured moments, $M_F(t)$ and $M_R(t)$ as:

$$M_X(t) = \left[\frac{X}{d} + 1\right] M_R(t) - \left[\frac{X}{d}\right] M_F(t) \tag{A-1}$$

where X is the distance aft of the rear measurement point as indicated in Fig. A-1.

The Power Spectral Density and Cross Spectral Density for the two measurement points are defined as

$$W_F(f) = \lim_{T \to \infty} \frac{F_T{}^*(f)\ F_T(f)}{T} \tag{A-2a}$$

$$W_R(f) = \lim_{T \to \infty} \frac{R_T{}^*(f)\ R_T(f)}{T} \tag{A-2b}$$

$$C_{FR}(f) = \lim_{T \to \infty} \frac{F_T{}^*(f)\ R_T(f)}{T} \tag{A-2c}$$

where

$$F_T(f) = \int_{-T}^{T} M_F(t)\, e^{-2\pi ift}\, dt$$

$$R_T(f) = \int_{-T}^{T} M_R(t)\, e^{-2\pi ift}\, dt$$

and the asterisk denotes the complex conjugate.

Then the Power Spectral Density at any arbitrary nodal point, X, can be written as:

$$W_X(f) = \lim_{T\to\infty} \left\{\left[1 + \frac{x}{d}\right] R_T{*}(f) - \left[\frac{x}{d}\right] F_T{*}(f)\right\} \left\{\left[1 + \frac{x}{d}\right] R_T(f) - \left[\frac{x}{d}\right] F_T(f)\right\} \qquad \text{(A-3a)}$$

$$= \left[1 + \frac{x}{d}\right]^2 W_R(f) + \left[\frac{x}{d}\right]^2 W_F(f) - \left[1 + \frac{x}{d}\right] \left[\frac{x}{d}\right] C_{FR}(f) - \left[1 + \frac{x}{d}\right] \left[\frac{x}{d}\right] C_{RF}(f) \qquad \text{(A-3b)}$$

but,

$$C_{FR}(f) = C_{RF}{*}(f)$$

therefore,

$$W_X(f) = \left[1 + \frac{x}{d}\right]^2 W_R(f) + \left[\frac{x}{d}\right]^2 W_F(f) - 2 \left[1 + \frac{x}{d}\right] \left[\frac{x}{d}\right] C_{FR}(f\text{: real}) \qquad \text{(A-3c)}$$

Consequently, the Power Spectral Density at any arbitrary nodal point can be determined from the Power Spectral Densities of the measured moments and the real portion of the Cross Spectral Density (Co-Spectrum) of the measured moments.

Similarly, the Cross Spectral Density between any two nodal points, X_1 and X_2, can be determined in terms of the measured spectra by defining

$$A_T(f) = \left[1 + \frac{X_1}{d}\right] R_T(f) - \left[\frac{X_1}{d}\right] F_T(f) \qquad \text{(A-4a)}$$

$$B_T(f) = \left[1 + \frac{X_2}{d}\right] R_T(f) - \left[\frac{X_2}{d}\right] F_T(f) \qquad \text{(A-4b)}$$

Then, the Cross Spectral Density between the moments at X_1, and X_2 becomes, by definition:

$$C_{X_1X_2}(f) = \lim_{T\to\infty} \frac{A_T^*(f)\, B_T(f)}{T} \qquad \text{(A-5a)}$$

$$= \lim_{T\to\infty} \frac{1}{T} \left\{\left[1 + \frac{X_1}{d}\right] R_T^*(f) - \left[\frac{X_1}{d}\right] F_T^*(f)\right\} \left\{\left[1 + \frac{X_2}{d}\right] R_T(f) - \left[\frac{X_2}{d}\right] F_T(f)\right\} \qquad \text{(A-5b)}$$

$$= \left[1 + \frac{X_1}{d}\right]\left[1 + \frac{X_2}{d}\right] W_R(f) + \left[\frac{X_1}{d}\right]\left[\frac{X_2}{d}\right] W_F(f) - \left[1 + \frac{X_1}{d}\right]\left[\frac{X_2}{d}\right] C_{RF}(f) - \left[1 + \frac{X_2}{d}\right]\left[\frac{X_1}{d}\right] C_{FR}(f) \qquad \text{(A-5c)}$$

Separating the Cross Spectral Density into its real and imaginary parts (the Co-Spectra and Quad-Spectra), this can be written as:

$$\begin{aligned} C_{X_1X_2}(f) = {} & \left[1 + \frac{X_1}{d}\right]\left[1 + \frac{X_2}{d}\right] W_R(f) + \left[\frac{X_1}{d}\right]\left[\frac{X_2}{d}\right] W_F(f) \\ & - \left\{\left[1 + \frac{X_1}{d}\right]\left[\frac{X_2}{d}\right] + \left[1 + \frac{X_2}{d}\right]\left[\frac{X_1}{d}\right]\right\} C_{FR}(f\text{: real}) \qquad \text{(A-5d)} \\ & - \left\{\left[1 + \frac{X_1}{d}\right]\left[\frac{X_2}{d}\right] - \left[1 + \frac{X_2}{d}\right]\left[\frac{X_1}{d}\right]\right\} C_{FR}(f\text{: imaginary}) \end{aligned}$$

From the relations developed in Eqs (A-3c) and (A-5d), it can be seen that the Power Spectral Density at any nodal point, X, and the Cross Spectral Density between two arbitrarily selected nodal points, X_1 and X_2, can be determined from the moment Power Spectral Densities at the balance bridge locations and the Cross Spectral Density of the measured balance moments.

Appendix B

Determination of the Mean Square Loads

Having established the capability of the ICB system to measure the Power Spectral Density and Cross Spectral Density of the modal excitation, the determination of the mean square vehicle loads from these data will be discussed. The mean square load at each vehicle location is determined from the integral, over frequency, of the Power Spectral Density of the load of interest. Because the bending moment is usually the desired load, the following discussion will be directed toward the determination of the mean square bending moment, although the same approach can be used for other loads. By combining Eqs (1) and (2), the bending moment Power Spectral Density can be written as:

$$W_{BM}(\omega, x) = \sum_{n} \frac{\left[M_n'(x)\right]^2}{\left|Z_n(\omega)\right|^2} W_{Q_n}(\omega) + \sum_{\substack{n \\ n \neq m}} \sum_{m} \frac{M_n'(x)\, M_m'(x)\, e^{-i(\theta_n - \theta_m)}}{\left|Z_n(\omega)\right| \left|Z_m(\omega)\right|} C_{Q_nQ_m}(\omega) \qquad \text{(B-1)}$$

In this equation, the Power Spectral Density and Cross Spectral Density of the excitation are determined from the Inertia Compensated Balance measurements using Eq (3). The modal moment coefficients are determined from the vibration analysis of the vehicle, and the modal impedance is determined from the vibration analysis including the effects of motion-dependent aerodynamic forces (i.e., aerodynamic damping, mass, and stiffness effects).

The mean square bending moment is determined by the frequency integral of the bending moment Power Spectral Density as:

$$\overline{M^2(x)} = \sum_{n} \left[M_n'(x)\right]^2 \int_0^\infty \frac{W_{Q_n}(\omega)}{\left|Z_n(\omega)\right|^2} d\omega + \sum_{\substack{n \\ n \neq m}} \sum_{m} M_n'(x)\, M_m'(x) \int_0^\infty \frac{e^{-i(\theta_n - \theta_m)}}{\left|Z_n(\omega)\right| \left|Z_m(\omega)\right|} C_{Q_nQ_m}(\omega)\, d\omega \qquad \text{(B-2)}$$

For small damping and significantly different modal frequencies, this integral can be approximated as

$$\overline{M^2(x)} = \frac{\pi}{2} \sum_{n} \frac{\left[M_n'(x)\right]^2 W_{Q_n}(\omega_n)}{g_n M_n^2 \omega_n^3} + \frac{\pi}{2} \sum_{n} \sum_{m} \frac{M_n'(x)\, M_m'(x)}{M_n M_m \omega_n (\omega_m^2 - \omega_n^2)} \left[C_{Q_nQ_m}(\omega_n\text{: imaginary}) - \frac{\omega_n}{\omega_m} C_{Q_nQ_m}(\omega_m\text{: imaginary})\right] \qquad \text{(B-3)}$$

The first term of this equation is the Thompson-Barton approximation, Ref. 3, reflecting the resonant response in the various vehicle modes. The second term reflects the correlation between the response in two modes due to the correlation of the modal excitations and can be derived in a similar manner as the first term.

Appendix C

Inertia Compensated Balance Instrumentation

The instrumentation used in the ICB system is depicted in Fig. C-1.

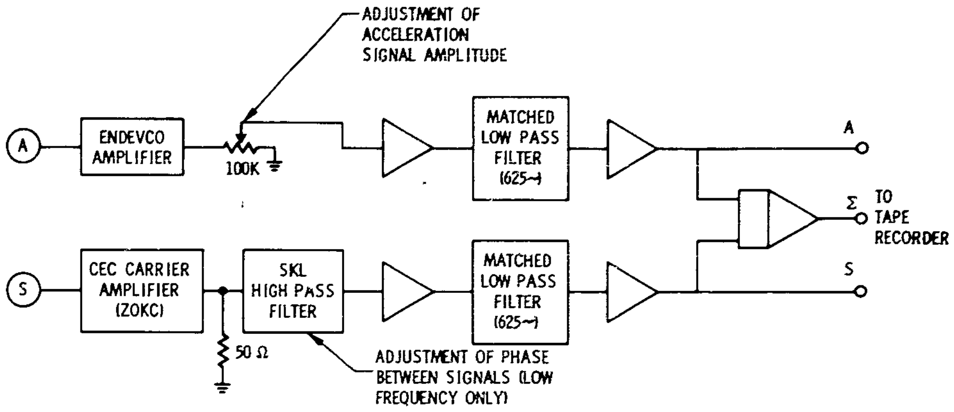

FIG. C-1. TYPICAL ICB CIRCUIT SCHEMATIC

The symbols used indicate the following:

A_f	Forward accelerometer signal
A_r	Aft accelerometer signal
S_f	Forward strain gage bridge signal
S_r	Aft strain gage bridge signal
Σ_f	ICB moment measured at the forward bridge location
Σ_r	ICB moment measured at the aft bridge location

Of these, A_f, S_f, A_r, and S_r are primary measurements; Σ_f and Σ_r are produced by summations of their respective accelerometer and strain gage bridge signals.

S_f and S_r were obtained from a standard two-point balance instrumented with four active arm bending bridges. The strain gages used were Baldwin

Lima Hamilton Type AB7. These bridges were excited and the signals were amplified by a CEC, Type 1-127, 20-kc carrier amplifier.

A_f and A_r were obtained using Endevco Type 2235 piezo-electric accelerometers. Signals from these transducers were amplified and matched to the remaining system by Endevco Type 2617 amplifiers.

The choice of a piezo-electric accelerometer was dictated by the need for a transducer with a high resonance frequency and low damping. This is required to avoid a large phase shift at high frequencies between the actual and indicated acceleration. At low frequencies, a phase difference existed due to the roll-off characteristic of the accelerometer-amplifier combination although no amplitude roll-off existed in the frequency range of interest. This phase difference was removed by determining the roll-off and matching it in the bridge circuit with a high pass filter. With this device, the phase differences in the strain and accelerometer circuits were eliminated without causing an amplitude roll-off by adjusting the filter corner frequency well below the frequency range being investigated. In addition, A_f and A_r accelerometer-amplifier combinations were matched in phase roll-off characteristics so that instrumentation phase shifts between Σ_f and Σ_r were kept negligibly small. The amplitude effects of roll-off were outside the frequency range of interest for all components.

Amplitude adjustments were made by fixing the S_f and S_r signals at convenient levels and adjusting the amplitudes of A_f and A_r as required during the calibration of the system.

Matched low pass filters were used in the A_f, A_r, S_f, and S_r circuits. These eliminated undesired high frequency signals from the data. These signals were primarily 20-kc noise from the carrier amplifiers and acoustically induced accelerations during the wind tunnel tests. Care was taken to assure that these filters did not produce undesirable phase and amplitude effects.

Figure C-1 shows several operational amplifiers other than the summing amplifiers. These were used primarily as impedance matching devices for the circuits and also as points where the various signals could be monitored during the calibrations. Both the operational and summing amplifiers were fabricated by NASA-Ames personnel from commercial components. The accelerometer and strain gage bridge were wired so that the strain signals were 180° out of phase with the acceleration signals. These signals were then summed.

All data was recorded on a Precision Instrument Type PI 214 14-track FM Type Recorder-Reproducer. Calibrations were made to determine the phase shifts inherent between critical tracks of recorded tape. These tended to increase with frequency and were held to less than 2° in the range of interest. Two-minute records were taken at each data point.

Data reduction was performed by the Dynamics Laboratory at Martin-Baltimore. The data were reproduced on an Ampex Type FL200 Tape Loop Reproducer. Power Spectral Density and Cross Spectral Density plots were produced using a Technical Products Company Type 627 Analyzer with 645 Multiplier.

THE EFFECT OF MODEL SCALE ON RIGID-BODY UNSTEADY PRESSURES ASSOCIATED WITH BUFFETING

By Charles F. Coe

National Aeronautics and Space Administration
Ames Research Center
Moffett Field, Calif.

ABSTRACT

The question of the effect of model scale on launch vehicle dynamic measurements is one which invariably arises in connection with the application of measured unsteady pressures on wind-tunnel models. The scaling of unsteady pressure measurements is discussed in this paper which presents comparisons of results of pressure-fluctuation measurements on both wind-tunnel models and on full-scale Ranger 5 and Mercury vehicles. In addition, results of tests using different sized models are shown in order to cover some of the different types of local flow associated with buffeting. The effects of scale on the root-mean-square fluctuations of pressure, the longitudinal correlation of the fluctuations, and on the power spectral densities are shown for selected transonic Mach numbers where the fluctuations are most severe.

LIST OF ILLUSTRATIONS

THE EFFECT OF MODEL SCALE ON RIGID-BODY UNSTEADY PRESSURES ASSOCIATED WITH BUFFETING

By Charles F. Coe

National Aeronautics and Space Administration
Ames Research Center
Moffett Field, Calif.

INTRODUCTION

The unsteady aerodynamic loads on launch vehicles at transonic speeds have recently received considerable attention. These unsteady loads result from pressure fluctuations that occur within regions of shock waves or regions of separated flow or both. Escape rocket systems, blunt noses to insure abort stability, bulbous payloads which are larger than their booster rockets, and numerous protuberances all lead to this troublesome flow unsteadiness which can cause buffeting.

Several wind-tunnel investigations (refs. 1 to 6) have been undertaken at Ames and Langley Research Centers and at Arnold Engineering Development Center to measure pressure fluctuations on both specific configurations and also on a variety of body shapes to determine effects of profile variations. When any of these pressure-fluctuation measurements are used for estimation of vehicle dynamic response, questions invariably arise as to the proper method of scaling the data to full scale. For example, are the concepts of a constant Strouhal number and scaling by application of the commonly used reduced frequency parameter, $\omega d/V$, appropriate for random nonperiodic buffet pressures. For lack of any verifying information the above concepts have been employed in references 6 and 7. Two recent investigations (refs. 8 and 9) have devoted some attention to the problem of scaling unsteady pressures. The latter (ref. 9), which contains data for models varying in size by a ratio of 5 to 1, tends to substantiate the validity of the reduced frequency parameter for scaling.* The ultimate test of scaling buffet pressures, however, comes with the direct comparison between wind-tunnel model data and full-scale data obtained during the launching of a vehicle.

The measurement of differential pressure fluctuations at two Agena stations during the Ranger 5 launch and of pressure fluctuations on the Mercury-Atlas adapter during launch of the MA-4, MA-5, MA-7, and MA-8 provided a good opportunity to make such comparisons. As a result, tests of a 7-percent scale Mercury model and a 10-percent scale Ranger model were included in an investigation of scale effects using different sized models which was in progress at Ames Research Center. The tests were conducted at transonic Mach numbers with

---

*Results from this investigation appear in the paper by Hanson and Jones of Langley presented at an earlier session of this Symposium.

pressure transducers located at the same stations as the full-scale flight instrumentation. It is primarily the results of these comparative tests that are contained herein. Additional data from the general research program are included to illustrate the effects of scale for different types of unsteady flow.

NOTATION

d	body reference diameter
D_{max}	maximum body diameter
f	frequency, cps
M	free-stream Mach number
p_t	stagnation pressure
q_o	free-stream dynamic pressure
V	free-stream velocity
x	distance along body axis from nose
α	angle of attack
Φ	power spectral density of fluctuating pressure coefficient, $\overline{\Delta C_p^2}$ per cps
φ	power spectral density of fluctuating pressure, $\overline{\Delta P^2}$ per cps
ω	frequency, radians per second
$\Delta C_p(\mathrm{RMS})$	coefficient of the root-mean-square fluctuation of pressure about the mean, $\frac{\Delta P(\mathrm{RMS})}{q_o}$
$\overline{\Delta C_p^2}$	coefficient of the mean-square fluctuation of pressure, $\frac{\overline{\Delta P^2}}{q_o^2}$
$\Delta P(\mathrm{RMS})$	fluctuation of pressure about the mean
$\overline{\Delta P^2}$	mean-square fluctuation of pressure, psf^2

MODELS

The models tested to investigate scaling effects (fig. 1) were a 7-percent scale Mercury-Atlas, a 10-percent scale Ranger, and three sizes each of models 8 and 13a.* For the Mercury-Atlas and Ranger models the Atlas cylindrical bodies were neither scaled in length nor did they include any protuberances. Key longitudinal stations are indicated in the figure to aid in visualizing the placement of the pressure transducers relative to the body profiles. The reference diameters used for scaling the results are also shown.

All the models were sting mounted except the 26-inch-diameter model 13a which was tested as a half model mounted on the 14-foot transonic wind tunnel wall to minimize the effects of blockage. All the models were tested in the 14-foot wind tunnel except the Mercury-Atlas which was tested in the 11-foot transonic wind tunnel and the 6.31-inch-diameter model 8 which was tested in the 6- by 6-foot wind tunnel.

The pressure transducer stations that match the locations on the full-scale vehicles are marked with an x in figure 1. The differential pressure fluctuations were measured on the Ranger by taking the electrical difference between the outputs from the transducers mounted opposite each other. Flush-mounted 1/4-inch-diameter strain-gage-type transducers were used on all the models.

A photograph of the Mercury model in the 11- by 11-foot wind tunnel is shown in figure 2. An arrow indicates the relative location of the transducer with respect to the bulges on the ring clamp between the spacecraft and adapter section. The transducer station behind one of the bulges at approximately mid-length of the adapter is that at which flight data were obtained.

EFFECTS OF SCALE

When dynamic data associated with motion effects are measured on models, it is accepted that the geometric similarity of the flow cannot be maintained unless the reduced frequencies for model and full scale are the same. Although there has been doubt whether the reduced frequency parameter is applicable to random unsteady aerodynamic measurements, simple dimensional analyses by Liepmann (ref. 10) of the variable parameters involved indicate that the dimensionless reduced frequency parameter can be used to scale pressure-fluctuation measurements:

$$\frac{\omega d_1}{V_1} = \frac{\omega d_2}{V_2}$$

---

*The model numbers were assigned to the series of launch vehicle payload shapes tested at Ames Research Center.

and

$$\Phi_1 = \frac{\overline{\Delta C_{p_1}^2} V_1}{d_1} = \frac{\overline{\Delta C_{p_2}^2} V_2}{d_2} = \Phi_2$$

Since

$$\Delta C_p(\mathrm{RMS}) = \sqrt{\int_{(\omega d/V)_1}^{(\omega d/V)_2} \left(\frac{\Phi V}{2\pi d}\right) d\left(\frac{\omega d}{V}\right)}$$

it follows that in order to compare RMS measurements from model to full scale or from one model size to another, the range of frequencies included in the RMS measurements must be scaled in proportion to the reference dimensions.

Comparisons of Mercury Results

A comparison of power spectra of the pressure fluctuations measured on the Mercury-Atlas adapter is shown in figure 3. The wind-tunnel data are for a fixed Mach number of 1.0 while the flight data were obtained for a range of Mach numbers near 1.* The comparison is based on reduced frequency. (The $V/2\pi d$ in the ordinate scale converts the power spectra from $\overline{\Delta C_p^2}$ per cps to $\overline{\Delta C_p^2}$ per unit of reduced frequency.) It can be seen from these results that the 7-percent model data, which have been scaled by a factor of about 14.3, fit reasonably well within the limits of the spread of flight measurements. To illustrate the extent of frequency scaling the limit of the 7-percent model data is at approximately 5,200 cps while the full-scale data for the same reduced frequency is approximately 365 cps.

A curve is also shown from reference 6. While this curve appears higher than the others, the difference between it and MA-4 levels is less than the spread from MA-4 to MA-5. This spread of a factor of about 4 on a mean-square scale (factor of 2 on a RMS scale) serves to indicate the limits of accuracy, within the current state of the art, that might be expected when predicting pressure fluctuations from model measurements. One obvious factor that influences the accuracy of flight data is the fact that flight-time histories are not stationary.

Since the RMS level of amplitude is the most common measurement applied to pressure fluctuations, it is appropriate to examine the effects of scaling on these measurements. The flight-time histories of the RMS pressure fluctuations on the Mercury-Atlas adapter are shown in figure 4. Points from the 7-percent scale model extend over a range of Mach numbers from 0.8 to 1.2. Since there were differences between model q_o and full-scale q_o, the model results have been adjusted to full scale. As noted, the band-pass frequency range of the flight data extends up to 500 cps. The scaled frequency range of

---

*The full-scale data were obtained from unpublished results which have been compiled by Mr. James Ancell of Aerospace Corporation.

the model should extend to about 7,200 cps, but unfortunately the upper frequency limit of the tape recording of data was only 6,000 cps. Even though the band-pass range was less than the properly scaled range, these 7-percent model data still generally are close to the MA-5 data. The point indicated by an x shows an estimated level for the range of frequencies extrapolated to 7,200 cps from the power spectrum in figure 3. As can be seen, the agreement between the 7-percent model data and the average flight data is improved. Points are also shown in figure 4 which were obtained for a band-pass filter range from 8 to 500 cps which is about the same range as for the full-scale data. The difference between the comparisons of model results and flight data for the two filter ranges further substantiates the validity of frequency scaling.

Comparisons of Ranger 5 Results

The power spectra of differential pressure fluctuations on the Agena with the Ranger 5 payload are shown in figure 5.* These results, which were scaled by a factor of about 10, generally agree more closely than did the Mercury data, and consequently add more support to the validity of scaling by the reduced frequency parameter. It should be noted that the frequency range of the measurements of fluctuations on the Agena was very low compared to the range available on the Mercury. This fact may partly account for the better comparisons between the Agena measurements.

Time histories of the RMS levels of the differential pressure fluctuations are shown in figure 6. As with the Mercury data, the range of band-pass filtering of the signal going into the RMS meter was scaled inversely as the model scale. For the Agena the range was from 8 to 1,000 cps for the model and from 0.8 to 100 cps for full scale. With these band-pass frequencies precisely scaled, the maximum intensities were reasonably well predicted as was the variation with time for station 259. At station 249 the flight-time history indicates an earlier buildup of intensity and also a dip near 47 seconds that was not followed by the wind-tunnel data which were taken at fixed Mach numbers. One might speculate that these differences between wind-tunnel and flight data could well be within the limits of accuracy that can be expected considering the unknown effects of Reynolds number and also other problems associated with obtaining accurate dynamic measurements.

---

*The flight power spectra and a magnetic tape of the differential pressure fluctuations were obtained from Lockheed Missiles and Space Company. The flight data will appear in a forthcoming report by William Henricks, Flight Test Report for Ranger Vehicle 6005, SS/626/5351, LMSC/A384258.

Effects of Scale on Model 8

The separated flow on the Mercury adapter and on the Agena both produced relatively flat power spectral densities. Previous experience with model 8 for other investigations has shown that the spectral densities vary in shape from a predominately low-frequency spectrum near the maximum diameter shoulder to a flat spectrum as the distance from this shoulder is increased. For this reason model 8 was originally selected for the investigation of scale effects so that more than one spectrum shape could be covered.

Figure 7 shows the longitudinal distribution of pressure fluctuations on model 8 for three different model sizes. As was done previously the band-pass frequencies for the RMS readings were scaled inversely as the model diameter starting from an upper limit of 2,000 cps on the 6.31-inch-diameter model. Once again it appears that satisfactory agreement was obtained, further substantiating the use of the reduced frequency for scaling. This substantiation by use of the RMS levels is only valid, however, where the power spectral levels are high enough in the frequency range being scaled to effect the RMS. For model 8 the power spectra indicate higher energy levels at the higher frequencies at stations aft of $x/D_{max} = 1.4$.

As previously mentioned, near the shoulder on model 8 the pressure fluctuations are concentrated at the lower frequencies. An example of scaled power spectra from a station within this region is shown in figure 8. The results appear to scale well including the peaks at $\omega d/V = 0.78$, which, as a result of the satisfactory scaling, can be concluded to be a peak caused by an aerodynamic frequency rather than a model motion. It is also interesting to note that the results were obtained in different wind tunnels. The 6.31-inch model was tested in the 6- by 6-foot tunnel and the other two models were tested in the 14-foot wind tunnel.

Effects of Scale on Model 13a

All the previous data shown lead to the conclusion that pressure-fluctuation measurements should be scaled by application of the reduced frequency parameter. These data have been from regions of separated flow, and the spectra have been smooth curves except for the peaks which scaled on model 8. In contrast to the previous smooth spectra, figure 9 shows an example of power spectra of fluctuations in the region of the shock wave on model 13a. These results have not been scaled. It can be noted that several peaks coincide on the two smaller models which were sting mounted, and that a smoother spectrum without such predominant peaks was measured on the 26-inch-diameter half model which was mounted on the tunnel wall. The fact that the peaks tend to coincide when the model supports are similar and change when the support is changed indicates that the shock-wave motion is influenced by model motions. The peak near 190 cps also coincides with a stream disturbance in the 14-foot wind tunnel (see ref. 1) thus indicating an influence of stream fluctuations as well. Since it would be expected that the full-scale fluctuations would also be influenced by vehicle motions and stream fluctuations, the details of spectra of this type certainly could not be scaled. It appears, at present, that for design purposes the best approach would be to construct a smooth power spectrum having a slope like the over-all slope of the measured curve and an area under the curve equal to the measured mean-square amplitude. There is some justification for this approach since as shown in reference 1 a model in different wind tunnels with different support properties produced the same RMS measurements even though in one case a large peak predominated. In other words, it appears that the energy available from the shock wave to produce fluctuations is unchanged, but that the frequency distribution can be influenced.

Effect of Total Pressure Variations

The power spectra of the pressure fluctuations have been put in coefficient form by dividing the spectra measurements by q_o^2. While generally this has been assumed to be a correct approach, nevertheless, some measurements were made on model 8 to check the effect of varying q_o by testing at different total pressures. Figure 10 shows an example of power-spectrum measurements of differential pressure fluctuations obtained in the 11- by 11-foot transonic wind tunnel at total pressures of from 15 to 60 inches of mercury. As can be seen there was little effect of total pressure.

Correlation of Pressure Fluctuations

In order for wind-tunnel measurements of pressure fluctuations to be of value it is necessary that the spatial correlation of the fluctuations on the model be the same as on the full-scale vehicle. There has been insufficient time to obtain cross spectral densities of any of the scaling data before this symposium; however, a quick look at the over-all correlation was obtained from correlation coefficient measurements as shown in figure 11. As with the RMS values previously presented, the band-pass frequency range of the signals to the analyzer was scaled inversely as the model diameters. While there are not many points available for comparison, those shown indicate the same correlation coefficients for a difference in model size near a factor of 4. Other correlation coefficient measurements with respect to different stations show essentially the same agreement for the same two models.

Attempts were also made to perform a correlation coefficient analysis between the two stations tested on the Ranger. Average coefficients obtained from the flight data over the periods of time from 43 to 46 seconds after launch and from 45 to 50 seconds agree reasonably well with the 10-percent scale model data at fixed Mach numbers of 0.79 and 0.90, respectively. The corresponding measurements were as follows:

Full scale, 43-46 sec correlation coefficient = 0.155
10-percent model, M = 0.79 correlation coefficient = 0.130
Full scale, 40-45 sec correlation coefficient = 0.180
10-percent model, M = 0.90 correlation coefficient = 0.21

CONCLUDING REMARKS

On the basis of this investigation and results presented herein, it appears that pressure-fluctuation measurements on models in regions of separated flow should be scaled to full scale by application of the reduced frequency parameter. Scaling by a factor of 14.3 on the Mercury model and by a factor of 10 on the Ranger 5 model gave good agreement with flight results.

In the region of the shock wave, model measurements can be influenced by motions of the model and also by disturbances in the stream. As a result, less accuracy can be expected. It will probably be necessary to estimate power spectral densities from the measured RMS level and a generalized spectrum shape.

Correlation coefficient measurements indicate the same coefficients for different sized models of model 8. Reasonable agreement was also obtained between the 10-percent model of the Ranger 5 and full scale; however, cross spectral densities are required before definite conclusions can be drawn regarding possible effects of scale on the spatial correlation of pressure fluctuations.

REFERENCES

1. Coe, Charles F.: Steady and Fluctuating Pressures at Transonic Speeds on Two Space-Vehicle Payload Shapes. NASA TM X-503, 1961.
2. Coe, Charles F.: The Effects of Some Variations in Launch-Vehicle Nose Shape on Steady and Fluctuating Pressures at Transonic Speeds. NASA TM X-646, 1962.
3. Coe, Charles F., and Nute, James B.: Steady and Fluctuating Pressures at Transonic Speeds on Hammerhead Launch Vehicles. NASA TM X-778, 1962.
4. Coe, Charles F., and Kaskey, Arthur J.: The Effects of Nose Bluntness on the Pressure Fluctuations Measured on 15° and 20° Cone-Cylinders at Transonic Speeds. NASA TM X-779, 1963.
5. Austin, R. F., and Prunty, C. C.: Investigation of Buffet Phenomena on a 0.24-Scale Model of the Forward Portion of the Titan B Missile With the Mark 4 and Mark 6 Re-Entry Bodies. AEDC-TN-61-78, Sept. 1961.
6. Goldberg, Arthur P., and Adams, Richard H.: Mercury-Atlas Buffeting Loads at Transonic and Low Supersonic Speeds. STL/TR-60-0000-AS431, Nov. 28, 1960.
7. Goldberg, A. P., and Wood, J. D.: Dynamic Loads in the Atlas-Able 5 During Transonic Buffeting. STL/TM-60-0000-19075, Aug. 22, 1960.
8. Chevalier, H. L., and Robertson, J. E.: Unsteady Pressures and Scale Effects on Models of the Titan B Mark 4 Re-Entry Body at Transonic Speeds. AEDC-TDR-62-178, Nov. 1962.
9. Jones, George W., Jr., and Foughner, Jerome T., Jr.: Investigation of Buffet Pressures on Models of Large Manned Launch Vehicle Configurations. NASA TN D-1633, 1963.
10. Liepmann, H. W.: Parameters for Use in Buffeting Flight Tests. Rep. No. SM-14631, Douglas Aircraft Co., Inc., Jan. 3, 1953.

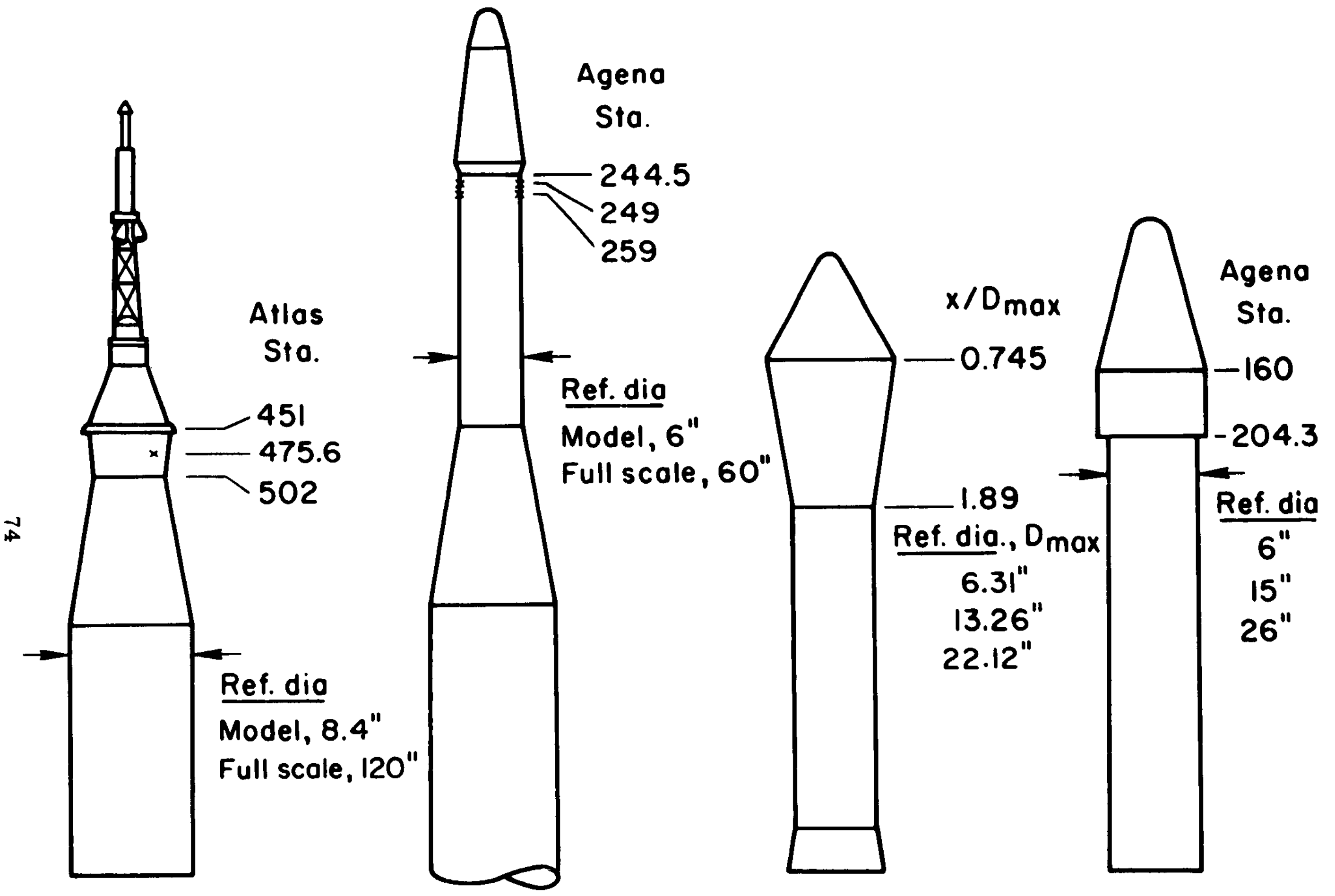

Mercury Atlas   Ranger 5   Model 8   Model 13a

Figure 1.- Models investigated for scale effects.

CONFIDENTIAL

Figure 2.- Photograph of 7-percent scale Mercury model.

CONFIDENTIAL

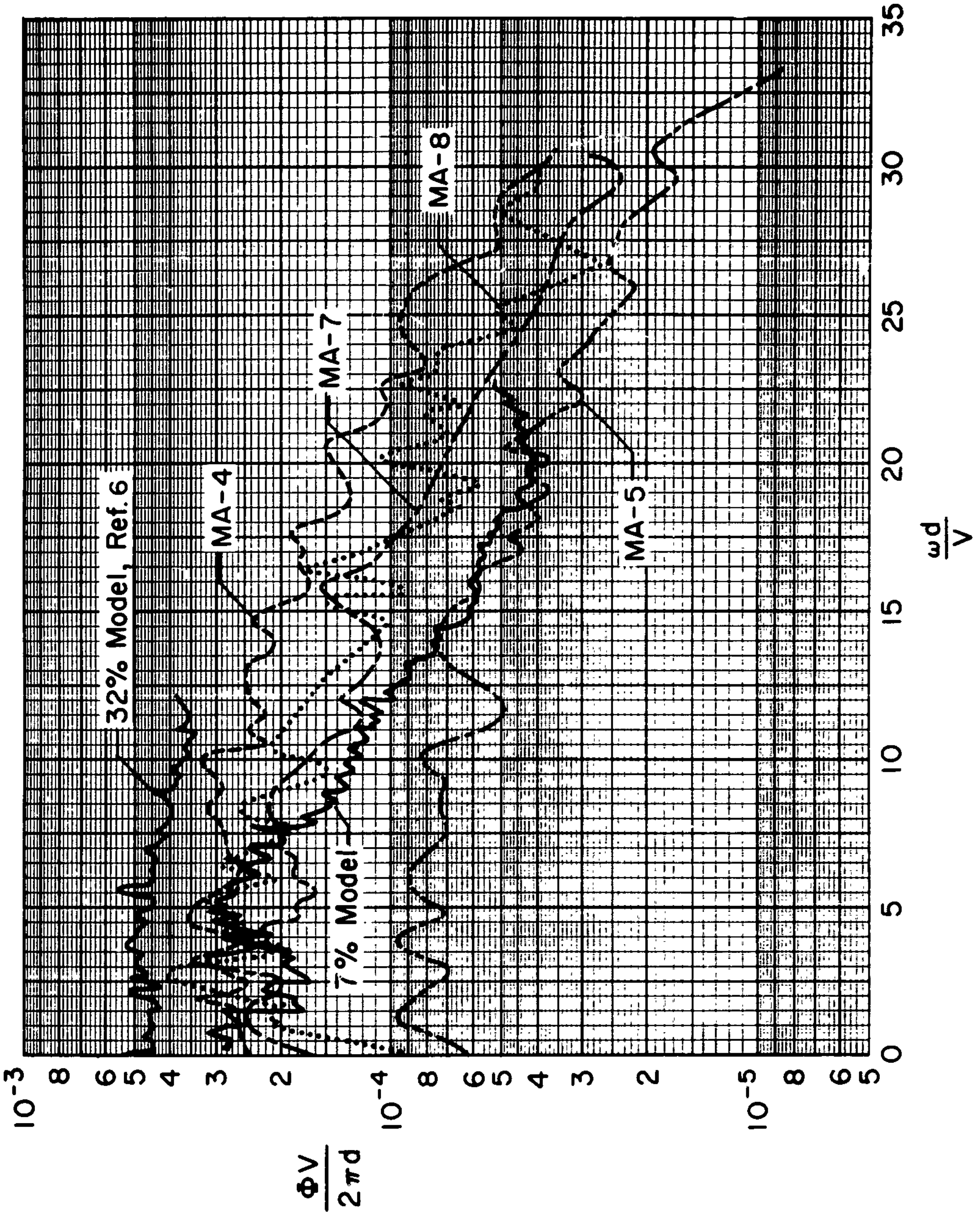

Figure 3.- Power spectra of pressure fluctuations on the Mercury-Atlas adapter near M = 1.

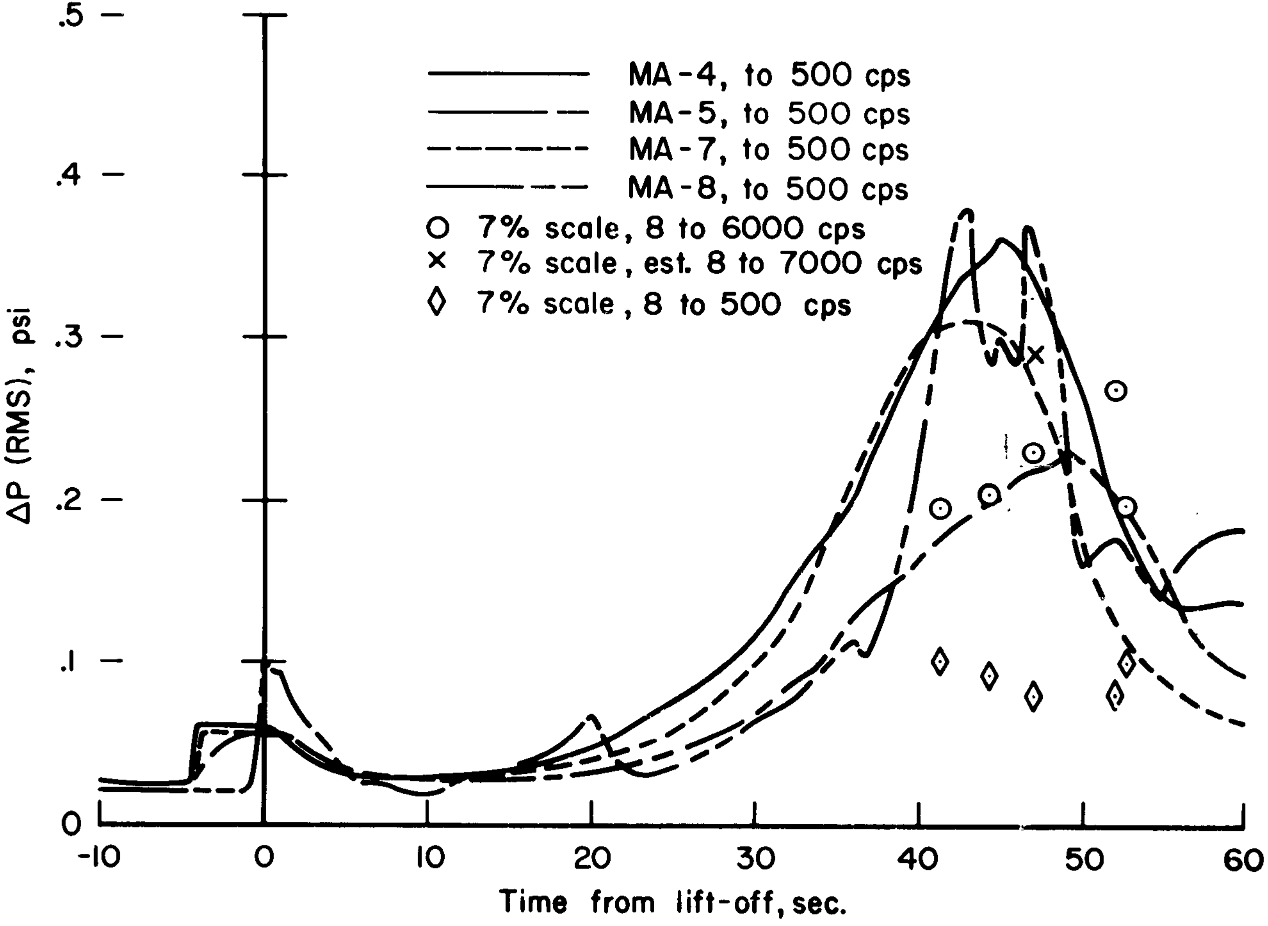

Figure 4.- Time history of pressure fluctuations on the Mercury-Atlas adapter.

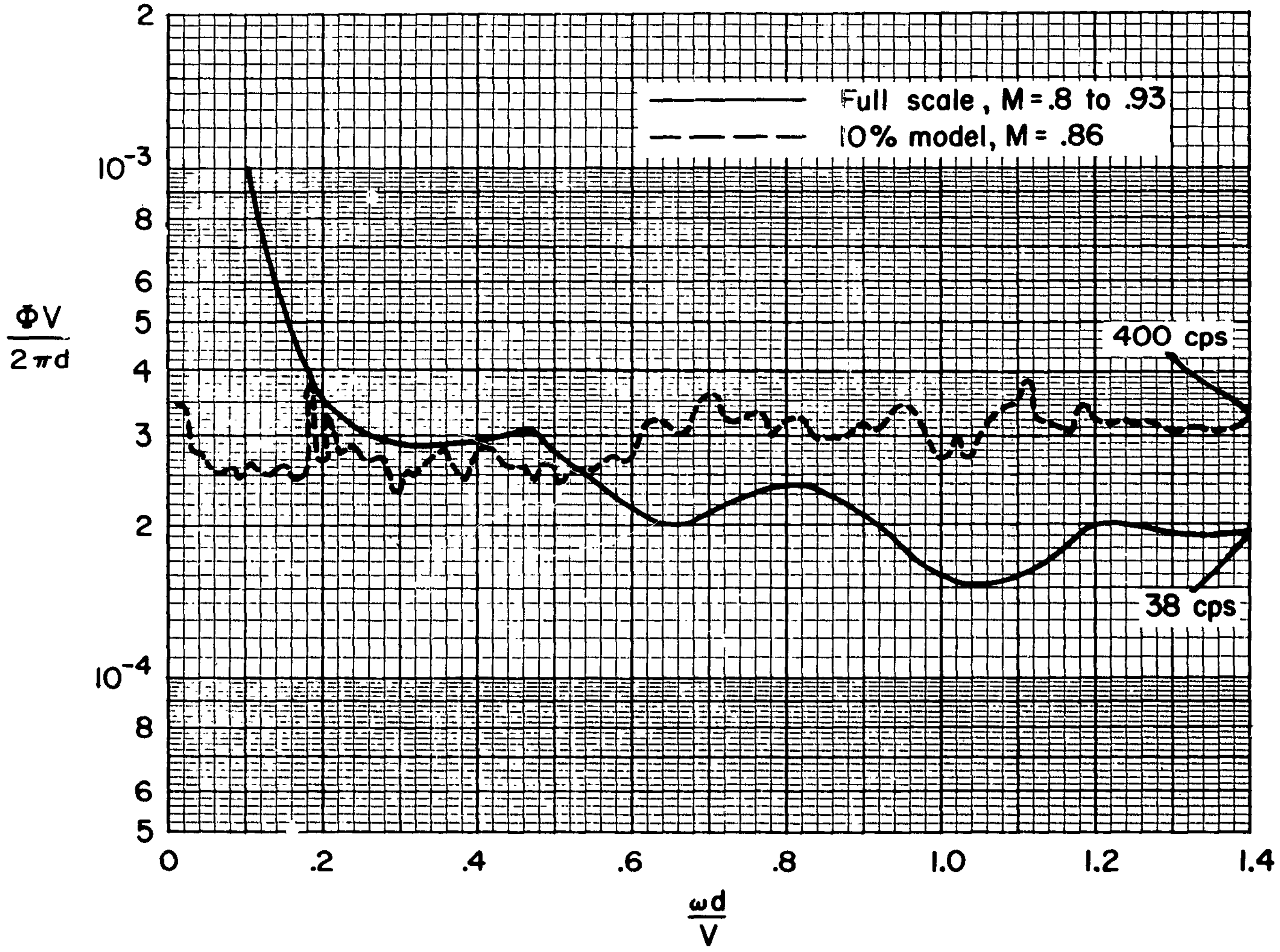

(a) Agena sta. 249.

Figure 5.- Power spectra of differential pressure fluctuations on the Agena with the Ranger 5 payload.

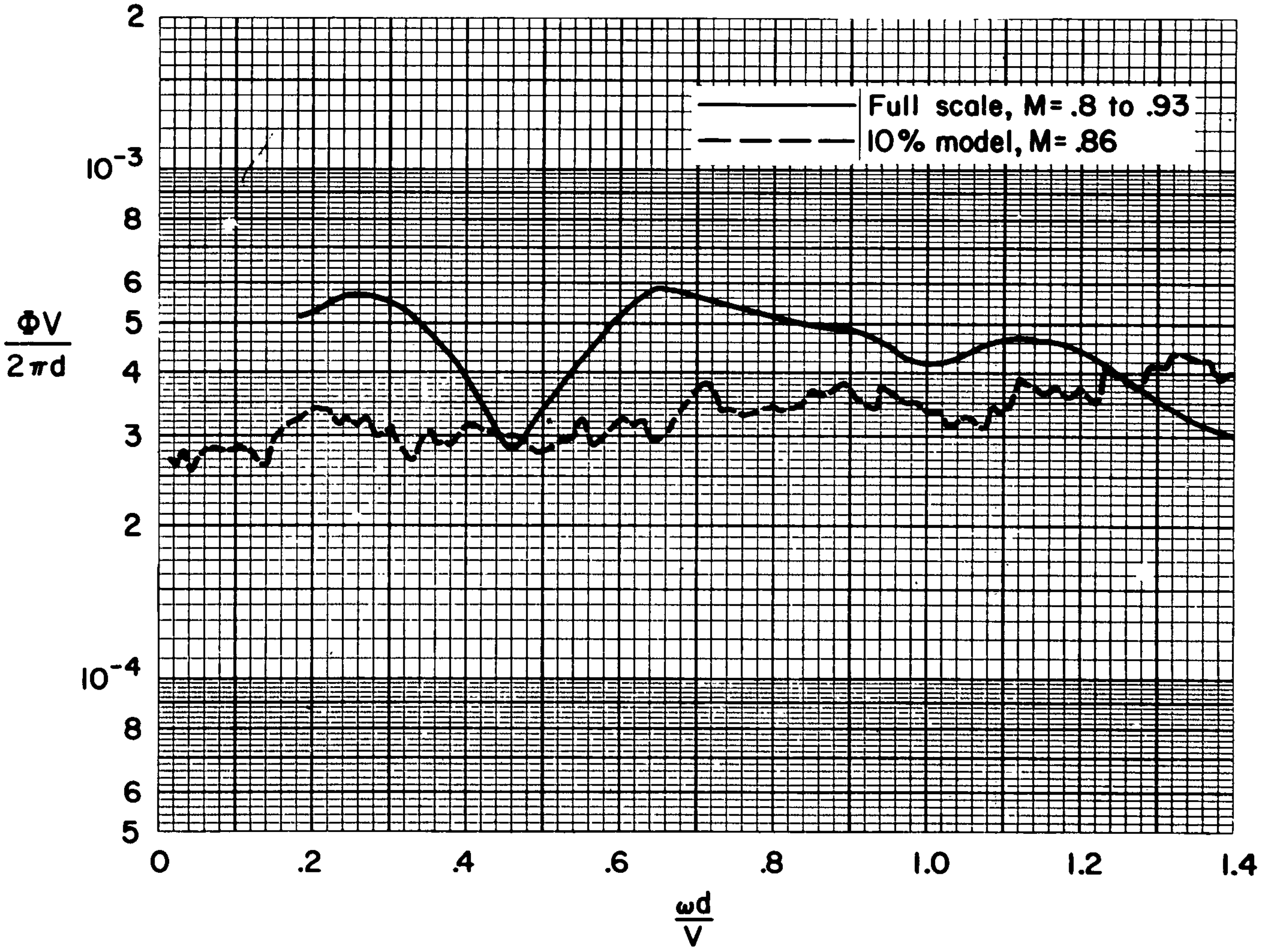

(b) Agena sta. 259.

Figure 5.- Concluded.

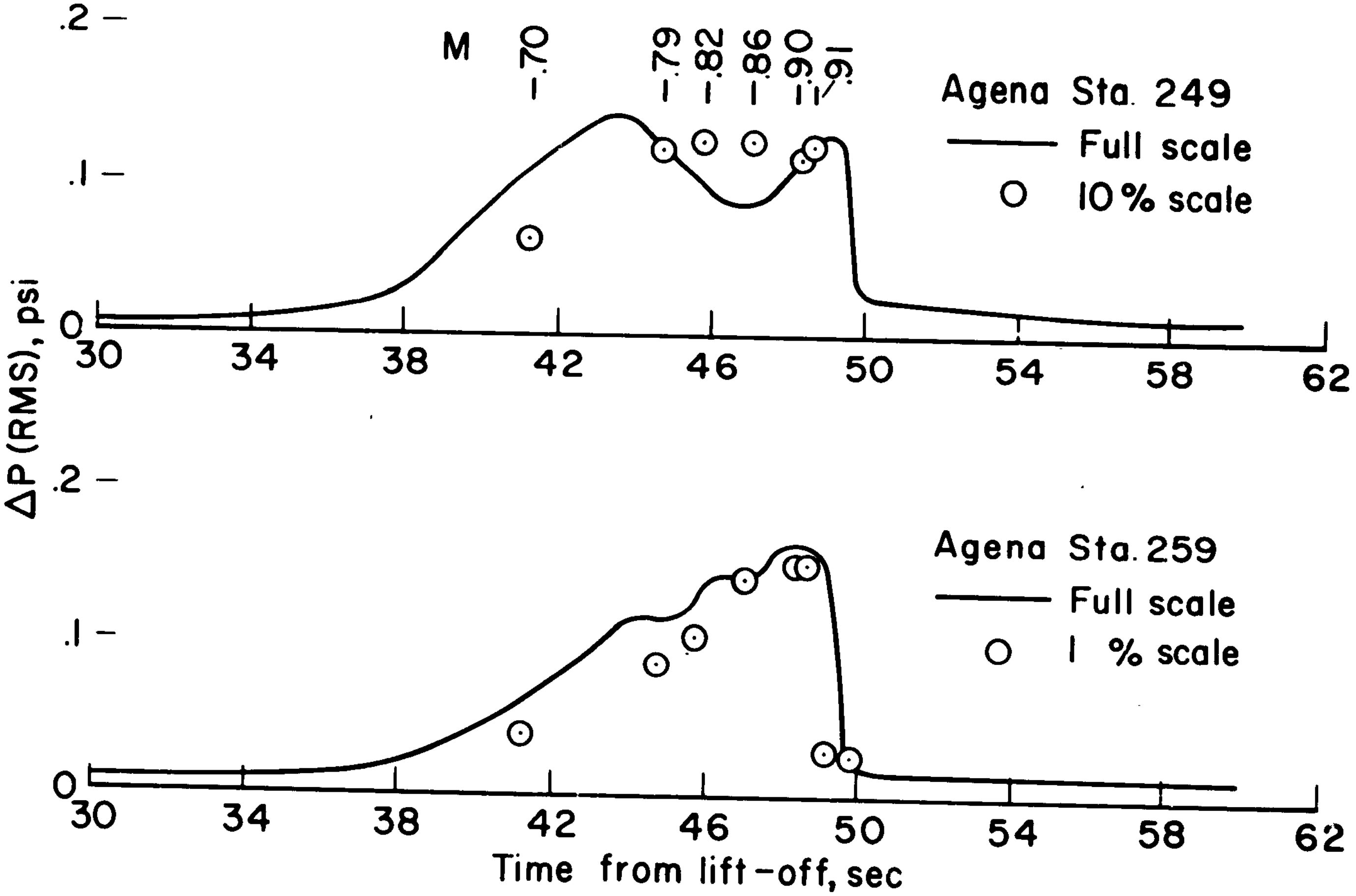

Figure 6.- Time histories of differential pressure fluctuations on the Agena with the Ranger 5 fairing.

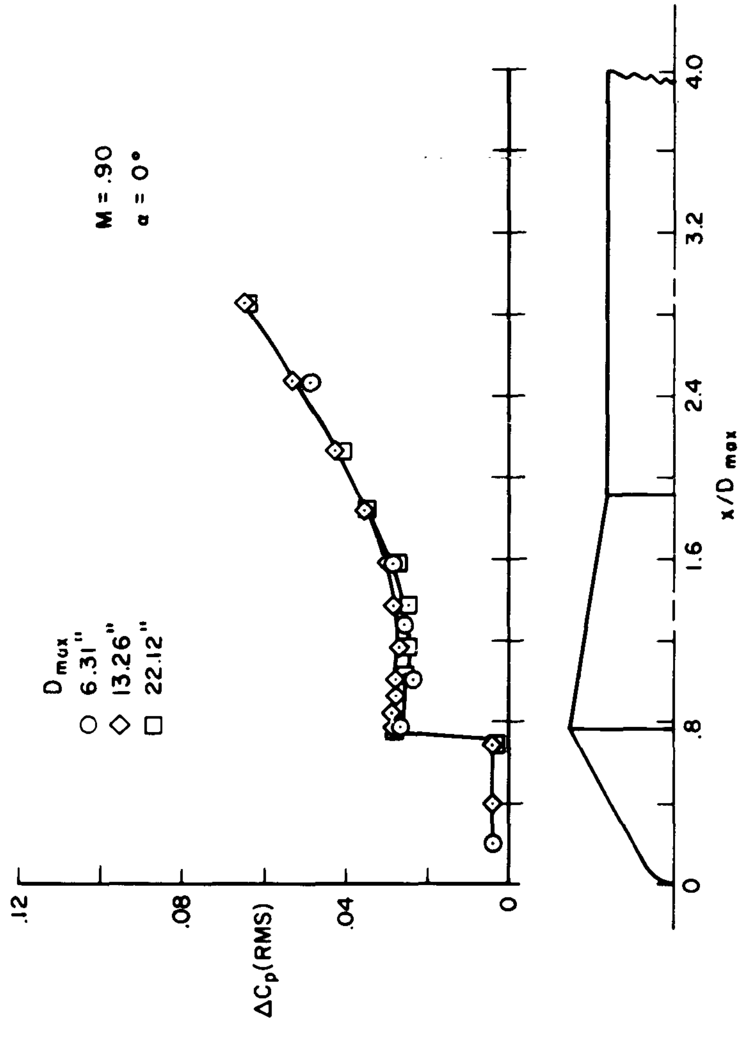

Figure 7.- Effect of scale on model 8 pressure fluctuations.

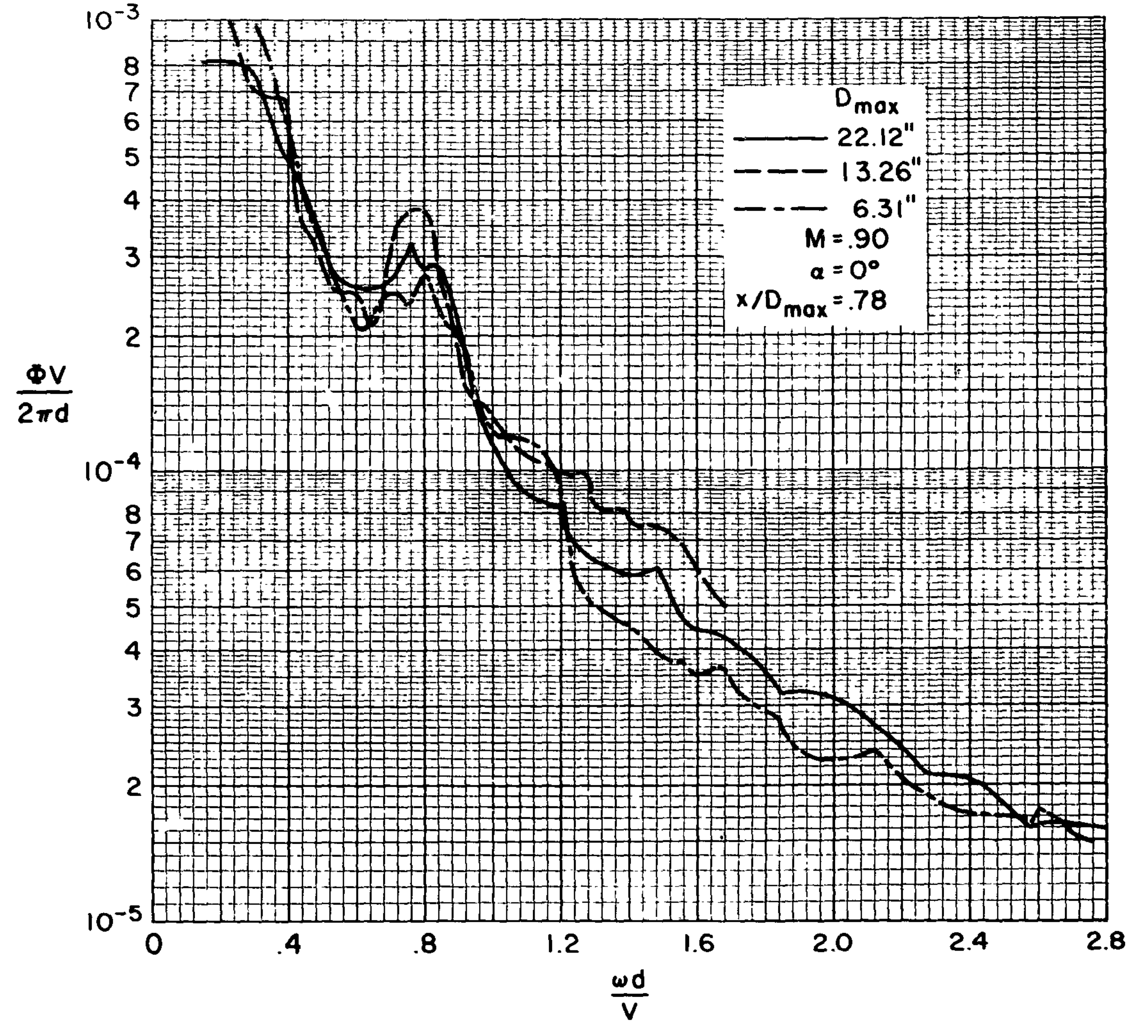

Figure 8.- Power spectra of pressure fluctuations on model 8.

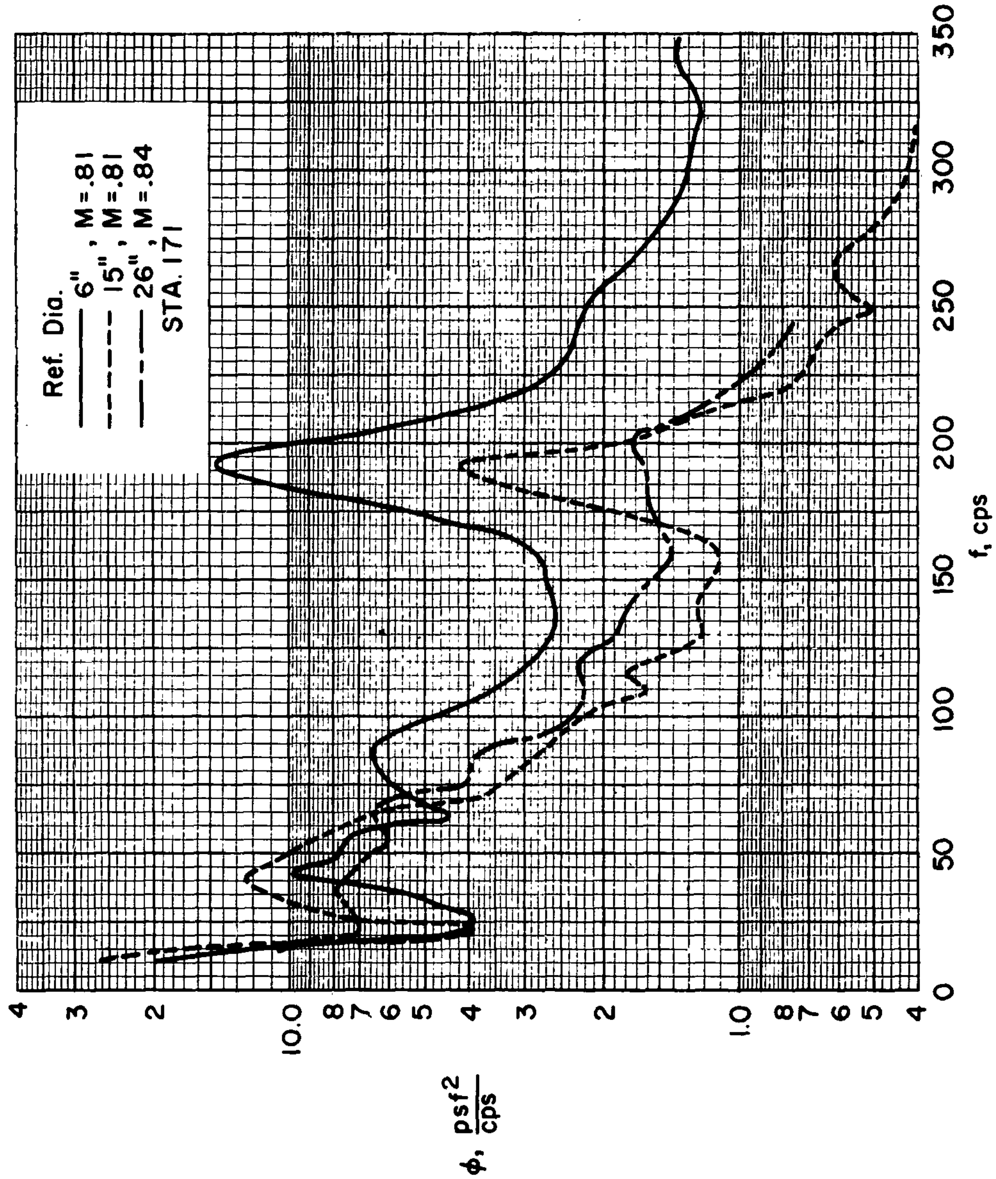

Figure 9.- Model 13a power spectra in region of a shock wave.

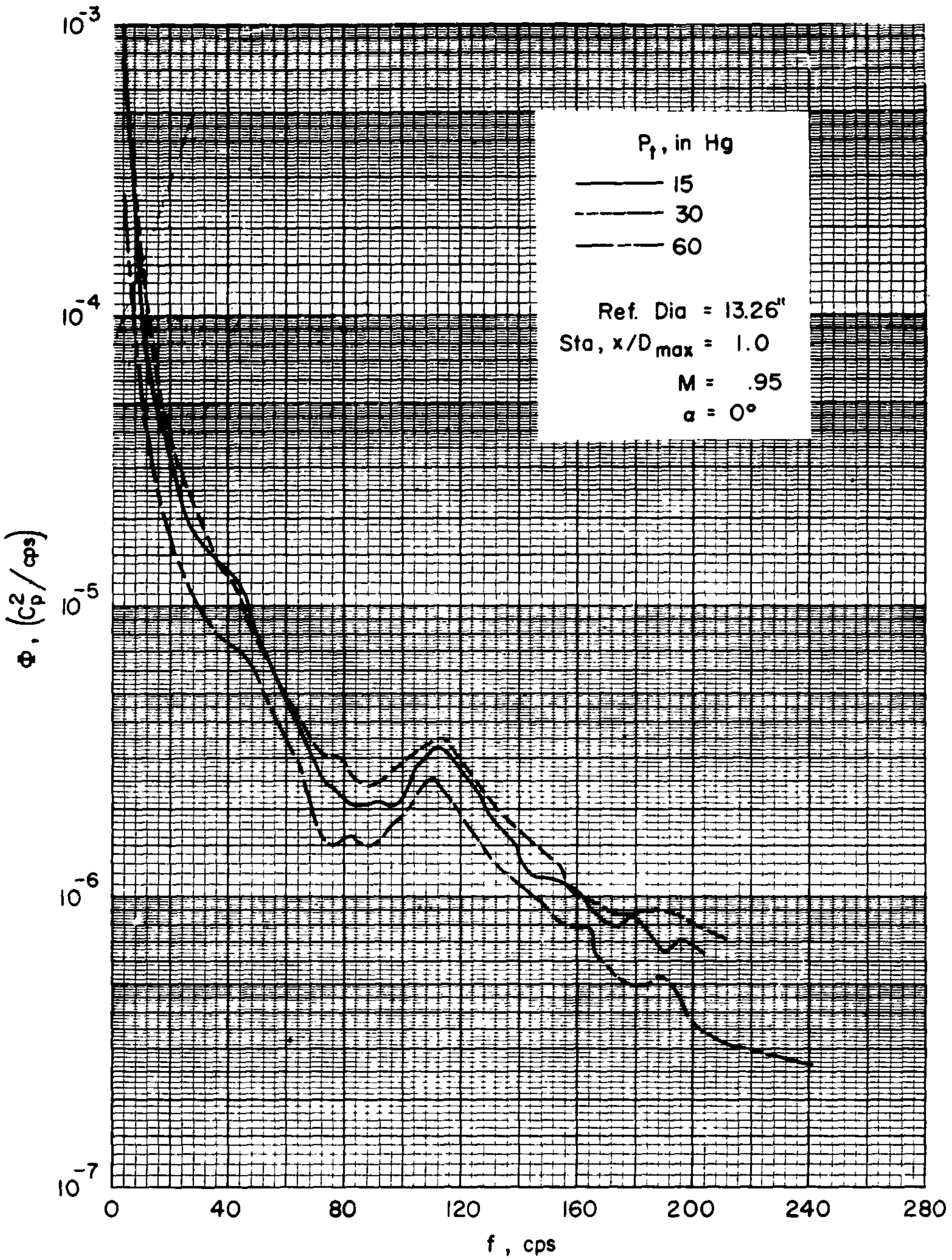

Figure 10.- Effect of total pressure on power spectra of differential pressure fluctuations on model 8.

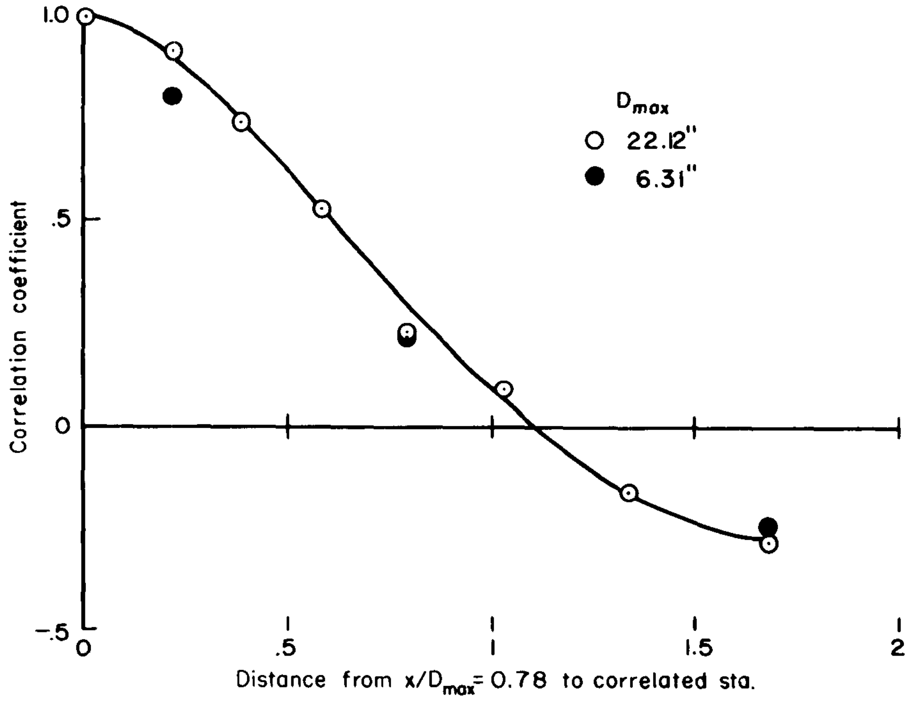

Figure 11.- Longitudinal correlation of pressure-fluctuation measurements on model 8.

SESSION VI

AIRCRAFT APPLICATIONS

Chairman: Dr. Holt Ashley
Massachusetts Institute of Technology

FLUTTER MODEL APPROACHES FOR HIGH PERFORMANCE AIRCRAFT

J. R. Stevenson

Supervisor, Structural Dynamics Group
North American Aviation, Inc., Los Angeles Division

ABSTRACT

Applications of flutter models in the design of high performance aircraft are discussed in the following areas: the role of flutter models, scale factors, design and fabrication, support system requirements and stability and control for complete air vehicle models, influence coefficients measurements, vibration measurements, flutter test instrumentation, safety devices, tunnel flow roughness and flutter testing. Information is presented on new construction materials and processes including a nickel-plating technique for the application of external skins, a novel support system for subsonic, transonic and supersonic complete air vehicle models, a novel wind tunnel dynamic pressure reduction safety device, and an automatic system for influence coefficients data gathering on IBM punched cards.

NOMENCLATURE

b = reference half-chord length

ω = circular frequency

V = true velocity

μ = mass ratio, $\frac{M}{\pi \rho b^2}$; Poisson's ratio, $G/_E$

E = modulus of elasticity

G = modulus of rigidity

I = bending moment of inertia; mass moment of inertia

J = torsional stiffness constant

t = structural thickness

q = dynamic pressure, $1/2 \rho V^2$

M = margin built into a flutter model, %/100; Mach number; total mass

ρ = air density

ρ_s = density of structural material

I_1 = bending moment of inertia per unit length

m = mass per unit length

δ = static deflection or deflection

K = linear spring constant

C = rotational spring constant

A = area

d = thickness of solid model structure

CG = center of gravity

EC = elastic center

AC = aerodynamic center

Subscripts

M	denotes model
F	denotes full scale
0	refers to centroidal axis
A	denotes actual
S	denotes structure

LIST OF ILLUSTRATIONS

INTRODUCTION

The prevention of flutter in high performance aircraft has become a design problem of continually increasing importance as flight boundaries have expanded. This has been so, not only as a result of the speed increases, but also as a result of air vehicle configurational changes dictated by the broadened operational environment. Inherent stiffness and consequently flutter speeds have tended to be lower as structural thickness ratios have decreased, structural temperatures have increased, and new alloys with higher strength to stiffness ratios have been developed. And this has not been completely offset by the generally favorable effects on stiffness and aerodynamic parameters of the trend toward reduced aspect ratios of airfoil surfaces. The net result of these trends has been a tendency for limit speeds to approach and in many cases to exceed inherent flutter boundaries resulting from strength requirements alone

Prior to the advent of supersonic speeds, designs satisfying strength requirements were frequently adequate from the flutter standpoint except possibly for control surface mass balancing and approximate flutter analyses usually sufficed to ensure that flutter boundaries were well in excess of limit speeds. Now the basic structural gages, skin panel parameters, control surface stiffness levels and indeed the overall configurations are frequently affected by flutter considerations. This, together with the increased emphasis on design optimization, the increased cost and the reduced susceptibility of sophisticated high performance aircraft structures to quick fixes have made accurate and rapid flutter prediction techniques an economic necessity. Furthermore, the accurate prediction of flutter boundaries has assumed greater importance in minimizing the cost and risk of flight testing.

However, a number of factors have combined to make accurate flutter predictions more difficult and time consuming: (1), The trend toward low aspect-ratio plate like structures has increased the difficulty of obtaining accurate analytical determinations of structural stiffness; (2), There has been a tendency for design evolutions to outstrip the development of unsteady aerodynamic theories, and (3), The increased air vehicle complexity and the greater number of conditions requiring analysis have combined to greatly extend the time and effort required for comprehensive flutter evaluations.

In these circumstances, experimental and analytical approaches must be carefully combined to obtain adequate and timely solutions for flutter design development problems.

The present paper is limited to a discussion of some of the problems encountered in the application of flutter models to the design of high performance aircraft and techniques we have employed in their solution.

THE ROLE OF FLUTTER MODELS

In flutter, as in other fields of engineering, experimental and analytical methods complement each other and the proper balance and timing between analytical and experimental efforts to obtain an adequate engineering answer for the minimum expenditure must be determined for each problem on the basis of prior knowledge and experience subject to revision as the problem unfolds.

Flutter model tests have the following specific functions:

1. To verify analytical natural vibration mode and flutter prediction methods.

2. To evaluate methods for computing structural stiffness.

3. To obtain flutter boundaries by direct measurement

4. To investigate parameter trends

Flutter models may be classified in two broad categories. One includes the simple trend models and the other the detailed models of an actual design. The simple cantilever trend model results can provide approximate or preliminary indications of Mach number and other parameter trends of great value in formulating a more comprehensive attack on the flutter problem and, in conjunction with detailed complete air vehicle analyses and low speed model test results, can be used to determine flutter boundaries when margins are not too small. When greater accuracy is required, tests of detailed component models covering the range of Mach numbers can be used to supplant the trend model results. Of course, where coupling effects between components are not small, adequate margins from detailed component model tests become reassuring preliminary results which must be supplemented by complete air vehicle analyses, using methods which correlate with model results, and/or high speed tests of complete air vehicle models.

SCALE FACTORS

For a flutter model to be a good dynamic representation of a full scale structure, the full scale stiffness and mass distributions and the external geometry must be simulated with sufficient accuracy. In addition, there should be a one-to-one correspondence of $\frac{b\omega}{V}$, M and μ. It generally is not possible to simulate the full scale Reynolds number but the effect of this discrepancy on flutter probably is small, except for investigations of stall flutter, if model Reynolds numbers are above the critical value.

It is interesting to note that flutter speeds are independent of size. This can be seen from the facts that flutter occurs for some value of the non-dimensional parameter $\frac{b\omega}{V}$ and that structural frequencies vary inversely with size b, thus maintaining a constant value of $b\omega$ and hence flutter velocity V.

There are basically two methods for obtaining stiffness simulation in the conversion of full scale structures to model scale. One is the direct scaling of the full scale structure and the other is by indirect scaling through the use of various stiffness coefficients. The method of direct scaling is employed for structures where one-dimensional stiffness coefficients (EI, GJ, etc.) are not applicable, for models which are also to be used to define or check full scale stiffness and for high speed models where the correct mass ratios must be simulated. The method of indirect scaling is employed primarily in the design of the smaller details of models which are otherwise directly scaled, for simple research models and for low speed models which can be described in terms of one-dimensional stiffness coefficients and for which mass ratio simulation can be achieved with structures of relatively low stiffness to weight ratios.

In general, direct scaling tends to be more accurate and model construction may be accomplished in a shorter overall time span since fewer analytical manipulations of the structure are required.

Some of the most useful and important relationships between flutter model and full scale structures are summarized as follows:

$$\frac{t_M}{t_F} = \frac{b_M}{b_F}\,\frac{E_F}{E_M}\,\frac{q_M}{q_F}\,\frac{1}{(1+M)^2} \tag{1a}$$

$$\frac{t_M}{t_F} = \frac{b_M}{b_F}\,\frac{G_F}{G_M}\,\frac{q_M}{q_F}\,\frac{1}{(1+M)^2} \tag{1b}$$

$$\frac{M_M}{M_F} = \left(\frac{b_M}{b_F}\right)^3 \frac{\rho_M}{\rho_F} \tag{2a}$$

$$\frac{m_M}{m_F} = \left(\frac{b_M}{b_F}\right)^2 \frac{\rho_M}{\rho_F} \tag{2b}$$

$$\frac{\omega_M}{\omega_F} = \frac{b_F}{b_M}\,\frac{V_M}{V_F}\,\frac{1}{(1+M)} \tag{3}$$

$$\frac{\delta_M}{\delta_F} = \frac{b_F}{b_M}\,\frac{q_F}{q_M}\,(1+M)^2 \tag{4}$$

$$\frac{K_M}{K_F} = \frac{b_M}{b_F}\,\frac{q_M}{q_F}\,\frac{1}{(1+M)^2} \tag{5}$$

$$\frac{C_M}{C_F} = \left(\frac{b_M}{b_F}\right)^3 \frac{q_M}{q_F}\,\frac{1}{(1+M)^2} \tag{6}$$

$$\frac{J_M}{J_F} = \left(\frac{b_M}{b_F}\right)^4 \frac{G_F}{G_M}\,\frac{q_M}{q_F}\,\frac{1}{(1+M)^2} \tag{7}$$

$$\frac{I_M}{I_F} = \left(\frac{b_M}{b_F}\right)^4 \frac{E_F}{E_M} \frac{q_M}{q_F} \frac{1}{(1+M)^2} \tag{8}$$

$$\frac{A_M}{A_F} = \left(\frac{b_M}{b_F}\right)^2 \frac{E_F}{E_M} \frac{q_M}{q_F} \frac{1}{(1+M)^2} \tag{9}$$

$$d_M = \left[12\, I_{1_F} \left(\frac{b_M}{b_F}\right)^3 \frac{E_F}{E_M} \frac{q_M}{q_F} \frac{1}{(1+M)^2}\right]^{1/3} \tag{10}$$

Model structural gages may be computed directly from full scale gages using equations (1a) and (1b) wherein it is assumed that structural centroids are matched and errors in I_{OM}/I_{OF} can be minimized sufficiently by proper choice of model materials. Where the full scale Poisson's ratio is not exactly simulated by the model material, better accuracy is obtained by using eq (1a) for members primarily loaded in bending and eq (1b) for members primarily loaded in shear. Relations (2a) and (2b) give the total and running ratios of model to full scale mass respectively. The ratio of frequencies is specified by relation (3) and it can be seen that the reduced frequency parameter is simulated exactly only when the margin M built into the model is zero. However, it is common practice to build some margin (say $M = .15$) into high speed models so that the desired stiffness margin can be demonstrated, in tests at constant Mach number, for the correct mass ratio. The ratio of static deflections is given by eq (4). Equations (5), (6), (7) and (8) give the ratio of linear spring constant, rotational spring constant, torsion constant and moment of inertia respectively. Equation (9) specifies the area ratio for tension-compression members such as spar caps, longerons, etc. Equation (10) can be used to calculate the thickness of solid homogeneous model structures to simulate the full scale EI.

It is interesting to note that fuel slosh frequencies vary inversely as the square root of size while structural frequencies vary inversely as the first power of size. It can be shown, therefore, that slosh frequencies are properly simulated when full scale static deflections are properly scaled.

DESIGN AND FABRICATION

An examination of the fact that flutter speeds are independent of size can provide some insight into the basic problems faced in the design and fabrication of flutter models. For example, if we were to conduct model tests in the atmosphere using free-flight or sled techniques, all we would have to do is duplicate the full scale structure to some reduced scale in all important details using full scale materials and we would have a unity speed scale flutter model.

One problem that might be encountered is that the model structural gages, having been scaled according to the geometrical scale factor, would be too thin to fabricate. We might solve this problem by using a material with a lower modulus of elasticity requiring correspondingly greater thickness to provide equivalent stiffness. But the substitute material would have to have a stiffness to density ratio equal to or greater than that of the full-scale material or the required weight could not be met. Also, since the full-scale structures are designed to be as efficient as possible in terms of strength to weight ratio and/or stiffness to weight ratio and the materials employed generally have a high stiffness to density ratio, less efficient but larger gage concentrated spar types of model construction offer no possibility of meeting the required mass ratio unless some material with an ultra-high stiffness to density ratio such as beryllium is used.

For models designed for testing in wind tunnels the problems are quite similar and may be stated by considering the pertinent scale factors. The scale factor for required model mass is

$$\frac{M_M}{M_F} = \left(\frac{b_M}{b_F}\right)^3 \frac{\rho_M}{\rho_F} \tag{2a}$$

and the scale factor for actual model mass is

$$\frac{M_{M_A}}{M_{F_A}} = \frac{\rho_{s_M}}{\rho_{sF}} \; \frac{t_M}{t_F} \left(\frac{b_M}{b_F}\right)^2 \tag{11}$$

Substituting the expression for t_M/t_F from eq (1a) into eq (11) gives

$$\frac{M_{M_A}}{M_{F_A}} = \left(\frac{E}{\rho_s}\right)_F \left(\frac{1}{E/\rho_s}\right)_M \left(\frac{b_M}{b_F}\right)^3 \frac{\rho_M}{\rho_F} \left(\frac{V_M}{V_F}\right)^2 \frac{1}{(1+M)^2} \tag{12}$$

Equating actual and required mass scale factors gives

$$\left(\frac{E}{\rho_s}\right)_M = \left(\frac{E}{\rho_s}\right)_F \left(\frac{V_M}{V_F}\right)^2 \frac{1}{(1+M)^2} \tag{13}$$

Assuming, for example, a transonic model designed for a blowdown tunnel using air, the ratio of V_M/V_F might be approximately .95 and with a built-in margin of 15%

$$\frac{(E/\rho_s)_M}{(E/\rho_s)_F} = (.95)^2 \frac{1}{(1.15)^2} = .683 \tag{14}$$

This represents the minimum model to full scale ratio of E/ρ_s, for the assumed conditions, that can be used without exceeding the required weight. For a low speed model eq (13) with $M = 0$ can be solved for the maximum velocity scale that can be achieved for given structural materials without exceeding the required weight to yield

$$\left(\frac{V_M}{V_F}\right)_{MAX} = \left[\frac{(E/\rho_s)_M}{(E/\rho_s)_F}\right]^{1/2} \tag{15}$$

An examination of eq (1a) shows that to maximize model gages the models should be as large as possible, be built of materials with low moduli of elasticity, be tested in tunnels capable of high dynamic pressures and not have excessively large built-in margins.

In summary, model construction materials with low elastic moduli and high stiffness to density ratios are desired. Table I lists some of the important properties of materials we have used in flutter model construction along with those for a typical full scale material (steel) for comparison.

TABLE I
MATERIAL PROPERTIES

MATERIAL	E 10^6PSI	G 10^6PSI	$\mu = G/E$	ρ_s LB/IN.^{3}	E/ρ_s 10^6IN.
Steel (PH 15-7 Mo)	29.5	11.4	.39	.28	105
Isowood (23 lb/ft.^{3})	.0576	.0221	.38	.0133	4.34
Isowood (30 lb/ft.^{3})	.0935	.0345	.37	.0171	5.48
Styrofoam (4.5 lb/ft.^{3})	.00633	.00225	.35	.00211	3.00
Al. Foil (5052)	10.3	3.9	.38	.10	103
Nickel (Electroplated)	20*	7.98*	.40	.312	64
Al. (7075)	10.6	4.0	.38	.10	106
Magnesium	6.5	2.4	.37	.065	100

* Higher values can be obtained by varying plating bath.

Isowood is a synthetic isotropic material developed and manufactured to our specifications by our Space and Information Systems Division specifically for flutter model applications. This material, due to its low stiffness and low stiffness to density ratio, is suitable primarily for low speed models. For high speed models, we have developed a technique of electroplating external skins of nickel over a Styrofoam core containing inlays in denser materials representing spars, ribs, bulkheads, etc. to obtain highly detailed directly scaled models. The advantages of the nickel plating technique are that one piece skins simulating complex tapers and compound curves can be plated and to lower stiffness or Et values than are practical with the aluminum foil technique.

Some examples of model construction are shown in Figures 1 through 6. The low speed solid Styrofoam models shown in Figure 1 were designed to simulate the full scale EI per unit length throughout the planform by the application of eq (10). Many small lead weights are imbedded in the Styrofoam to obtain the required mass distribution. Because of the short time span required for design and construction, we have found this type of model to be very suitable for preliminary design studies. Figure 2 shows some detailed skins and frames machined in Isowood and Styrofoam for directly scaled low speed flutter models. In some cases an internal sealant is applied so that wet fuel can be used. The minimum practical gage in Isowood is approximately 0.020 inches. The internal structures of some directly scaled high speed models are shown in Figure 3. Figure 4 shows a directly scaled low speed complete air vehicle model fabricated largely from Isowood and Styrofoam. Thin sheet as well as block types of Styrofoam were used in this application. High speed nickel plated flutter models are shown in Figure 5. In Figure 6, the upper portion shows an indirectly scaled low speed flutter model and the lower portion shows some of the external wing-mounted stores constructed for it. This model was constructed of many separate sections with each supported at a single point on a concentrated spar.

SUPPORT SYSTEM

The ideal wind tunnel suspension system for complete air vehicle flutter models may be defined as one with zero mass, stiffness and damping, capable of reacting the drag and normal forces without creating any aerodynamic disturbance and including very accurate automatic model position and attitude controls which will not affect the flutter characteristics to be determined. Needless to say, this is not the system to be described here. However, Figure 7 illustrates a novel suspension system design successfully employed in low speed and transonic tests of complete air vehicle flutter models that may come close enough to the ideal suspension for practical purposes. Utilizing only six torque bar springs, the system provides low frequencies in all rigid-body modes except fore-and-aft translation as well as essentially independently adjustable spring constants and elastic centers for vertical translation, side translation, pitch, yaw and roll.

In addition, the effective mass and damping can be held to very low values and the high degree of aerodynamic cleanliness is consistent with requirements for subsonic, transonic and supersonic testing. When required, remote control of pitch angle can be included in a straightforward manner. Accurate indications of suspension system normal force and pitching moment reactions, indispensable to intelligent model testing, can be obtained from strain gage bridges applied to the torque bars as will be explained later. Electrical leads from model strain gages, etc. are simply routed to the aft end of the model, bundled together and run through a sting downstream of the model with a suitable amount of slack between sting and model. Drag loads are carried on a pair of cables connected to a whiffle tree upstream. The whiffle tree is supported by a cable sling. A pair of cables with coil springs is used to preload and stabilize the whiffle-tree-sling assembly. These springs contribute to the suspension yaw stiffness.

Each of the torque bar assemblies is identical in design arrangement. A typical assembly is illustrated in Figure 8. The outer shell is a stiff steel tube of square cross-section. An irreversible worm gear drive provides a means of rotating the square tube about its longitudinal center line in bearings fixed to wind tunnel structure. The torque bar spring is a solid steel shaft of hexagonal cross-section mounted concentrically inside of the square outer shell and keyed to the outer shell by a hollow block machined with a slip fit to the proper shape. The keying block may be moved along the longitudinal axis of the spring and locked in place by means of a cable and pulley system and a series of set screws respectively to change the torque bar effective length. A sector is rigidly attached to an adapter collar fitted to the exposed end of the torque bar and the adapter collar is supported in ball bearings on each side of the sector. A cable attachment including a turnbuckle is fastened to the sector near the hub and a light weight cable of the proper length is routed over the sector to the model. A swaged ball on the end of the cable seats in a fitting built into the model. The spring constant can be adjusted by sliding the keying block to change the torque bar effective length and the spring preload can be changed by rotating the outer shell with the irreversible worm gear.

The worm gears on the forward and aft upper and lower torque bar assemblies can be interconnected by shafting and appropriate gearing and driven by an electric motor to obtain remotely controlled pitch rotation about an axis coincident with the location of the center support cables as illustrated in Figure 7.

The cable attach fittings in the model can be designed to react the rigging preloads in direct tension and hence can be both compact and light in weight and their weight can usually be completely absorbed as part of the required model ballast.

For symmetric flutter, suspension system effective mass is one-third of the drag cable mass, the total vertical cable mass and the effective mass of the sectors and torque bar springs. The effective mass of a sector and torque bar spring is

$$M_e = \frac{I}{r^2} \qquad (16)$$

where I = mass moment of inertia of sector plus torque bar spring about the axis of rotation

and r = sector radius

Due to its small radius of gyration, the torque bar spring makes a negligible contribution to M_e and the sector contribution can be minimized by careful design. For the antisymmetric case the effective mass of the suspension system is extremely low being only one-third of the vertical cable mass, one-third of the drag cable mass for lateral translation and the total drag cable mass plus the effective mass of the whiffle-tree assembly including the stabilizing cables and springs, in yaw. In practice, ratios of suspension effective mass (including the effective mass of electrical leads) to total model mass of only 0.021, 0.003 and 0.014 have been obtained for pitch and vertical translation, roll and lateral translation, and yaw modes respectively.

When coil springs are used to suspend a model, some compromise on spring stiffness may be required to remove the coil surge frequencies from the flutter frequency range to prevent coil surge from seriously affecting the flutter characteristics. This problem has been eliminated through the use of torque bar springs.

Spring constant formulas for the symmetric rigid-body modes are given below.

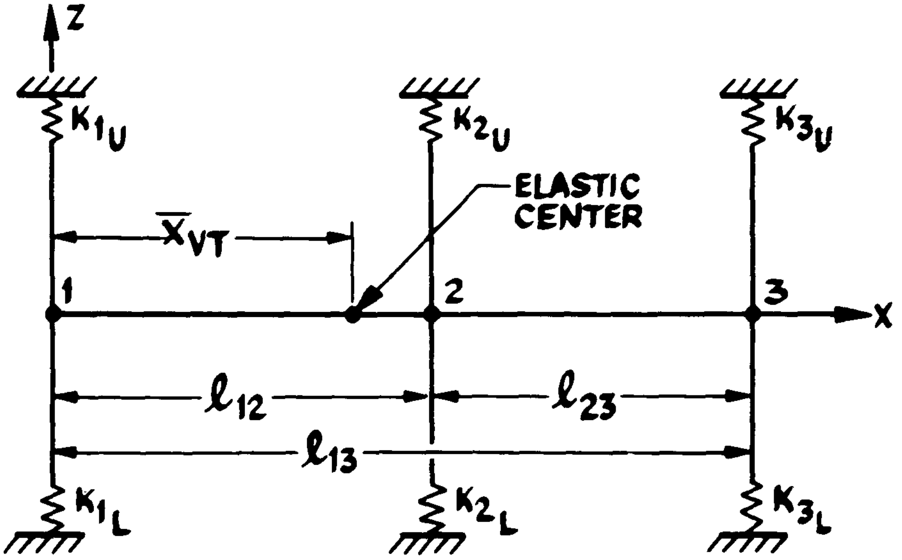

Figure 9 Suspension notation for symmetric modes

Referring to Figure 9

$$\left.\begin{aligned} K_{1_V} &= K_{1_U} + K_{1_L} \\ K_{2_V} &= K_{2_U} + K_{2_L} \\ K_{3_V} &= K_{3_U} + K_{3_L} , \end{aligned}\right\} \tag{17}$$

the spring constant in vertical translation is

$$K_{VT} = K_{1V} + K_{2V} + K_{3V} , \tag{18}$$

the elastic center is given by

$$\bar{X}_{VT} = \frac{K_{2V}\,\ell_{12} + K_{3V}\,\ell_{13}}{K_{1V} + K_{2V} + K_{3V}} \tag{19}$$

and the pitch stiffness about the elastic center is given by

$$C_P = K_{1V}\left(\bar{X}_{VT}\right)^2 + K_{2V}\left(\ell_{12} - \bar{X}_{VT}\right)^2 + K_{3V}\left(\ell_{13} - \bar{X}_{VT}\right)^2 . \tag{20}$$

Rearranging, we obtain

$$K_{1V} + K_{2V} + K_{3V} = K_{VT} \tag{18}$$

$$\left(\bar{X}_{VT}\right) K_{1V} + \left(\bar{X}_{VT} - \ell_{12}\right) K_{2V} + \left(\bar{X}_{VT} - \ell_{13}\right) K_{3V} = 0 \tag{19}$$

$$\left(\bar{X}_{VT}\right)^2 K_{1V} + \left(\ell_{12} - \bar{X}_{VT}\right)^2 K_{2V} + \left(\ell_{13} - \bar{X}_{VT}\right)^2 K_{3V} = C_P \tag{20}$$

Equations (18), (19), and (20) can be solved for K_{1V}, K_{2V} and K_{3V} when the required values of K_{VT}, $\bar{X}_{VT}$ and C_P are given.

For the purpose of illustrating the development of spring constant formulas for the antisymmetric rigid-body modes, it shall be assumed for simplicity that all vertical cable lengths are equal.

Referring to Figure 10, the following set of equations is derived for calculating the model dead weight reactions at each of the three support points.

$$W_1 + W_2 + W_3 = W \tag{21}$$

$$\left(\bar{X}_{CG}\right)W_1 + \left(\bar{X}_{CG} - \ell_{12}\right) W_2 + \left(\bar{X}_{CG} - \ell_{13}\right) W_3 = 0 \tag{22}$$

$$\left(\bar{X}_{CG}\right)^2 W_1 + \left(\ell_{12} - \bar{X}_{CG}\right)^2 W_2 + \left(\ell_{13} - \bar{X}_{CG}\right)^2 W_3 = I_P \tag{23}$$

The differences of upper and lower cable tensions are given by

$$\left.\begin{aligned} T_{1_U} - T_{1_L} &= W_1 \\ T_{2_U} - T_{2_L} &= W_2 \\ T_{3_U} - T_{3_L} &= W_3 \end{aligned}\right\} \tag{24}$$

where the upper tensions are taken positive upward and the lower tensions are taken positive downward.

Referring to Figure 11, the lateral stiffness of one of the support points is given by

$$K_L = \frac{T_U \sin\Theta}{\delta} + \frac{T_L \sin\Theta}{\delta}$$

$$\text{but} \quad \delta = \ell\Theta$$

$$\text{and} \quad K_L = \frac{T_U}{\ell} + \frac{T_L}{\ell} = \frac{T_U + T_L}{\ell}$$

for small deflections. Then

$$\left.\begin{aligned} K_{1_L} &= \frac{T_{1U} + T_{1L}}{\ell} \\ K_{2_L} &= \frac{T_{2U} + T_{2L}}{\ell} \\ K_{3_L} &= \frac{T_{3U} + T_{3L}}{\ell} \end{aligned}\right\} \tag{25}$$

and the total spring constant in side translation is

$$K_{ST} = K_{1L} + K_{2L} + K_{3L} \tag{26}$$

The vertical location of the elastic center is given by

$$\bar{Z}_{ST} = \frac{\frac{1}{\ell}\left(T_{1_U} r_{1_U} - T_{1_L} r_{1_L}\right) + \frac{1}{\ell}\left(T_{2_U} r_{2_U} - T_{2_L} r_{2_L}\right) + \frac{1}{\ell}\left(T_{3_U} r_{3_U} - T_{3_L} r_{3_L}\right)}{K_{ST}} \quad (27)$$

where all r's are considered positive lengths.

If we stipulate that

$$\frac{T_U}{T_L} = \frac{r_L}{r_U} \quad (28)$$

for each of the three support points, each of the bracketed terms in eq (27) is zero, $\bar{Z}_{ST} = 0$ and the roll axis is coincident with the X axis. Referring to Figure 10, the fore-and-aft location of the elastic center is given by

$$\bar{X}_{ST} = \frac{K_{2L}\,\ell_{12} + K_{3L}\,\ell_{13}}{K_{1L} + K_{2L} + K_{3L}} \quad (29)$$

and the yaw stiffness about the elastic center is given by

$$C_Y = K_{1_L}\left(\bar{X}_{ST}\right)^2 + K_{2_L}\left(\ell_{12} - \bar{X}_{ST}\right)^2 + K_{3_L}\left(\ell_{13} - \bar{X}_{ST}\right)^2 \quad (30)$$

Referring to Figure 12, the restoring moment in roll for one of the three supports, assuming small deflections, is

$$M_r = T_U\, r_U \Theta_U + T_U\, r_U \Psi + T_L\, r_L \Theta_L + T_L\, r_L \Psi \quad (31)$$

The spring constant in roll is given by

$$C_r = \frac{M_r}{\Psi} = T_U\, r_U \left(1 + \frac{\Theta_U}{\Psi}\right) + T_L\, r_L\left(1 + \frac{\Theta_L}{\Psi}\right) \quad (32)$$

Since $\Theta_U << \Psi$ and $\Theta_L << \Psi$, K_r is given with sufficient accuracy by

$$C_r = T_U\, r_U + T_L\, r_L \quad (33)$$

Then for the complete suspension system the roll stiffness is given by

$$C_R = \left(T_{1_U} r_{1_U} + T_{1_L} r_{1_L}\right) + \left(T_{2_U} r_{2_U} + T_{2_L} r_{2_L}\right) + \left(T_{3_U} r_{3_U} + T_{3_L} r_{3_L}\right) \quad (34)$$

Referring to Figure 13, the contribution of the whiffle tree springs to yaw stiffness is

$$C_{Y_W} = 2 K_W d^2 \tag{35}$$

Summarizing, the equations for the antisymmetric spring constants are

$$K_{1L} + K_{2L} + K_{3L} = K_{ST} \tag{26}$$

$$\left(\bar{X}_{ST}\right) K_{1L} + \left(\bar{X}_{ST} - \ell_{12}\right) K_{2L} + \left(\bar{X}_{ST} - \ell_{13}\right) K_{3L} = 0 \tag{29}$$

$$\left(\bar{X}_{ST}\right)^2 K_{1L} + \left(\ell_{12} - \bar{X}_{ST}\right)^2 K_{2L} + \left(\ell_{13} - \bar{X}_{ST}\right)^2 K_{3L} = C_Y - 2K_W d^2 \tag{30}$$

and

$$C_R = \left(T_{1_U} r_{1_U} + T_{1_L} r_{1_L}\right) + \left(T_{2_U} r_{2_U} + T_{2_L} r_{2_L}\right) + \left(T_{3_U} r_{3_U} + T_{3_L} r_{3_L}\right) \tag{34}$$

For given values of K_{ST}, $\bar{X}_{ST}$, C_Y and K_W equations (26), (29) and (30) can be solved for the required values of K_{1L}, K_{2L} and K_{3L}. Combining eq (24) with eq (25) gives the following expressions for the cable tensions:

$$\left.\begin{aligned}
T_{1_U} &= \frac{W_1 + \ell K_{1L}}{2} \\
T_{1_L} &= \frac{\ell K_{1L} - W_1}{2} \\
T_{2_U} &= \frac{W_2 + \ell K_{2L}}{2} \\
T_{2_L} &= \frac{\ell K_{2L} - W_2}{2} \\
T_{3_U} &= \frac{W_3 + \ell K_{3L}}{2} \\
T_{3_L} &= \frac{\ell K_{3L} - W_3}{2}
\end{aligned}\right\} \tag{35}$$

Combining relations (28) and (34) gives

$$C_R = 2\left(T_{1_U} r_{1_U} + T_{2_U} r_{2_U} + T_{3_U} r_{3_U}\right) \tag{36}$$

If we assume $r_{1_U} = r_{2_U} = r_{3_U} = r_u$, then

$$C_R = 2r_U \left(T_{1_U} + T_{2_U} + T_{3_U}\right) \tag{37}$$

or

$$r_U = \frac{C_R}{2\left(T_{1_U} + T_{2_U} + T_{3_U}\right)} \tag{38}$$

and using relation (28)

$$\left.\begin{aligned} r_{1_L} &= r_U \frac{T_{1U}}{T_{1L}} \\ r_{2_L} &= r_U \frac{T_{2U}}{T_{2L}} \\ r_{3_L} &= r_U \frac{T_{3U}}{T_{3L}} \end{aligned}\right\} \tag{39}$$

SUPPORT SYSTEM REQUIREMENTS

In the preceding section the general arrangement of a novel spring type suspension system is described in detail. However, considerable engineering is required to meet design objectives for a specific application. These requirements include the following:

(1) capability of adequately supporting the dead weight

(2) low effective mass

(3) low damping

(4) low stiffness

(5) adequate deflection capability to handle the range of model gross weights, steady air load reactions and dynamic response amplitudes

(6) sufficient range of adjustment on spring stiffness and cable tension to satisfy static and dynamic stability requirements for all loadings

Some flutter models are so fragile that they can fail under dead weight loads if inadequately supported. An important feature of the three point suspension system is that it can be adjusted to minimize fuselage vertical bending deflections and stresses due to dead weight loads. Effective mass can be held to a minimum by designing cables and sectors to low strength margins and by specifying minimum requirements for deflection, spring constant and tension ranges. Low damping is assured by the use of double ball bearings to support the sectors and by providing adequately large cable clearance holes in the tunnel. The low stiffness requirement tends to result in long torque bars. In our applications the torque bars were 18 to 20 feet long. The required range of adjustment of spring stiffness and cable tensions can be minimized by optimizing the suspension geometry for the specific application.

SUPPORT SYSTEM STABILITY AND CONTROL

Positive static or weather vane stability is essential to the maintenance of low trim loads and is assured as long as the support system elastic centers in pitch and yaw are forward of the corresponding aerodynamic centers. A finite pitching moment coefficient at zero lift can make the maintenance of low trim loads considerably more difficult. The pitching moment coefficient may be reduced by appropriate control surface or wing deflection if the local aerodynamic loads created by these deflections are not excessive and the effects on model stiffness are negligible. Where remote control of model incidence angle is provided, the suspension system can be effectively used to react the pitching moment.

The qualitative effect of center of gravity on rigid body longitudinal (or lateral) dynamic stability is shown in Figure 14. Regardless of the pitch to vertical translation frequency ratio, forward centers of gravity result in vibration modes with non-coalescent frequencies and hence are dynamically stable. Aft C.G.'s are shown to result in modal aerodynamic stiffnesses tending to promote frequency coalescence and dynamic instability.

Our experience with delta winged configurations has demonstrated that dynamic instability can be obtained for a forward C.G. with $\frac{\omega_P}{\omega_{VT}} > 1$ as a result of the small elastic camber deflections in the vertical translation mode that can occur even when the suspension frequencies are more than two octaves below the frequency of the fundamental elastic mode. This is illustrated in Figure 15 for a two point support system. The instability was due to the positive increment in aerodynamic stiffness in the vertical translation mode contributed by the elastic camber. It should be noted that camber deflections are shown greatly exaggerated in Figure 15 for clarity. For a single point support it is shown that the effect of camber in the vertical translation mode can cause divergence when $\frac{\omega_P}{\omega_{VT}} > 1$. For $\frac{\omega_P}{\omega_{VT}} > 1$, both problems can be avoided with a spring constant distribution in a three point suspension representing a suitable compromise between the single point and two point extremes. The lower part of Figure 15 indicates that an even better solution would be to adjust a three point suspension to obtain a ratio of ω_P to ω_{VT} slightly less than unity, particularly if this can be achieved in a specific application with an elastic camber deflection contributing positive aerodynamic stiffness.

INFLUENCE COEFFICIENTS MEASUREMENTS

The measurement of model flexibility influence coefficients is an extremely important aspect of flutter model testing. These data are used to check theoretical methods of stiffness calculation, to assess the accuracy of model stiffness against calculated or measured full scale data and to substantiate the accuracy of theoretical methods for computing vibration modes and flutter speeds through comparisons with measured values.

Unfortunately these measurements can be both tedious and time consuming. To minimize these difficulties and at the same time obtain highly detailed descriptions of model flexibility we have developed the use of automatic data gathering and analysis equipment. The heart of the data gathering system is a 40 channel Crescent Engineering model 540 Commutated Translator unit. Crescent variable permeance deflection transducers with a 2 inch stroke providing a maximum overall system resolution of ±0.0002 inches are connected to the inputs of 38 of the 40 channels. The remaining 2 channels receive the inputs from deflection transducers mounted in calibrated force rings to measure the applied loads. The force rings are mounted on counterbalanced arms which can be rapidly moved and locked in any position. Forces are then applied by turning coarse screws or fine differential screws installed between the force rings and the supporting arms. The electrical outputs of the force rings are calibrated in pounds and any force up to 50 pounds can be set by observing the output on a digital voltmeter in the Translator unit.

The deflection transducers consist of encased center-tapped coils with central probes. Each probe weighs approximately 5 grams and fits loosely in the coil assembly. Typical deflection transducer setups consist in mounting the coils directly below the model control points with their axes vertical and suspending the probes on strings from small hooks temporarily attached at the model control points. To measure lateral deflections or where space problems exist the strings are routed over pulleys. The Translator unit contains an automatic printer for data recording and an IBM unit has also been connected to the Translator output for automatic data recording on punched cards. The Translator unit contains a cross-bar scanner which automatically sweeps through the 40 channels in approximately 30 seconds. In this manner individual channel sensitivities, applied loads and deflections are automatically punched on IBM cards. These cards are then fed into a computer program which determines the best slope fit of the load-deflection data and tabulates these slopes as an assembled influence coefficients matrix. Figure 16 shows typical setups for influence coefficients measurements. With this equipment the data for a 30th order matrix have been recorded in less than two hours and 60th order matrices are commonly obtained.

VIBRATION MEASUREMENTS

The measurement of natural vibration modes is also a very important part of flutter model testing. Our first natural modes measurements on a flutter model are usually made in the Dynamics Laboratory for the boundary conditions set up for the influence coefficients measurements. The measured mode shapes and frequencies are compared with calculated values based on the measured influence coefficients to obtain a check on the accuracy of the measured influence coefficients and the calculated mass data. If the support conditions in the wind tunnel are different, the appropriate analytical transformations of the measured influence coefficients are made and the checks of calculated versus measured modes are repeated. Figure 17 shows a typical multi-shaker vibration test setup in the wind tunnel. Good agreement is usually obtained between measured and calculated data for the first four or five modes. Due to difficulties in accurately measuring higher modes on lightweight models, more reliance is usually placed on the calculated higher modes and the calculated modes are used in the flutter analyses to correlate theory with experiment. In complete air vehicle flutter analyses we have found that modes as high as the ninth free-free mode can significantly affect the flutter speed. This was due, in this case, to an overlap in the frequency spectrums of predominantly chordwise fuselage modes and predominantly spanwise wing modes.

FLUTTER TEST INSTRUMENTATION

Flutter model wind tunnel instrumentation should be designed for maximum simplicity and reliability as well as for minimum weight and cost while providing the following information and functions:

(1) Instantaneous (pen) recordings of model response waveforms

(2) Oscillograph recordings of model frequency and phase response accurately related to tunnel test conditions.

(3) Oscillograph recordings of model trim and dynamic stresses. For tests in continuous tunnels these data should also be displayed on meters.

(4) Automatic triggering of high speed motion picture cameras and model safety devices for tests in continuous tunnels.

In our experience, strain gage sensors have proved to be the best choice for satisfying the above requirements. They are reliable, light in weight and low in cost. Used in a carrier system, their ability to sense frequency, phase and stress and the possibility of feeding more than one circuit with the output of a single bridge tends to promote overall simplicity.

On a model of a complete air vehicle, six or more strategically located temperature compensated strain gage bridges may be required. For the suspension system previously described, normal force is measured by installing a complete bridge on each of the torque bar springs, adjusting the outputs to be proportional to the individual spring constants and interconnecting the outputs to be additive for pure translation. An additional set of six bridges is installed to measure the suspension system pitching moment reaction. A total output proportional to pitching moment can be obtained by adjusting the individual outputs to be proportional to the product of spring constant and distance from the elastic center and summing the outputs with proper regard to signs.

SAFETY DEVICES

A quick acting tunnel q reduction or shutdown device is required if one is to plan with some confidence to obtain more than one flutter point from a single model.

Figure 18 illustrates one of the earlier devices we have used for this purpose in our low speed tunnel. In the retracted position each screen is held flat on the tunnel floor by a solenoid operated latch. The latch is actuated by an electrical signal which also simultaneously de-energizes the tunnel fan motor. The actuating signal can be applied either with a manual switch or automatically from model strain gage signals through an electronic triggering device set to operate at predetermined stress levels. When released by the solenoid operated latch, preloaded springs initiate the upward rotation but the airstream supplies most of the force for extension. As the speed brake approaches the 90 degree travel limit, hydraulic shock struts provide a smooth deceleration to zero velocity. Full extension took place in approximately 0.25 seconds. An initial q reduction of 40% was obtained over the area blanketed by the screens and the tunnel velocity decreased to zero after approximately 10 seconds. The screens were positioned in the tunnel to blanket the flow over the wings of complete air vehicle models. This safety device was first used with the model shown in Figure 6. The initial tests were conducted in 1954 and approximately 1000 runs including 400 flutter points have been obtained in external stores flutter investigations on this model. This model is still intact largely due to the effectiveness of this "fly swatter" speed brake device.

Figure 19 illustrates a later speed brake device. It consists of a false floor and ceiling with trailing edge tabs and can be quickly installed in the test section. Like the earlier device it is coupled to the fan motor and can be triggered either manually from several test crew stations or automatically at predetermined model stress levels. Electric motors release the tab latches and drive cams to initiate tab rotation. The airstream provides most of the energy for tab rotation. Rotation through the total travel of 100 degrees occurs in less than 0.1 seconds. Figure 20 shows a time history of the reduction in test section dynamic pressure. The additional blockage of the main stream and the aspirator effect on the secondary streams due to tab deflection tend to divert the main stream flow to the secondary streams. In addition to fast response, this system provides full effectiveness throughout the test section and thus can be used with any type of model installation.

TUNNEL FLOW ROUGHNESS

While some tunnel flow roughness or turbulence is desirable for the purpose of exciting flutter, it can create serious problems in the testing of flutter models with low mass ratios and wing loadings. One problem is that the apparent flutter speeds obtained may be somewhat lower than the true flutter speeds. As the flutter speed is approached the response to turbulence in the flutter mode increases as the aerodynamic damping decreases with the result that the true flutter speed may not be quite attained due to (1), misinterpretation of the more-or-less sustained forced vibration response as a sustained flutter oscillation and (2), the desire to avoid overstressing the model. Another possible problem is that for even lighter and more fragile models the stresses induced by flow turbulence may be excessive for speeds well below the flutter speed.

Over the years, no flow roughness problems were encountered in tests of relatively high mass ratio models in our 8x11 foot low speed tunnel. However, fairly recent attempts to test low mass ratio complete air vehicle flutter models indicated that the turbulence level would have to be reduced if these tests were to be successfully completed.

Measurements in the test section indicated small fluctuations in both dynamic pressure and flow direction. The fluctuations in flow direction were considered to be primarily responsible for excessive model dynamic stresses and rigid body displacements--particularly when the tests were conducted at zero lift.

The first major attempt at improving the flow smoothness was to install a screen with about 50% porosity. This was installed across the stilling chamber just upstream of the contraction to minimize power consumption. Subsequent flow measurements indicated only slight improvements. After much additional thought and small scale experimentation the final solution was proposed. This consisted of installing honeycomb across the big section just upstream of the screen. The honeycomb had a six inch square cell size and was three feet long in the streamwise direction. The improvement was dramatic. Fluctuations in flow direction were reduced to between 1/5 and 1/10 of the previous level. And more important, in tests of low mass ratio flutter models, the onset of flutter could be detected on a pen recorder as a relatively clean sinusoidal response often before any motion could be detected by visual observation of the model.

Later on when the same problem arose in attempts to test a complete air vehicle model at transonic speeds in our 7x7 foot Trisonic blow down tunnel, we knew what was required. After honeycomb was installed in the stilling chamber, the test section turbulence was reduced by about the same factor as for the low speed tunnel and the transonic complete air vehicle model tests were successfully completed.

FLUTTER TESTING

The objectives of flutter testing, at least in continuous flow tunnels and particularly for low speed models, are somewhat analogous to repeatedly walking to the edge of an abyss and safely retreating. It is desired to obtain the critical flutter speeds, flutter frequencies and mode shape information for each of many configurations using only one model. This is a big order, and its completion requires a great deal of knowledge and careful planning in all phases of the work leading up to and including the actual testing.

In addition to the preceding portions of the paper, a few specific comments may be in order. To avoid the possibility of explosive flutter, coulomb friction in models and their suspension systems should be held to an absolute minimum, and all testing should be conducted well within the known model strength. An instantaneous recorder such as a pen type is extremely helpful in that the up-to-date time histories of flutter bursts obtained make possible rapid judgments as to the magnitude of damping and when the point of sustained flutter has been reached.

A typical pen recording of a flutter point obtained on a low speed model is shown in Figure 21. Due to the low tunnel flow turbulence, the flutter response is extremely clean even though the motion is so small as to be barely perceptible in direct viewing of the model. The rapid decay of the flutter oscillations following the actuation of the "q reducer" also may be noted.

CONCLUDING REMARKS

It is clear that flutter model techniques have become increasingly important as the flutter problem has assumed greater importance in the design of high performance aircraft. In the future we can expect further developments in dynamic modeling technology as new problems are posed by more advanced flight vehicles.

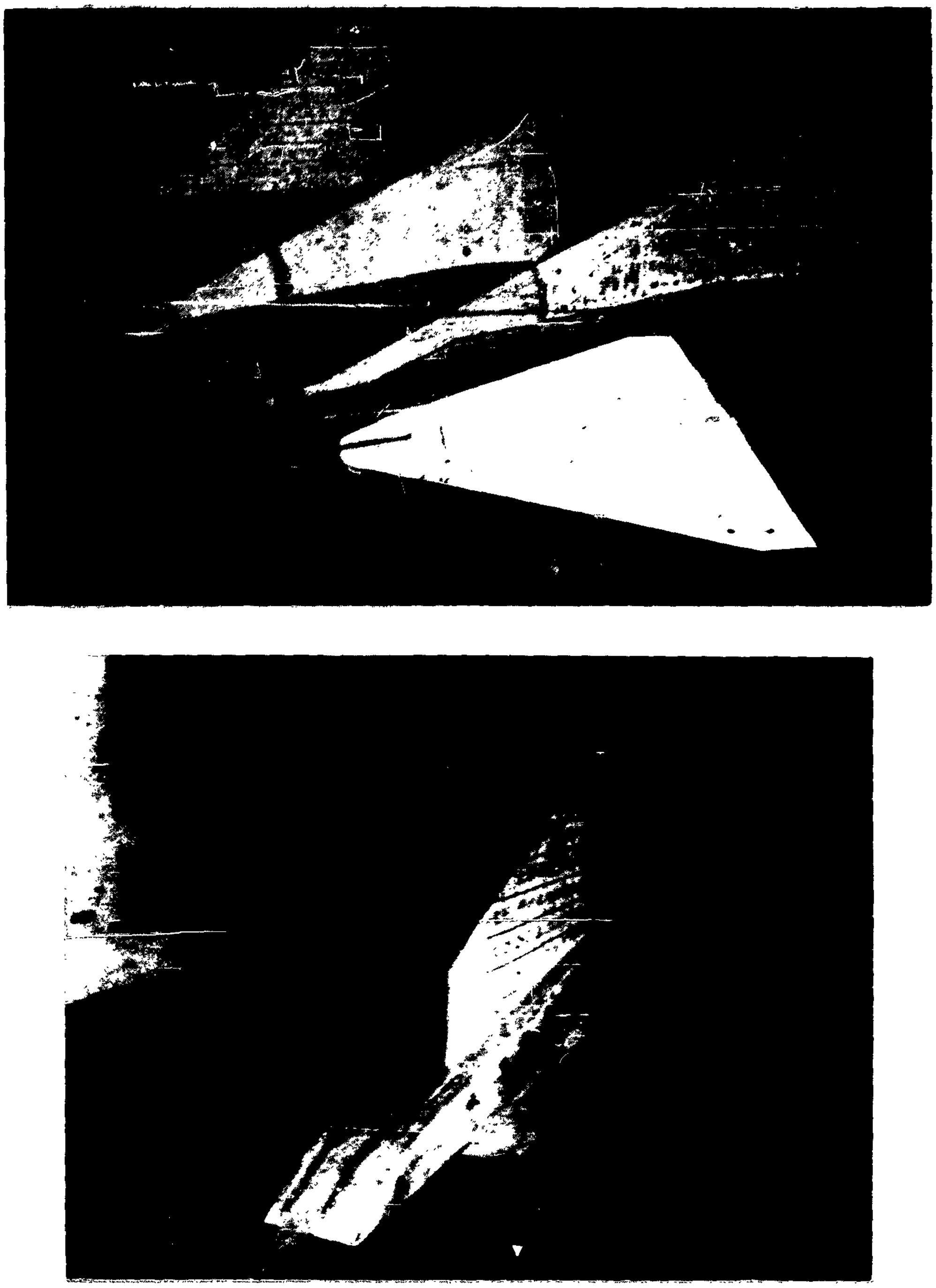

Figure 1 Low speed solid styrofoam flutter models

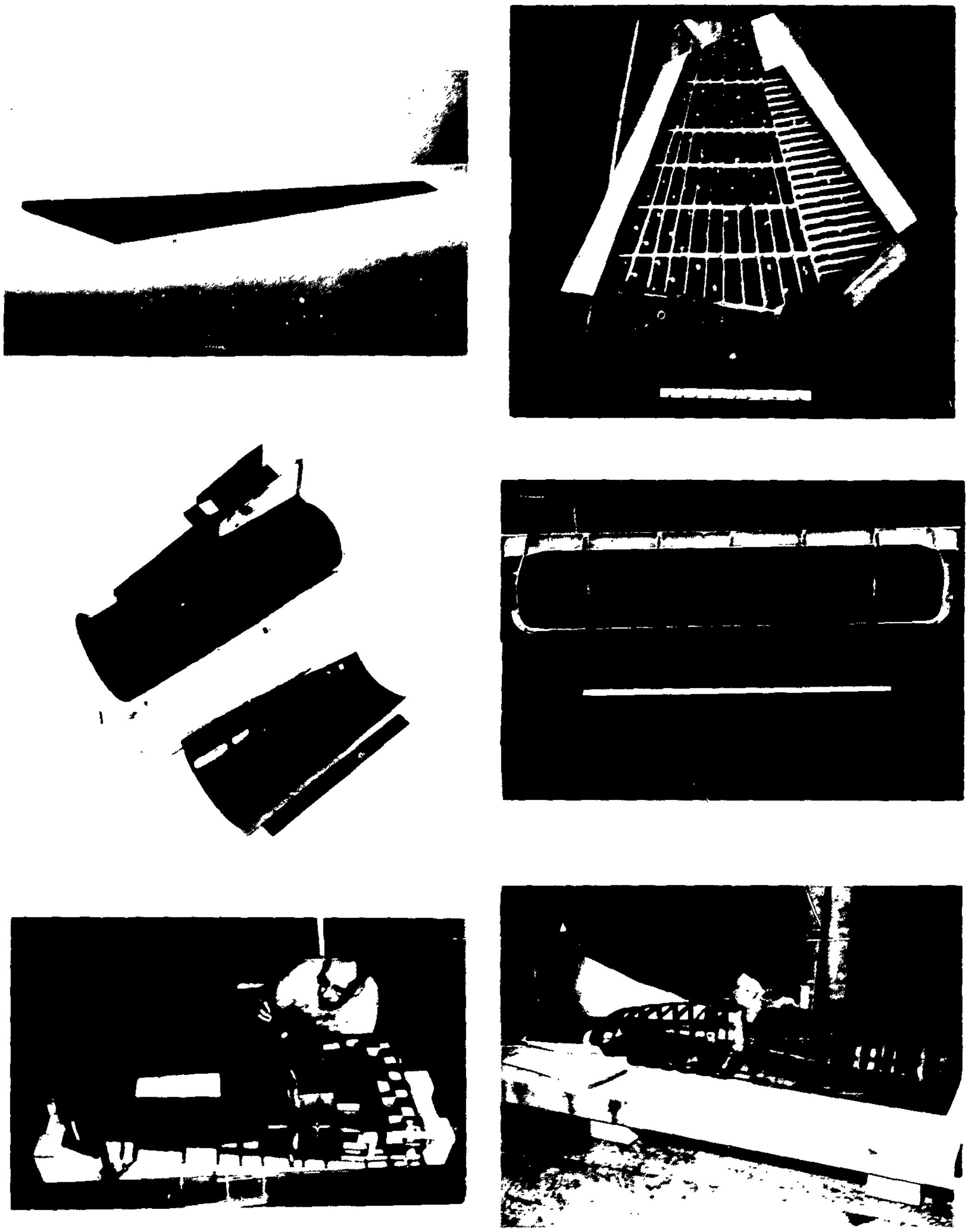

Figure 2 Construction details, low speed directly scaled flutter models

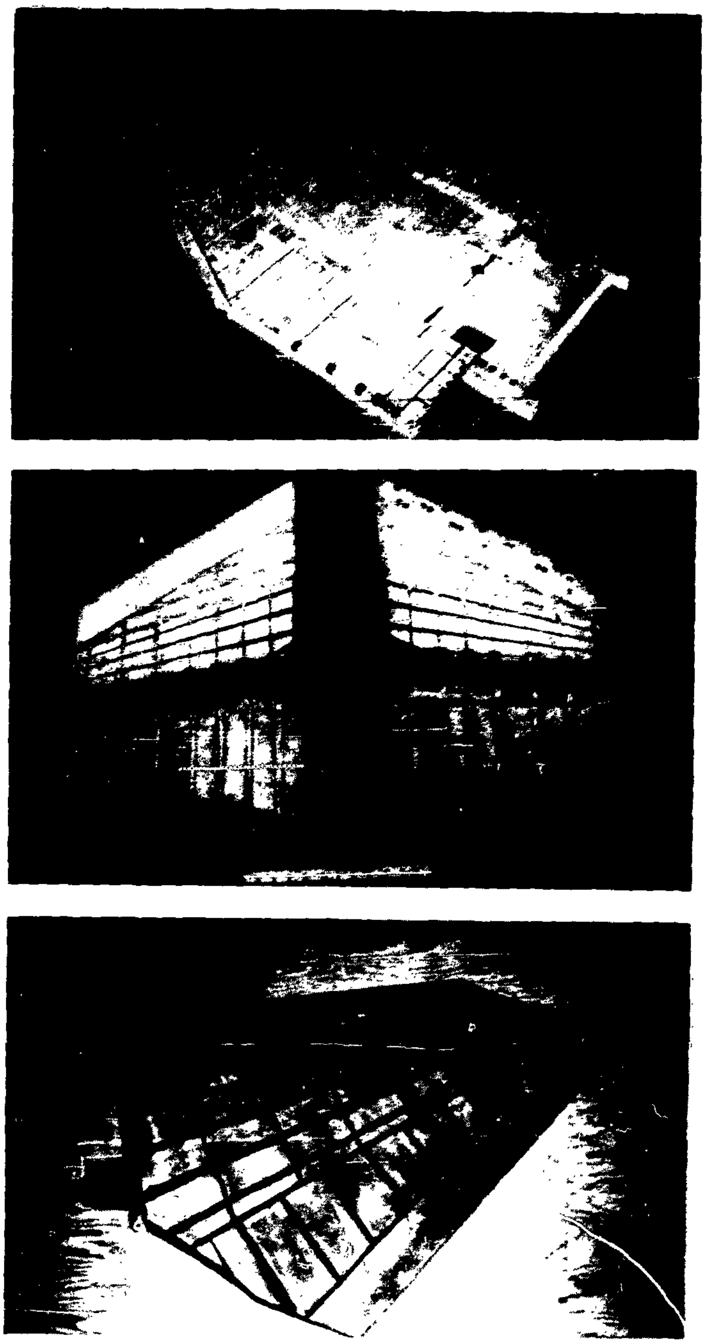

Figure 3 Construction details, high speed directly scaled flutter models

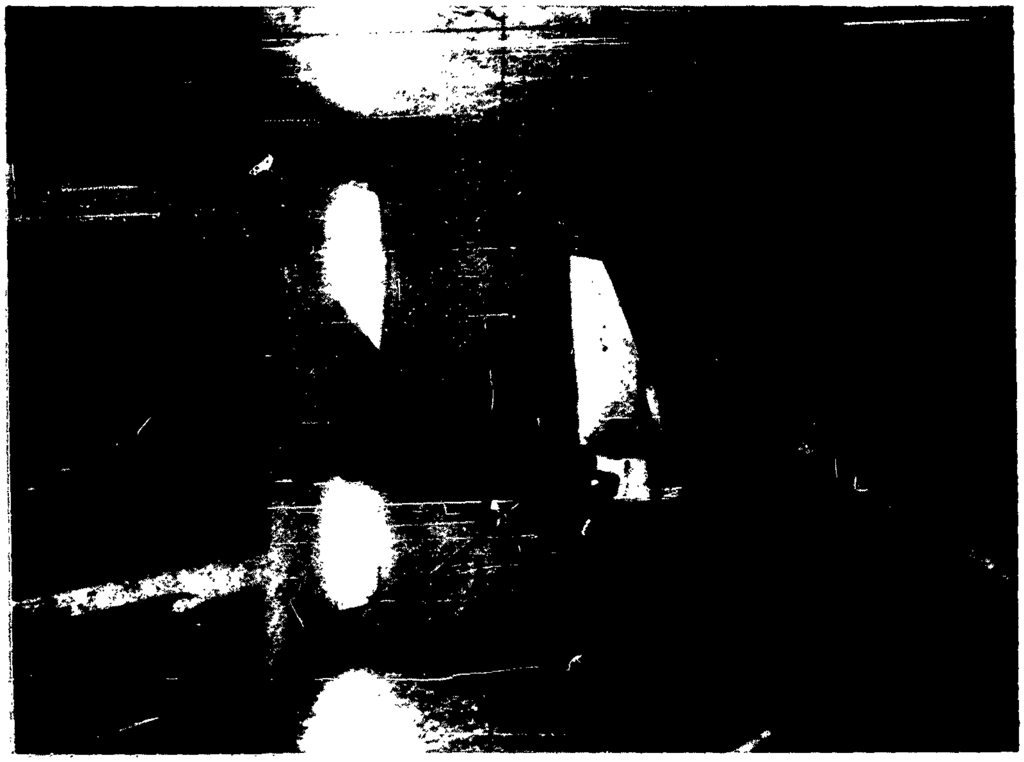

Figure 4 Low speed directly scaled flutter model

Figure 5 High speed directly scaled flutter models

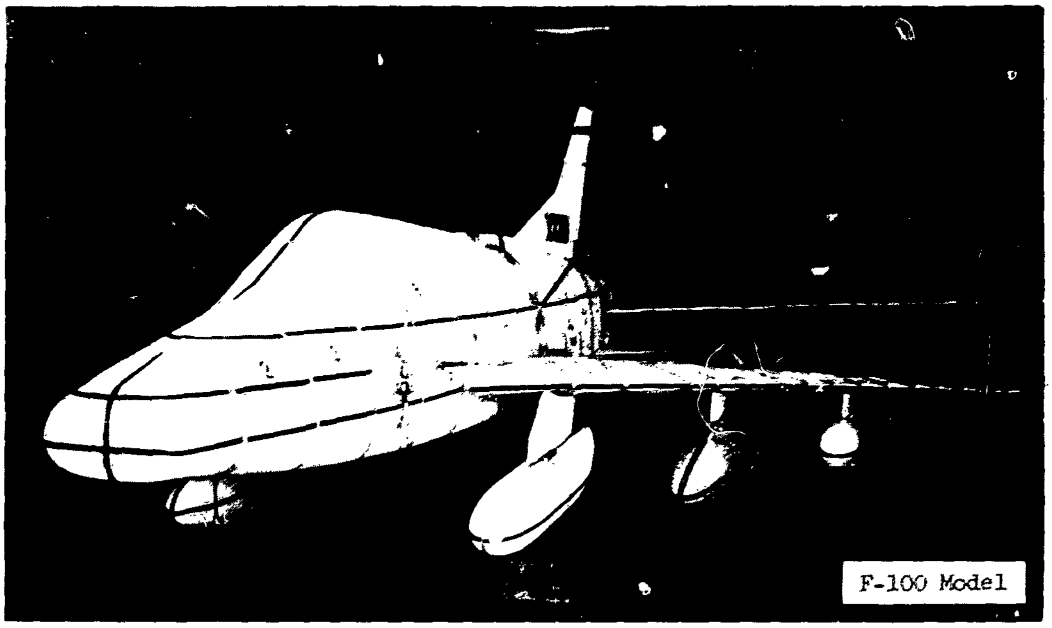

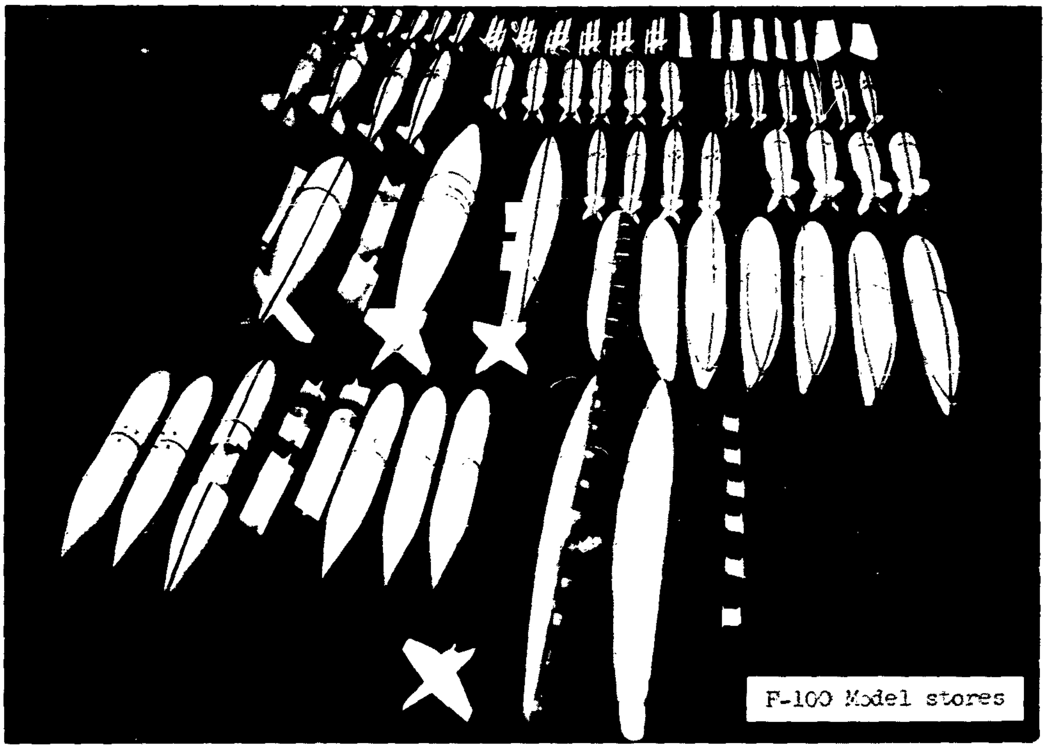

Figure 6 Low speed indirectly scaled flutter model

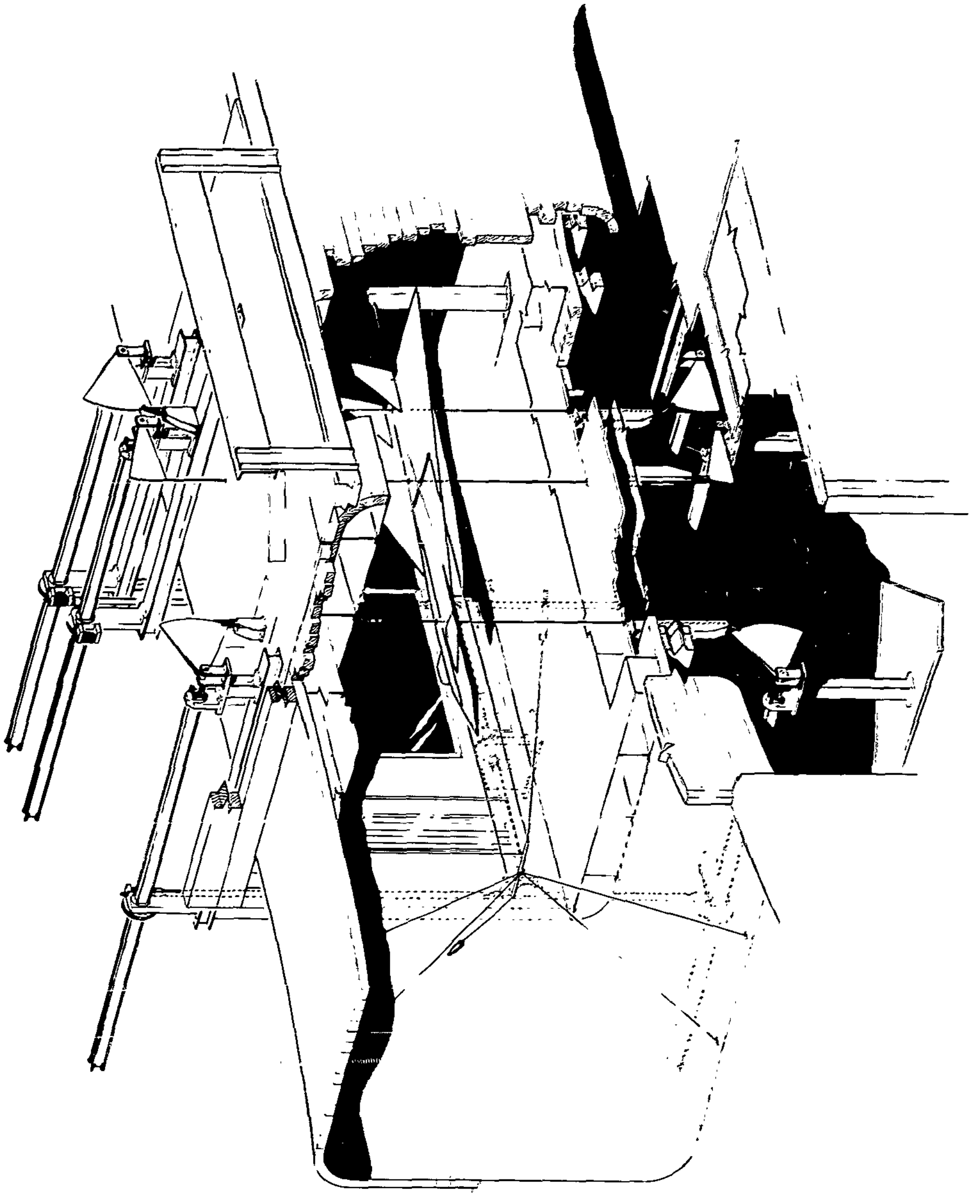

Figure 7 General arrangement, flutter model suspension system

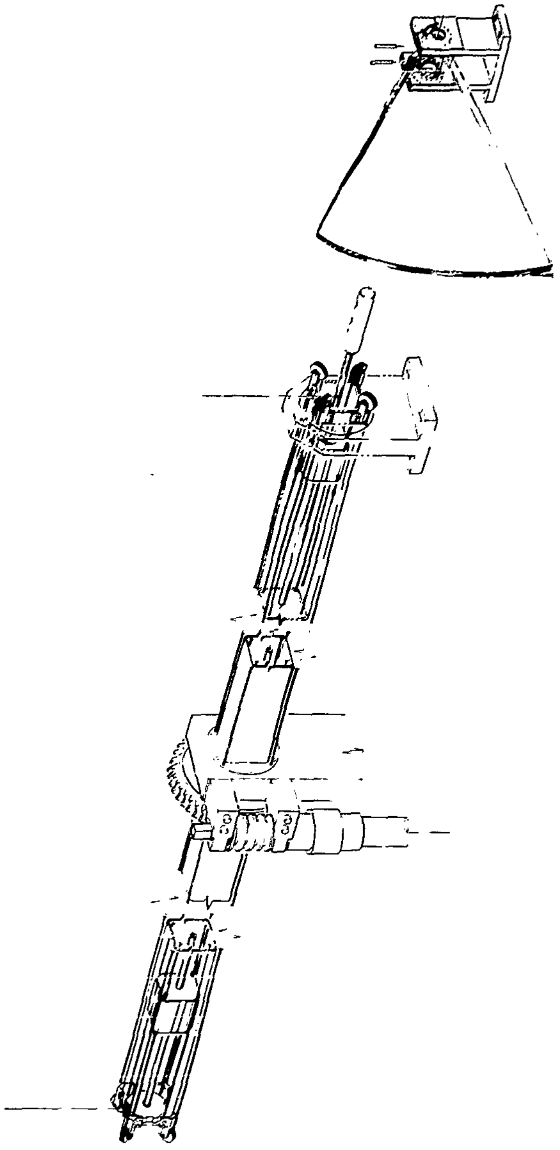

Figure 8 Typical torque bar assembly, flutter model suspension system

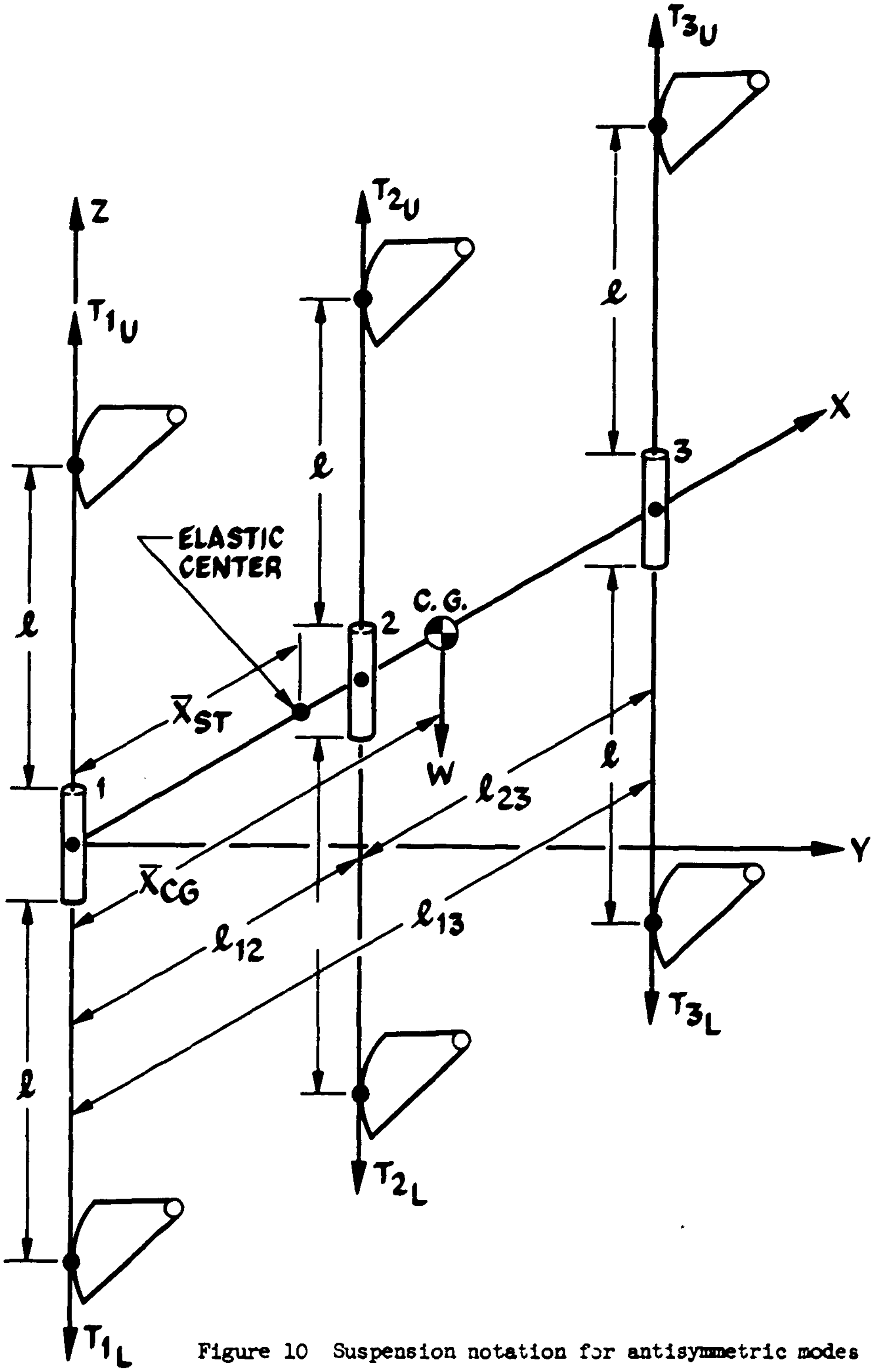

Figure 10 Suspension notation for antisymmetric modes

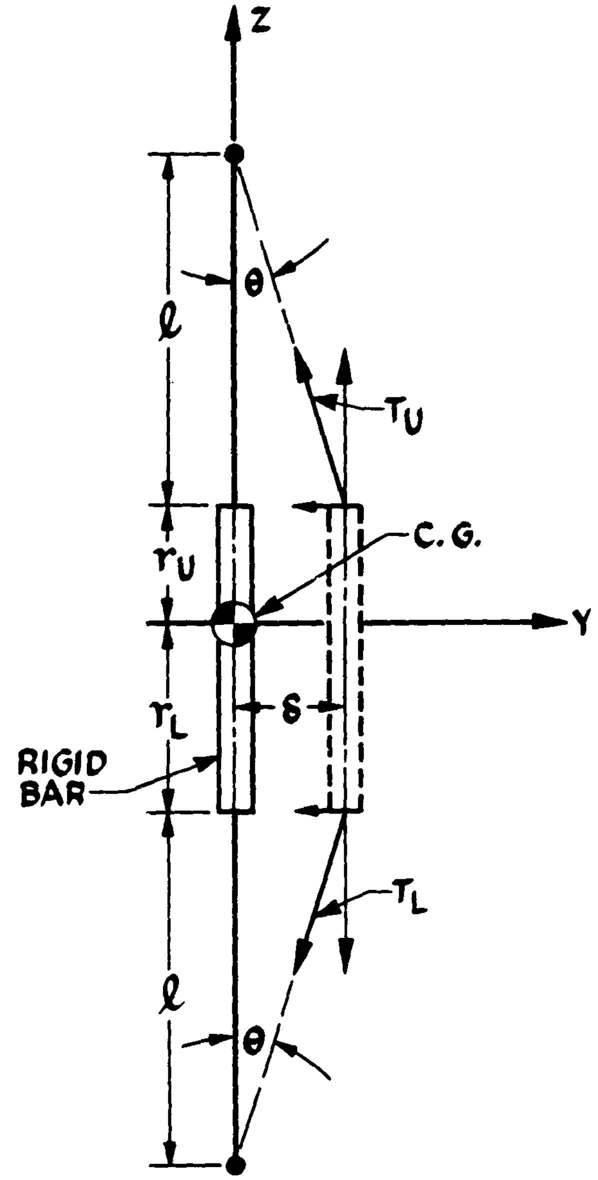

Figure 11 Support point lateral displacement

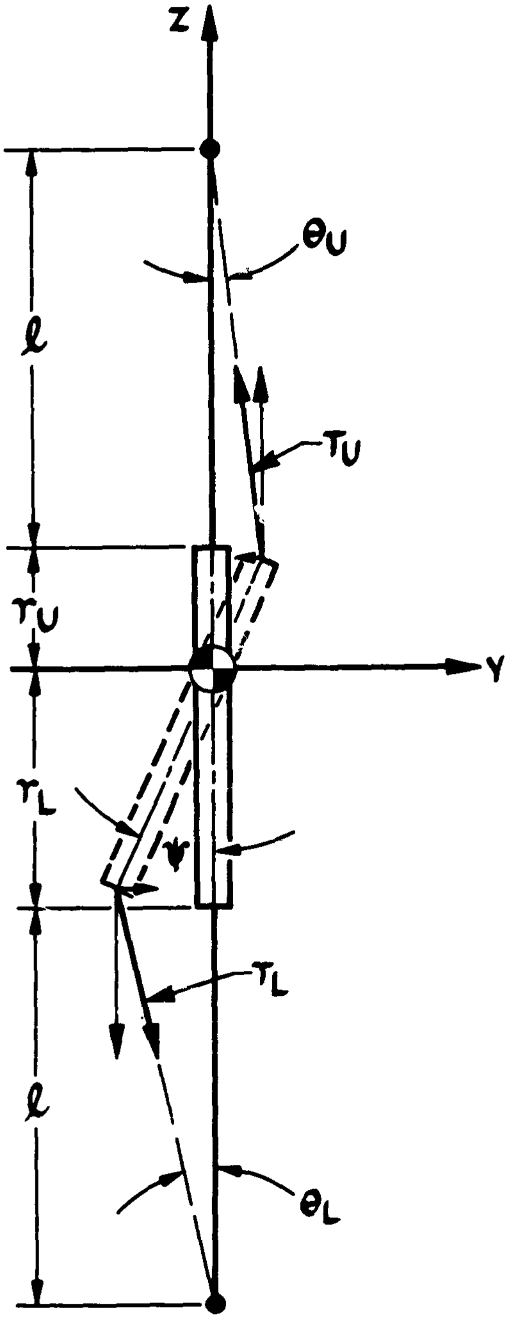

Figure 12 Support point roll displacement

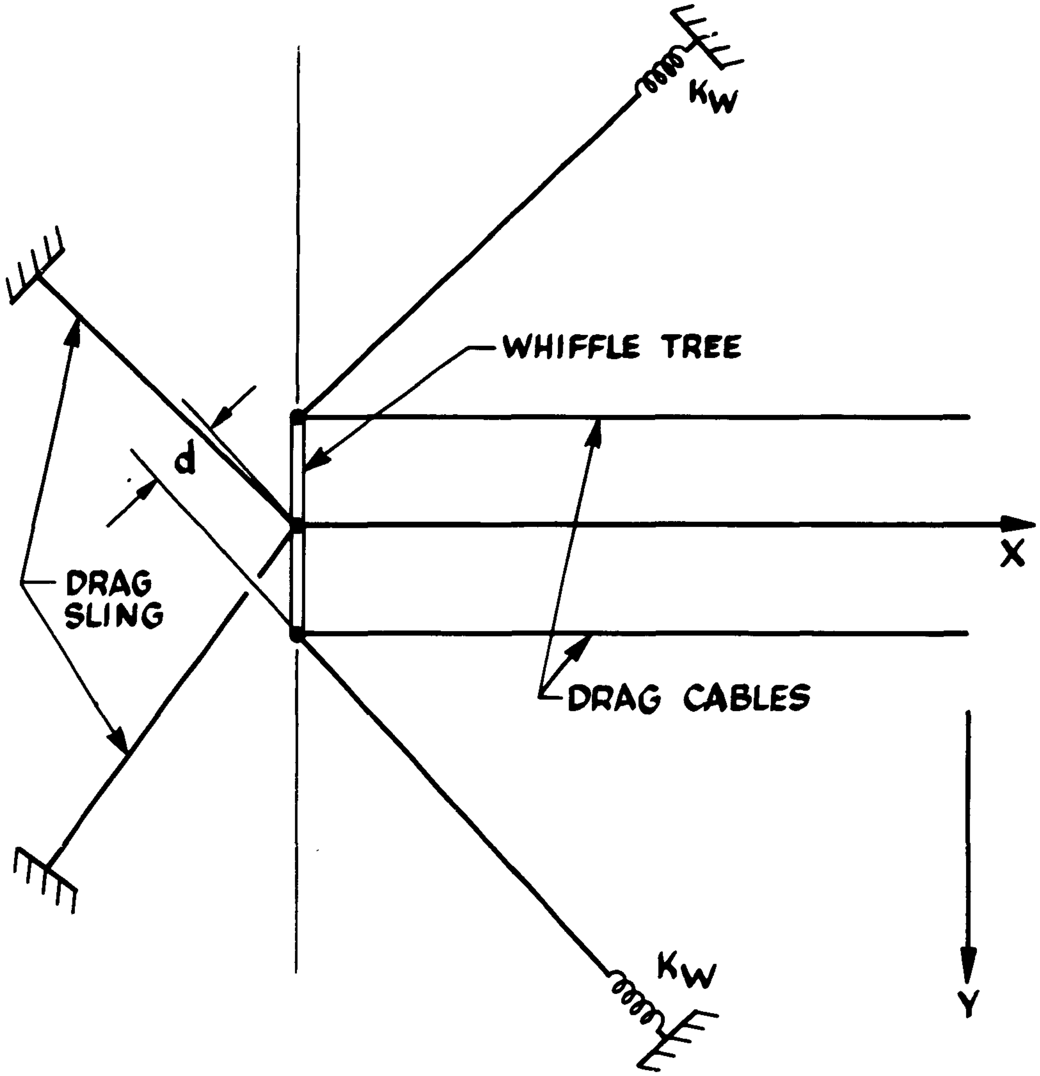

Figure 13 Suspension drag harness

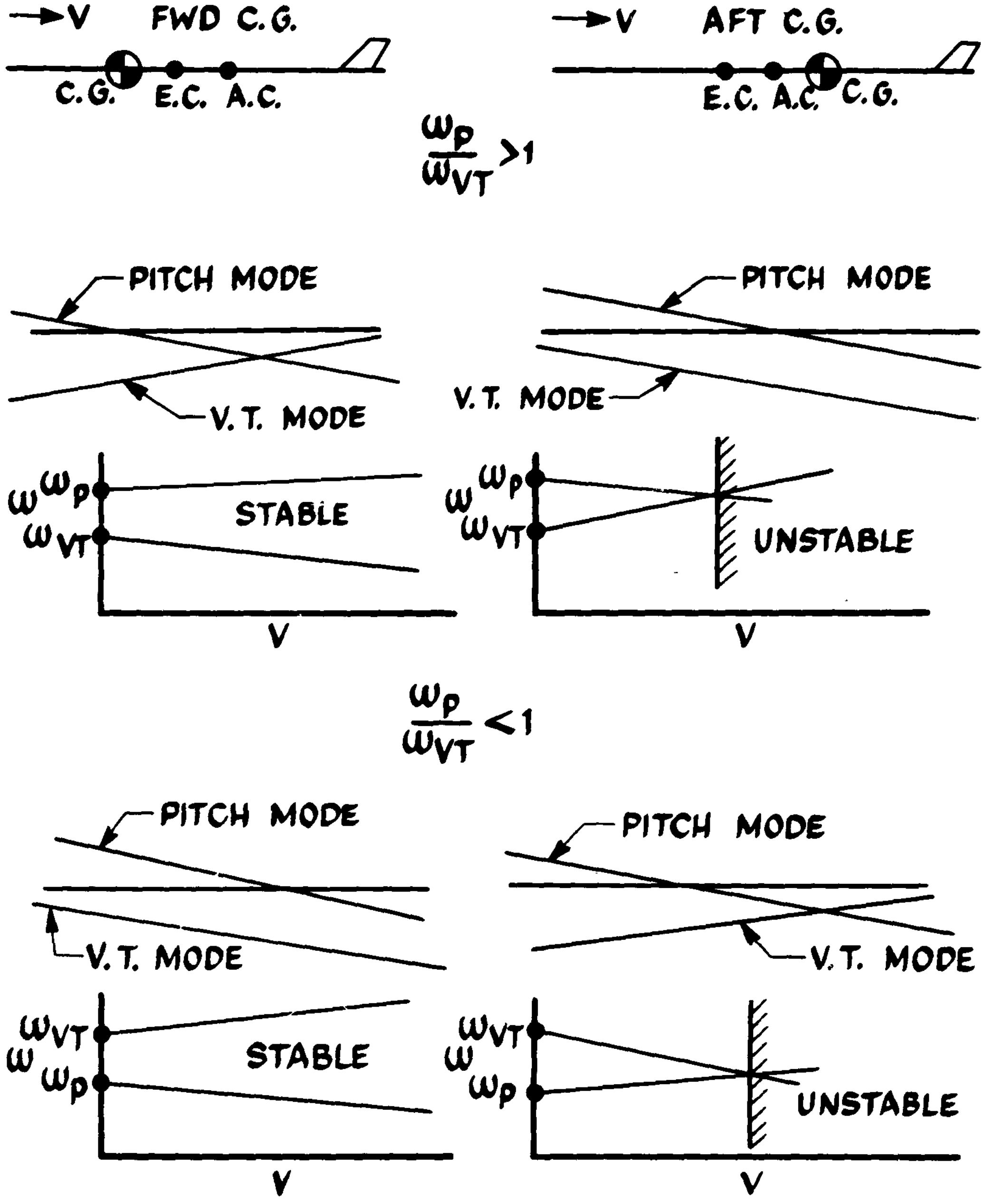

Figure 14 Effect of C.G. location on suspension dynamic stability

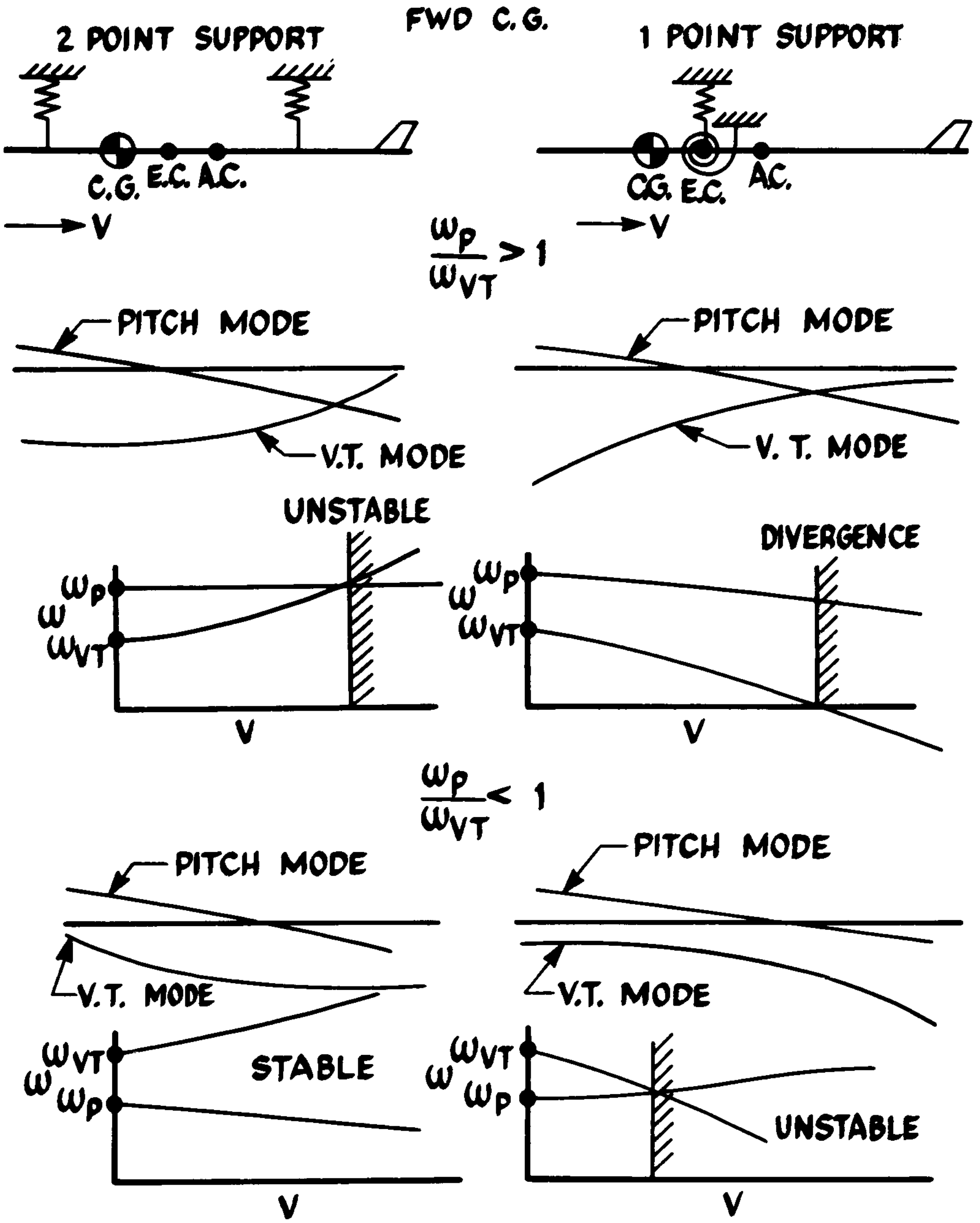

Figure 15 Effects of model elastic camber deflections on suspension stability

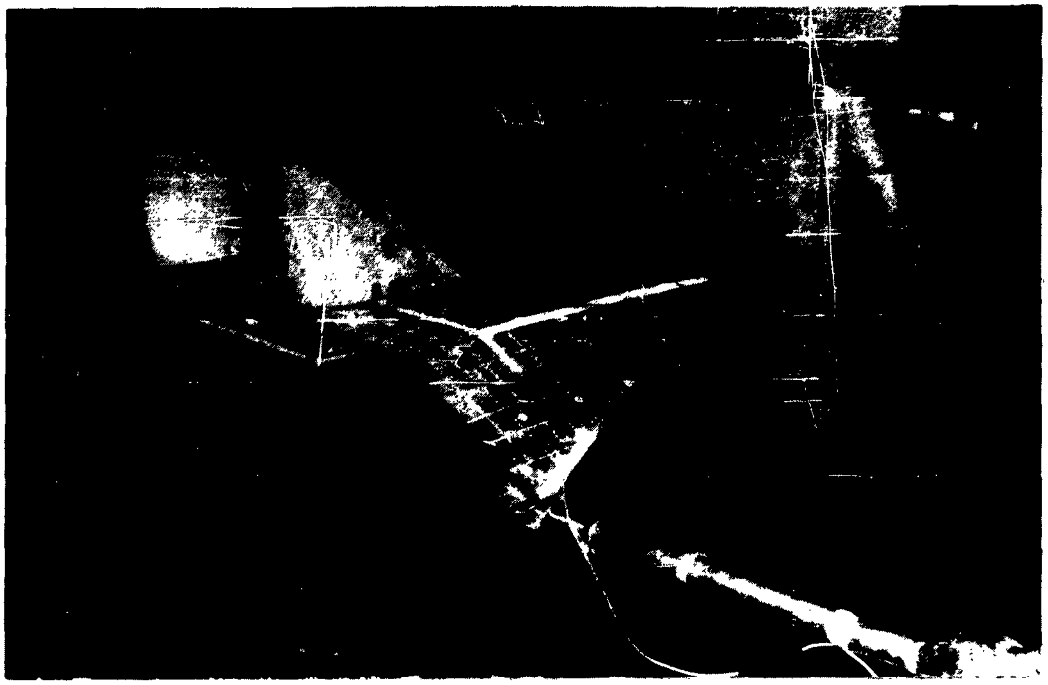

High speed flutter model

Low speed flutter model

Figure 16 Influence coefficients measurements

Multi-shaker setup

Electronics equipment

Figure 17 Model shake test in wind tunnel

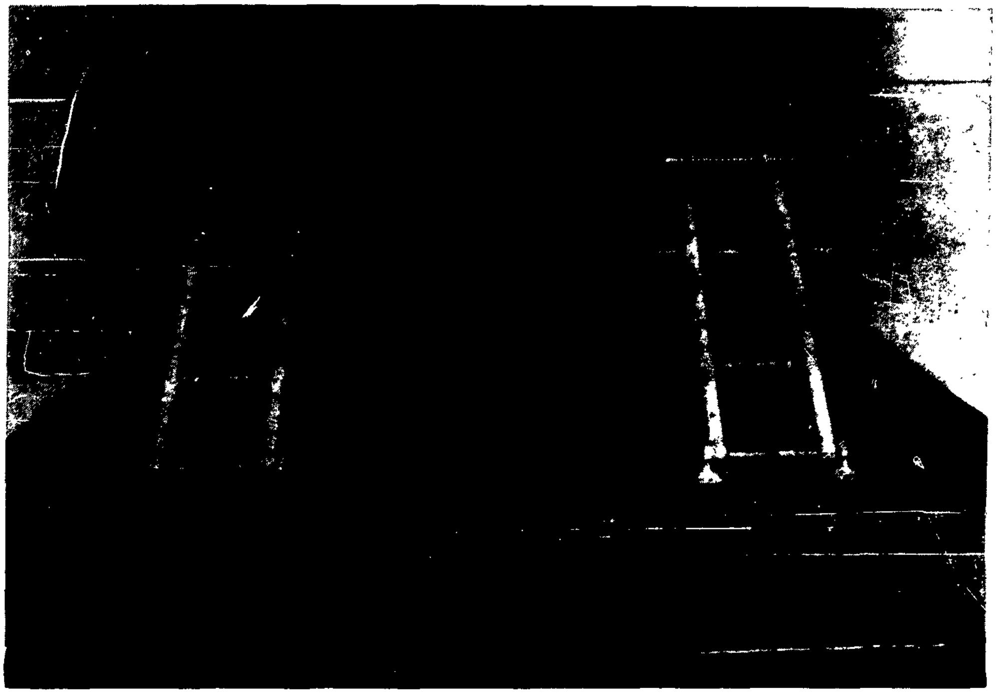

Figure 18 An early wind tunnel speed reduction device

Tabs retracted

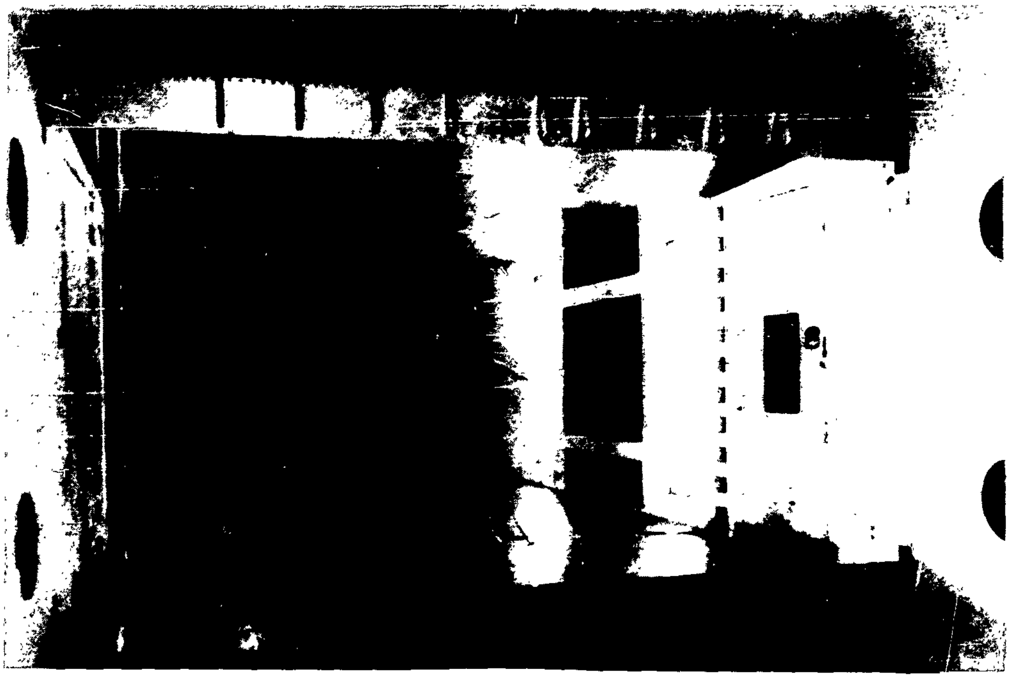

Tabs extended

Figure 19 Wind tunnel "q reducer" safety device

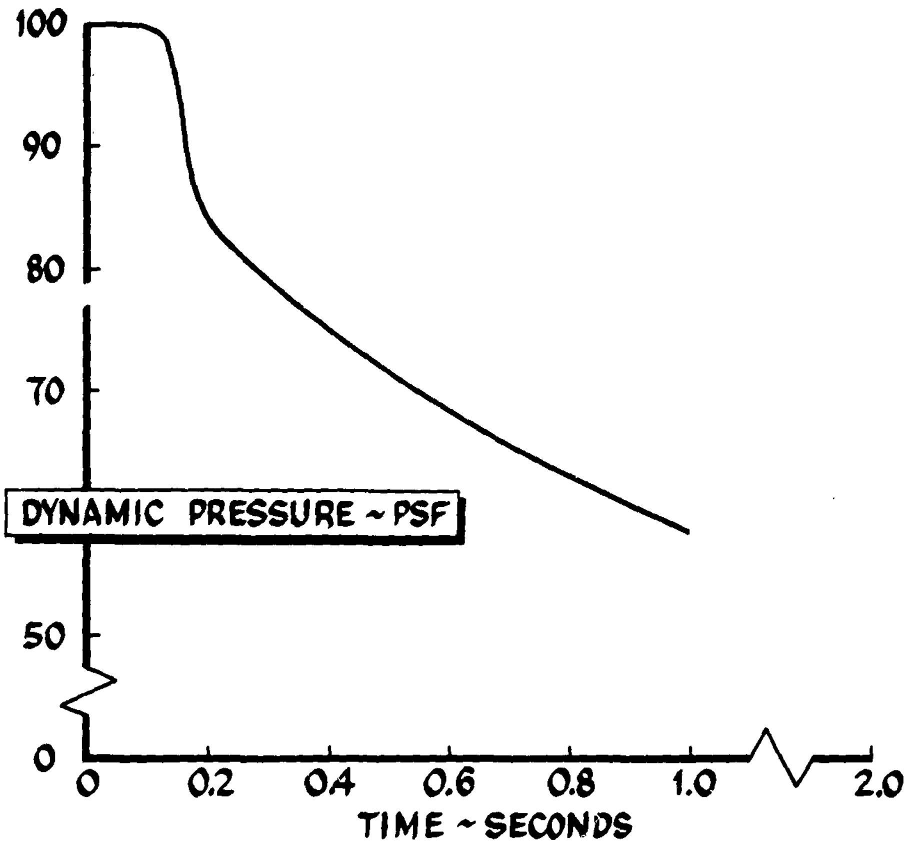

Figure 20 "q reducer" performance

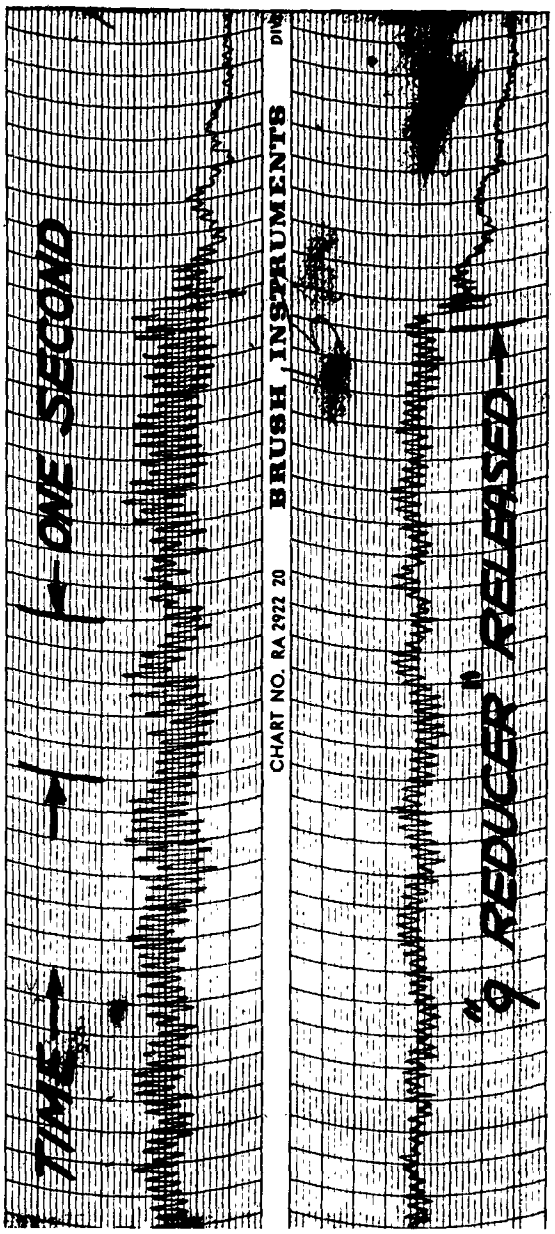

Figure 21 A typical low speed flutter record

THE USE OF DYNAMICALLY SIMILAR MODELS FOR THE DETERMINATION OF TRANSIENT LOADS ON THE LASV

B. J. Brock, Engineering Specialist

B. G. Musson, Engineer

Structures Dynamics Group

CHANCE VOUGHT CORP.
A SUBSIDIARY OF LING-TEMCO-VOUGHT, INC.

ABSTRACT

This paper discusses the design, construction, and testing of a dynamically similar model used for measuring transient loads in a high speed wind tunnel. The model tested during this program was a model of a nuclear ramjet powered, low altitude supersonic vehicle (LASV). This vehicle is a high fineness ratio lifting body with three equally-spaced stabilizers and a canard elevator system. Dynamic loads at two stations on the fuselage obtained for store ejection and transient elevator inputs are compared with analytical results.

LIST OF ILLUSTRATIONS

LIST OF TABLES

THE USE OF DYNAMICALLY SIMILAR MODELS FOR THE DETERMINATION OF TRANSIENT LOADS ON THE LASV

B. J. Brock, Engineering Specialist

B. G. Musson, Engineer

Structures Dynamics Group

CHANCE VOUGHT CORP.
A SUBSIDIARY OF LING-TEMCO-VOUGHT, INC.

I. INTRODUCTION

The content of this paper presents data obtained under contracts AF33(657)-8686 and AF33(657)-10439 with the United States Air Force. As a partial fulfillment of these contracts, a model was constructed and tested to provide empirical data for comparison with analytical studies. The objectives of the test program were:

(1) Assure that the stabilizers are free of flutter within the operational limits of the vehicle.

(2) Measure transient loads on the fuselage resulting from the ejection of an internal store.

(3) Measure transient loads on the fuselage resulting from elevator inputs.

II. MODEL DESIGN AND CONSTRUCTION

Prior to the finalization of the model design, several studies of the model were required. The size of the model and the values of various nondimensional parameters had to be established and analyses done to assure the suitability of the values chosen. It was decided the model would be built without the inlet and duct because they have negligible effect on the symmetric dynamical characteristics of the vehicle.

The capabilities of the vehicle at design conditions imposed severe requirements for dynamic simulation with a model. Because of its size and dynamic pressure capabilities, the CVC High Speed Wind Tunnel was chosen for this series of tests. This tunnel has a 4' x 4' test section and a dynamic pressure capability at Mach 3.0 of about 4,800 psf. The large test section permitted the use of a 1/20 scale model at Mach numbers up to 1.6 without interference from the shock wave reflected from the tunnel wall. Also, the high dynamic pressure capability allowed the use of a reasonable stiffness ratio.

The model geometric scale factor is defined by:

$$n = \frac{l_m}{l_a} = 0.05 \qquad (1)$$

Where:

n is the geometric scale factor
l_m is a representative model length
l_a is the corresponding representative vehicle length

As mentioned above, this value is set by the tunnel size and lowest Mach number desired for testing.

The stiffness ratio of the model is determined by the dynamic pressure capabilities of the wind tunnel used for testing. The dynamic pressure for the vehicle at Mach 3.0 at sea level, standard NACA conditions is 13,346 psf, and the tunnel is capable of approximately 4,800 psf. The ratio of these two dynamic pressures determines the stiffness ratio. It was decided to test at a design dynamic pressure of 4,000 psf, thus:

$$f = \frac{q_m}{q_a} = 0.30 \qquad (2)$$

Where:

f is the stiffness ratio
q_m is the dynamic pressure for the model
q_a is the dynamic pressure for the vehicle

The mass ratio of the model is determined by the air density capabilities of the wind tunnel. In this case the tunnel is capable of approximately sea level density, therefore:

$$m = \frac{\rho_m}{\rho_a} = 1.0 \qquad (3)$$

Where:

m is the mass ratio
ρ_m is a representative model density
ρ_a is the corresponding vehicle density

The model frequency scales according to the inverse of the geometrical scale factor is such that the frequency ratio is given by:

$$r = \frac{n\omega_m}{\omega a} \tag{4}$$

Where:

r is the frequency ratio
ω_m is a representative model frequency
ω_a is the corresponding vehicle frequency

The frequency ratio is related to the stiffness and mass ratios of equations (2) and (3) respectively such that:

$$r = \sqrt{\frac{f}{m}} = 0.548$$

A store ejection mechanism was designed to simulate in model scale the transient loads on the vehicle resulting from the ejection of an internal store. This was accomplished with a pneumatic device that imparts a scaled impulse to a brass slug of scaled mass.

The design conditions of the ejection mechanism were to eject the mass with an impulse of 0.1148 lb_f-sec. The force-time history of the ejection was assumed to be approximately as shown in the non-dimensional sketch below.

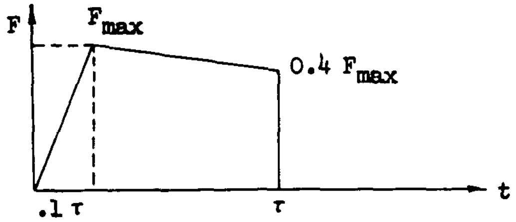

The stroke length and maximum force (F_{max}) determined from this curve when 0.0027 sec. are 0.9 sec. and 57.40 lb_f, respectively.

The model elevators were designed to introduce transient inputs into the system. This was accomplished with a slow ramp up to 5^o deflection of the elevator with a "quick snap" back to zero. The mass, geometry, and root stiffness of the elevators were scaled, but surface flexibility was not.

Studies were made of the wind tunnel mounting system to investigate the effect of the mounting spring stiffnesses on the elastic modes and frequencies of the models. The coupled system was then investigated to insure that the system would be stable as installed in the wind tunnel. The "free-free" frequencies and the coupled frequencies of the system as installed on the sting are shown in Table 1. The elastic mode shapes were found to differ only a negligible degree from the free-free to the constrained condition.

The final design and construction of the models were subcontracted to Dynamic Devices, Incorporated of Dayton, Ohio. The primary structure of the model is made of aluminum. This has an advantage in that the ratio of the Young's modulus of aluminum to that of steel, which is the material of the vehicle, is almost the same as the stiffness ratio. This allows many pieces to be built by merely scaling the vehicle dimensions down to model size.

In general, the philosophy of design was to have a basic structure of proper stiffness with a light-weight, non-load-carrying aerodynamic fairing. It is known that the starting loads in the tunnel can be as high as 16 psi across the model at $M = 3.0$ with 7 or 8 psi being normal at this Mach number. These loads were taken into consideration during the model design, but it was not possible to design to 16 psi and still maintain the scaled stiffness required. In these cases, the stiffness design was used in the hope the resilience of the model mounting would alleviate the starting loads sufficiently to keep from damaging the model.

A general arrangement layout of the fuselage model is shown in Figure 1. The structural tube was attached to the sting by means of leaf springs designed to allow pitch and translational degrees of freedom but to constrain the model in yaw. The forward mounting was designed to give a pinned effect at the model attachment point and cantilevered at the sting. The rear support springs are clamped at both ends, both at the model and at the sting. The spring attachment points were located as near to the node points of the first elastic mode as possible so that the springs would have a small effect on this mode. Circular steel rings were used as stabilizer mounting reinforcing rings. Brass rings were attached to the structural tube to give the model the correct mass distribution. The basic structural tube and attached weights were inclosed with a balsa shell covered with silk to give the model the correct aerodynamic contouring. The complete model and a cut-away view are shown in Figure 2.

The ejection mechanism is a pneumatically-operated piston-cylinder arrangement. The slug (which is the piston in this case) is held in place by a brass screw machined to the proper diameter to break at 57 pounds load. The calculations indicate that this breaking load should give an impulse of about 0.11 lb_f-sec. Air pressure supplied to the cylinder provided the force required to break this screw. The ejection mechanism was positioned on the antinode of the first elastic mode to insure the maximum response in this mode. The location of the ejection mechanism is shown on the general arrangement drawing of Figure 1.

Movable elevators made of solid aluminum were placed on the model so that transient inputs could be induced upon the model during the tunnel runs. The elevators were driven by an electric motor through a cam arrangement which lifted the elevators to an angle of 5° and allowed them to snap back to zero through a half cycle of the cam. The elevators were returned to the zero position with a spring arrangement. The electric motor was mounted at the fuselage bulkhead at the cone-cylinder break (this is also the point of attachment of the forward support springs). The location of the elevators and the actuator motor is shown on Figure 1.

The initial model stabilizer construction was basically the same as the vehicle stabilizer structure used as the basis of the mathematical model. A planform drawing of the stabilizer model is shown in Figure 3. The stabilizer structure was later modified to the planform shown in Figure 4 to give the model added strength. The initial stabilizer model was made up of three beams with the space between the beams filled with balsa. The beams and balsa were covered with an aluminum skin which was brought up to proper aerodynamic contour with balsa and covered with Japanese tissue. The distribution of corrective masses for the model stabilizers was determined from the data obtained by cutting up a pilot model without corrective ballast and measuring its mass distribution. The difference between this distribution was made up with thin lead sheets attached to the aluminum skin. The later design was made by machining the beam grid from a solid plate and filling the voids with balsa. The corrective masses were then added and the stabilizer was covered with Japanese tissue. This construction was found to yield a satisfactory simulation of the plate-like vehicle stabilizer.

A sting mount was designed for the purpose of running flutter tests with a single stabilizer. Root attachment springs were included to simulate the root stiffness conditions of the fuselage.

All components of the model were thoroughly checked by CVC personnel prior to acceptance of the model from the model subcontractor. The stiffness and mass properties of the models were closely checked and modified where necessary in an attempt to keep these properties to within 15% of the design values. However, some compromises with stiffness had to be made in the interest of greater strength.

The stiffness of the fuselage structural tube was measured in the following manner. The tube was cantilevered at the tail cone break point and loaded with a shear load at the location of the elevators. Mirrors were placed along the tube at equal intervals and the angular deflection of light beams reflected from these mirrors measured for the loaded condition. These deflections were reduced to stiffness distributions and compared with scaled vehicle stiffness curves and calculated model stiffness curves. This comparison is shown in Figure 5. A plot of the distribution of the stiffness ratio along the fuselage is shown on the same figure based on the calculated stiffness distribution. The model stiffness was high in the midsection because of the difficulty in machining the fuselage tube to within less than 0.010-inch wall thickness.

The inertial properties of the completely assembled model were measured as follows. First, the model mass was measured with an accurate balance and the center of mass located. The moment of inertia about the center of gravity was then measured by swinging the model as a bifilar pendulum with the axis of rotation through the center of mass. The comparison of model and design mass data are shown in Table 2.

A pendulum type device was made to measure the impulse of the ejection mechanism. The simulated store was fired horizontally from the ejector mounted on the pendulum and the maximum amplitude of the pendulum swing measured. This amplitude was related to the impulse of the ejection mechanism by the use of the geometry and inertial characteristics of the pendulum. After the ejection mechanism was calibrated to yield approximately 0.11 lb_f-sec impulse consistently, it was installed in the fuselage tube. The ejection mechanism was static fired several times prior to the tunnel runs, and high-speed photographs were taken of an ejection. The impulse was calculated by measuring the exit velocity from these sequence photographs and multiplying it by the mass of the slug. This resulted in a precise measurement of the ejection impulse of 0.1095 lb_f-sec. The structural damping was calculated from a trace showing the bending moment time history at a point 18.38 inches from the nose. The structural damping was found to be 2% of the equivalent critical viscous (linear) damping.

Initial testing of the stabilizers was done with a mounting block designed to simulate a cantilever condition at the stabilizer attachment points. This block was clamped to a rigid test fixture and mirrors placed on the stabilizer at the panel points. The stabilizer was loaded and angular deflections of these mirrors in the x and y directions measured by the light beam method mentioned above. These measured angular deflections were compared with corresponding data derived analytically. A sample of these comparisons is shown in Figures 6 and 7 for the x and y angular deflections respectively.

The mass of each completed stabilizer was measured with an accurate balance and the center of mass was located by balancing it along two axes with a knife edge. The moments of inertia of each stabilizer were measured about two mutually perpendicular axes by swinging each stabilizer as a bifilar pendulum. As mentioned earlier, a pilot model was constructed and cut up for the purpose of obtaining mass distributions of the models. Each individual bay was weighed and the corrective masses and locations thereof required to bring the models into agreement with the design values were calculated. Lead weights were added to each subsequent model to provide these corrections.

The root stiffness of the sting root mounting springs was measured with a combination of a mirror to detect angular motion and a dial gage to detect lineal motion. The comparison between the design root influence coefficient matrix and the measured root influence coefficient matrices are shown in Figure 8.

An acoustic shaker was used to excite the stabilizer models for the natural frequency checks. A vibration pickup with its output connected to an oscilloscope was used to detect the motion of the models and salt was sprinkled over the surface to define the node lines. A sample comparison of the measured and calculated node lines and frequencies for the cantilevered root condition are shown in Figure 9.

III. TESTING TECHNIQUES

All wind tunnel tests were conducted in the CVC High Speed Wind Tunnel. The characteristics of this tunnel are summarized in Figure 10. This tunnel was chosen because of its large size (4' by 4'), wide Mach number capability (0.2 to 5.0), and high dynamic pressure capability (5,000 psf at Mach 3.6).

The disadvantage of an unevacuated blowdown tunnel is the existence of high starting loads when running supersonic tests. These loads resulted in several premature structural failures of both the stabilizer and the fuselage.

A stabilizer was mounted on a sting with root supports which simulated the bulkhead flexibility for the purpose of flutter testing. The frequencies of each model being tested were checked after each run to check for possible structural failures during the run. This served the dual purpose of checking for flutter of the surface and indicating the serverity of the tunnel starting and unstarting loads.

Each of the stabilizers was instrumented with two sets of strain gages. One set was oriented to pickup spanwise loads, and the other set was oriented to pick up chordwise loads. Each of the strain gage traces was recorded on an oscillograph type recorder simultaneously with several tunnel parameters. In addition, each test was covered with a high-speed movie camera running at approximately 1,000 frames a second. A stabilizer was successfully flutter tested up to Mach 2.0. The model was stable during the run but was broken by the unstart shock.

A set of stabilizers, modified for greater strength, was fabricated for a second series of tests. The most important modification was that the strength of the rear beam was doubled. It was found that the beam was then strong enough, but that the skin (which is only 0.002-inch thick 2024-ST aluminum) began breaking directly behind the middle beam on high Mach number runs. Thus, although one weak point was eliminated another was brought to light.

The complete dynamic model was mounted on the sting for tunnel testing as shown in Figure 2. The balsa fairing was broken on the first run of the first series of tests necessitating that the model be modified and rebuilt before testing could continue. Even after the model had been strengthened, the only data obtained without using a protective device was at Mach 1.6.

The response due to elevator deflections was measured first. The elevator actuator motor was controlled by a switch in the tunnel control room. The elevator was deflected slowly up to 5° and snapped back with a spring. After the shock had gone down the tunnel, the elevators were activated and several responses for elevator inputs were measured. Next, the response due to a store ejection was measured. The air pressure value was controlled by a switch from within the tunnel control room. The shape of the force-time curve has been described previously.

The model was badly damaged with the starting and unstarting shocks on the first run at Mach 2.2. The left stabilizer was lost during the start, but the right stabilizer remained intact during the run and apparently was lost during the tunnel shutdown. This ended the attempts to test this model without some sort of protective device to shield the model from the high loads experienced during tunnel start and unstart.

A set of proximity plates were designed and installed in the tunnel to protect the model during the starting and unstarting conditions. The plates consisted of steel channels which completely enclosed the model on all sides and were open on both ends. The plates were hydraulically operated on command from the tunnel control room, requiring approximately 5 seconds for actuation. The model was enclosed during the tunnel start and then the plates were retracted to the tunnel wall while data were measured. When the desired information had been recorded, the plates were extended to protect the model again during the unstart conditions. It is estimated that the protective plates reduce the starting and unstarting loads approximately 50% to 75% in the Mach 2.0-3.0 range. However, high-oscillating loads were introduced while the model was fully enclosed by the plates, with immediate relief of these loads noted upon initial plate movement. Separating the plates initially, approximately 1/4 inch from the closed position, resulted in considerable reduction of these oscillating loads. This method of protecting models is in a developmental stage and requires further study and tests.

Strain gage instrumentation was used at two stations on the model, at 21.3 inches and 28.8 inches from the nose. The strain gages were mounted directly on the top and bottom of the fuselage structural tube. The instrumentation was calibrated by noting the deflections of the oscillograph traces for known loading conditions and obtaining a scale factor in inch-pounds per inch of trace deflection.

Immediately prior to each run, the model was shaken with an electromagnetic shaker to determine the first few natural frequencies. This was done as a check on the structural soundness of the model on the premise that any failures would manifest themselves in frequency shifts in the model.

Finally, the proximity plates were closed to protect the model during the tunnel start and the actual wind tunnel test begun. After the starting shock had gone down the tunnel, the proximity plates were retracted and the high-speed movie cameras started. The store ejection was automatically triggered to occur 1 second after the start of the movie cameras and the elevators were actuated manually approximately 1 second after the store ejection. After a few readings had been obtained for elevator inputs, the proximity plates were replaced to protect the model from the unstart shock and the tunnel was shut down. Each wind tunnel run required approximately 15 seconds of run-time.

The data points obtained in this manner are summarized in Table 3.

IV. TEST RESULTS

Vertical bending moment-time histories were obtained for both elevator and store ejection inputs at the conditions summarized in Table 3.

It was found that the model was bottoming out against the sting for the initial elevator deflection, thereby complicating the interpretation of the results. However, the data obtained was quite clear with a minimum of background "noise" from the tunnel turbulence. A reproduction of a typical data trace for elevator inputs is shown in Figure 11.

The data obtained for the store ejections had no extraneous inputs as encountered in the elevator deflection tests. The data obtained was very clear for all conditions. A reproduction of a typical data trace for store ejection is shown in Figure 12 and a time sequence of the store trajectory at M = 3.0 is shown in Figure 13.

The model construction and testing are discussed extensively in reference 1.

V. COMPARISONS WITH ANALYTICAL STUDIES

In defining the physical system and formulating the mathematical model for use with a digital computer, the continuous system is replaced with a discrete system of collocation points by the application of certain interpolation procedures and Lagrange's equations of motion. The model fuselage was idealized as a one-dimensional body whose aeroelastic properties are described as functions of a single spacial coordinate along the fuselage. The first four calculated mode shapes and frequencies are shown in Figure 14 compared with measured data from the model test.

For the purposes of analysis, the stabilizers are idealized as plates with integral stiffeners. The aeroelastic properties are described as functions of two spacial coordinates in the plane of the stabilizer. The first six calculated node lines and frequencies are compared with measured node lines and frequencies for a typical stabilizer with flexible supports in Figure 15.

The results of the "bent body" pressure distribution measurements of reference 2 were used as the basis of the development of the aerodynamic influence coefficient matrices for Mach 3.0 flight conditions. Two-dimensional piston theory was used for the aerodynamics of the stabilizers and elevators.

The methods of analysis are discussed in detail in references 1 and 3.

VI. COMPARISONS OF TEST RESULTS AND ANALYSIS

The primary purpose of these tests was to provide an empirical check on the assumptions and methods utilized to calculate the transient loads on the vehicle. Because it was not feasible to achieve a free-flight condition in the wind tunnel, the model, including the tunnel mounting system, was analyzed for direct comparisons. The philosophy here is to approach as complete a simulation as possible with the model and assume that the assumptions and method of analysis are adequate for the full-scale vehicle if they are adequate for the model.

Transient responses of the mathematical model were calculated by solving the equations of motion with a numerical integration technique. The force input time-history used for the store ejection analysis is the same as the one described in Section II. The elevator input analysis was approached as an initial deflection problem. It was assumed that the ramp up was slow enough to induce insignificant dynamic response in the model until the elevators were snapped back to zero with the return spring (see Figure 11). Thus, the initial deformed shape for a static elevator deflection of 5° was calculated and used as the static initial condition for an analysis of the dynamic system with zero elevator deflection. As mentioned earlier, it was found that the model was bottoming against the sting initially, requiring that the problem be run in two parts to obtain the complete solution. Dynamic loads were calculated from these responses by application of the modal acceleration concept for calculating collocation point loads.

A comparison of the calculated and measured bending moments for a zero airspeed store ejection is shown in Figure 16 and comparisons for store ejection and elevator inputs at Mach 3 conditions are shown in Figures 17 and 18 respectively. As a matter of interest, the calculated load-time history for a store ejection on a system without the sting support springs (free-free) is included in Figure 17.

VII. CONCLUSIONS

It has been demonstrated that relatively fragile dynamic models can be tested successfully at supersonic speeds in unevacuated blow-down wind tunnels if protective devices are employed to reduce the start and unstart loads on the model. Also, it has been found that transient loads may be measured on a dynamic model and correlated with analytical results with good agreement.

REFERENCES

1. Chance Vought Corporation. (U) Aerothermodynamic Data and Design Criteria Pertinent to the Development of the Propulsion System of a Supersonic, Low Altitude, Nuclear Propelled Vehicle. ASD-TDR-63-165. Aeronautical Systems Division, Wright-Patterson Air Force Base, Ohio. March 1963. (SECRET REPORT)

2. Frank H. Durgin and William C. Noz, Jr. The Effects of Body Camber on Body Pressure Distributions and Wing Forces for Mach Numbers From 2.0 to 7.6. Massachusetts Institute of Technology, Naval Supersonic Facility, Wind Tunnel Report 479. April 1961.

3. Chance Vought Corporation. (U) Tests, Studies, and Investigations for Development of Airframe, Propulsion, Secondary Power, Avionics, Boosters, Payloads, Flight Test Subsystems, Air Conditioning, Support, Range and System Studies Technology Required for the Low Altitude Supersonic Vehicle Program. ASD-TDR-63-947. Aeronautical Systems Division, Wright-Patterson Air Force Base, Ohio. 1964. (SECRET REPORT). (In preparation.)

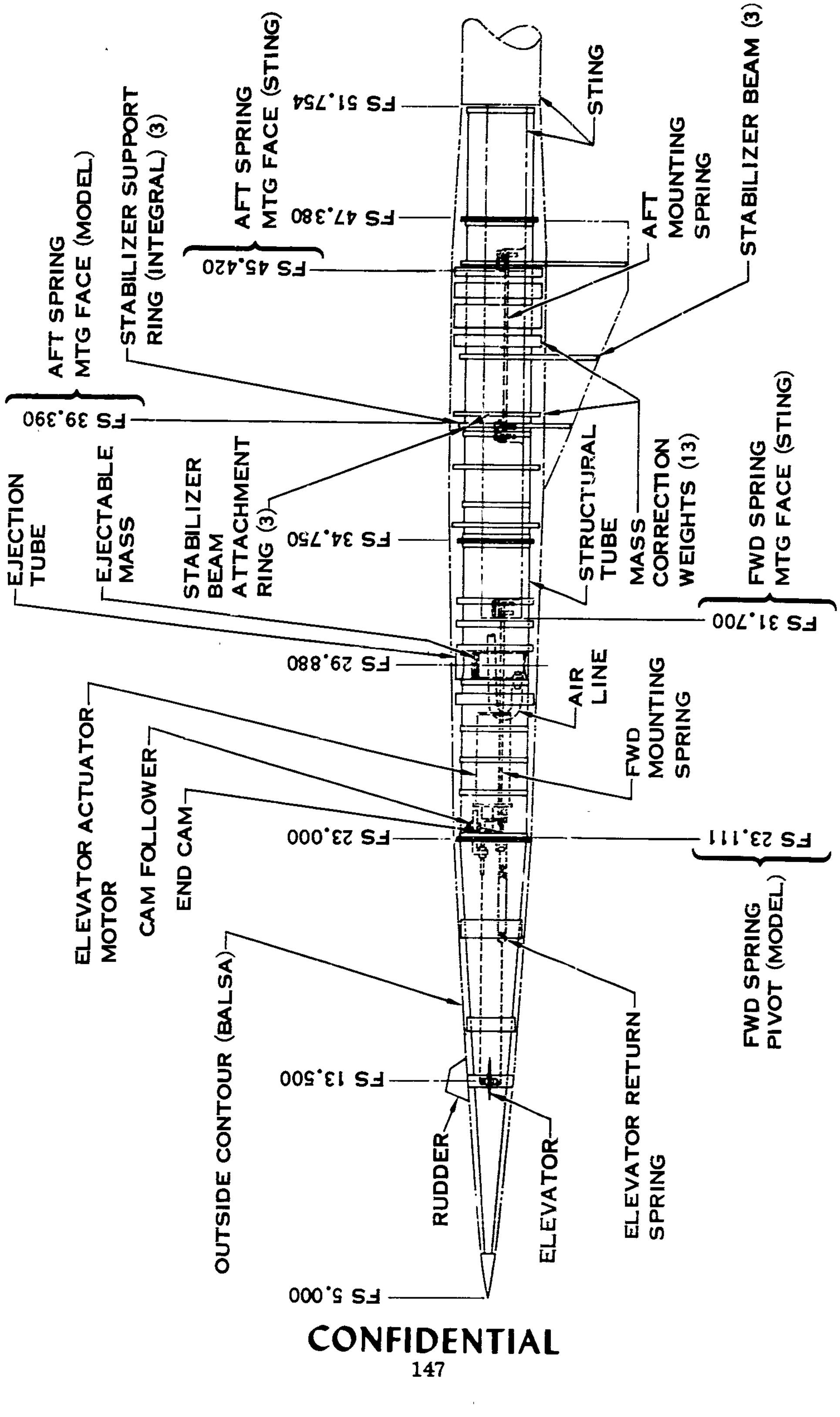

Figure 1. General Arrangement of Fuselage Model

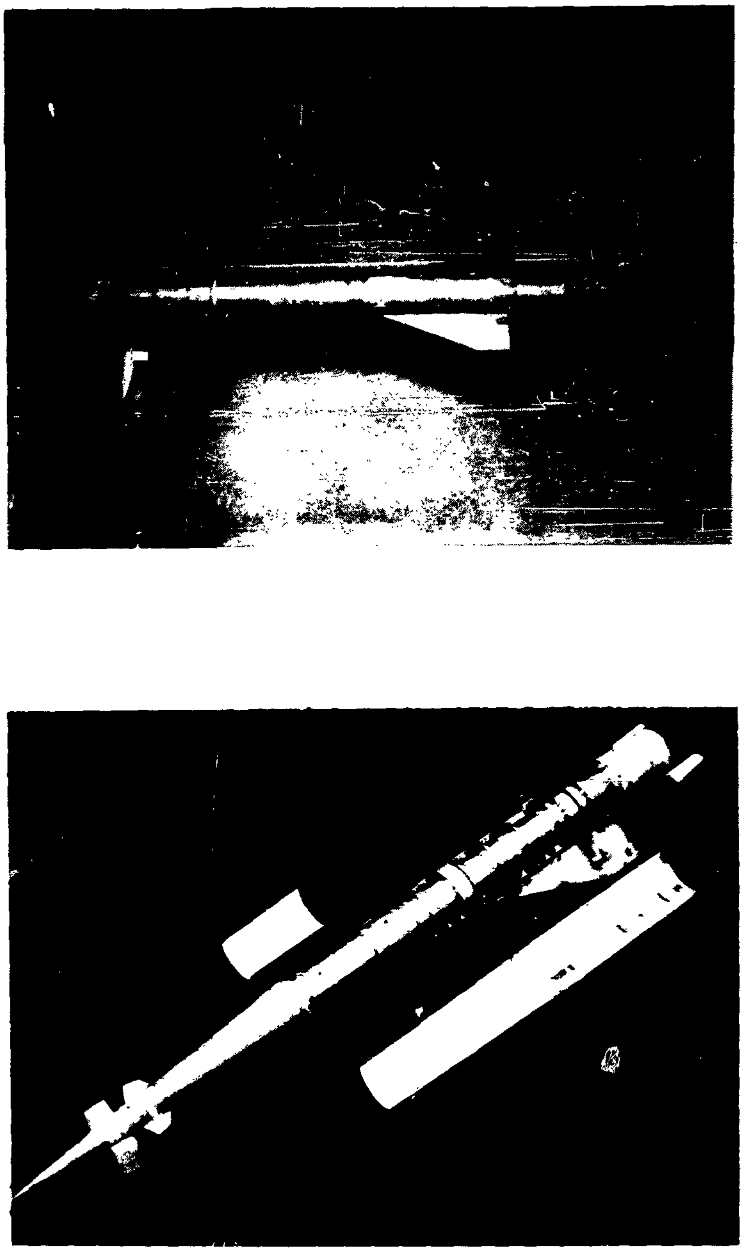

Figure 2. Complete Model and Cutaway View

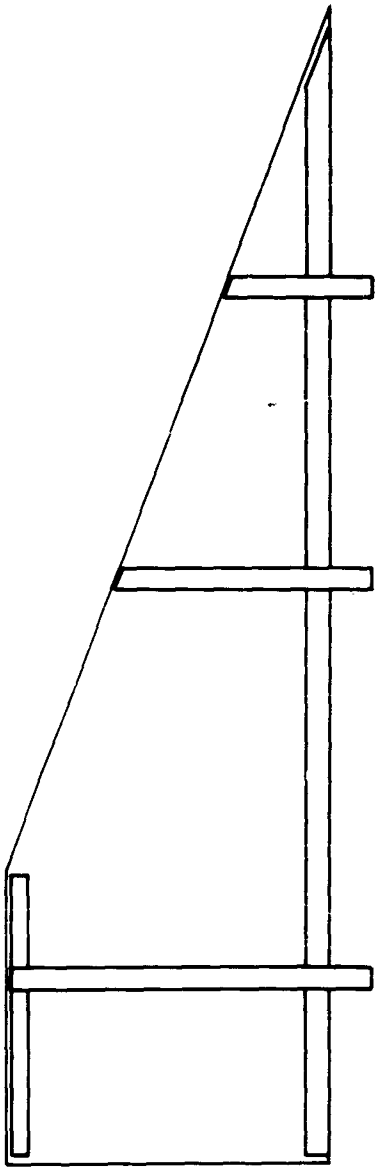

Figure 3. Planform of Original Stabilizer Design

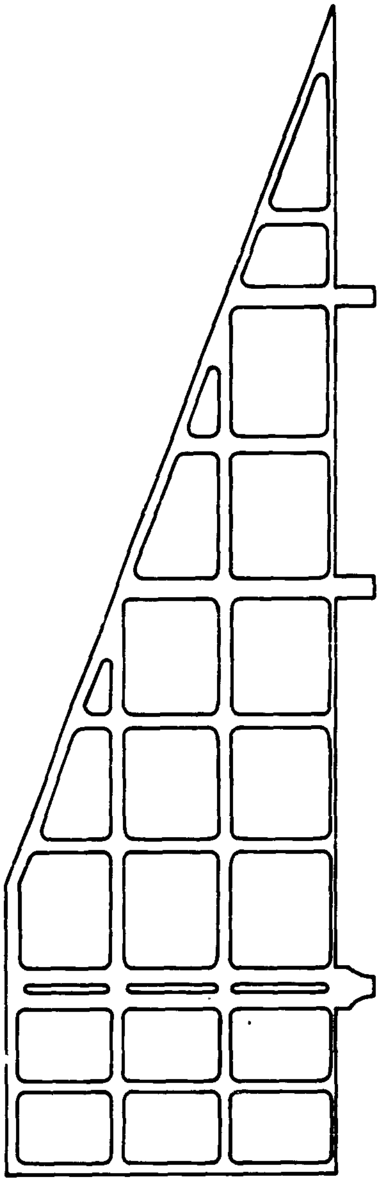

Figure 4. Planform of Final Stabilizer Design

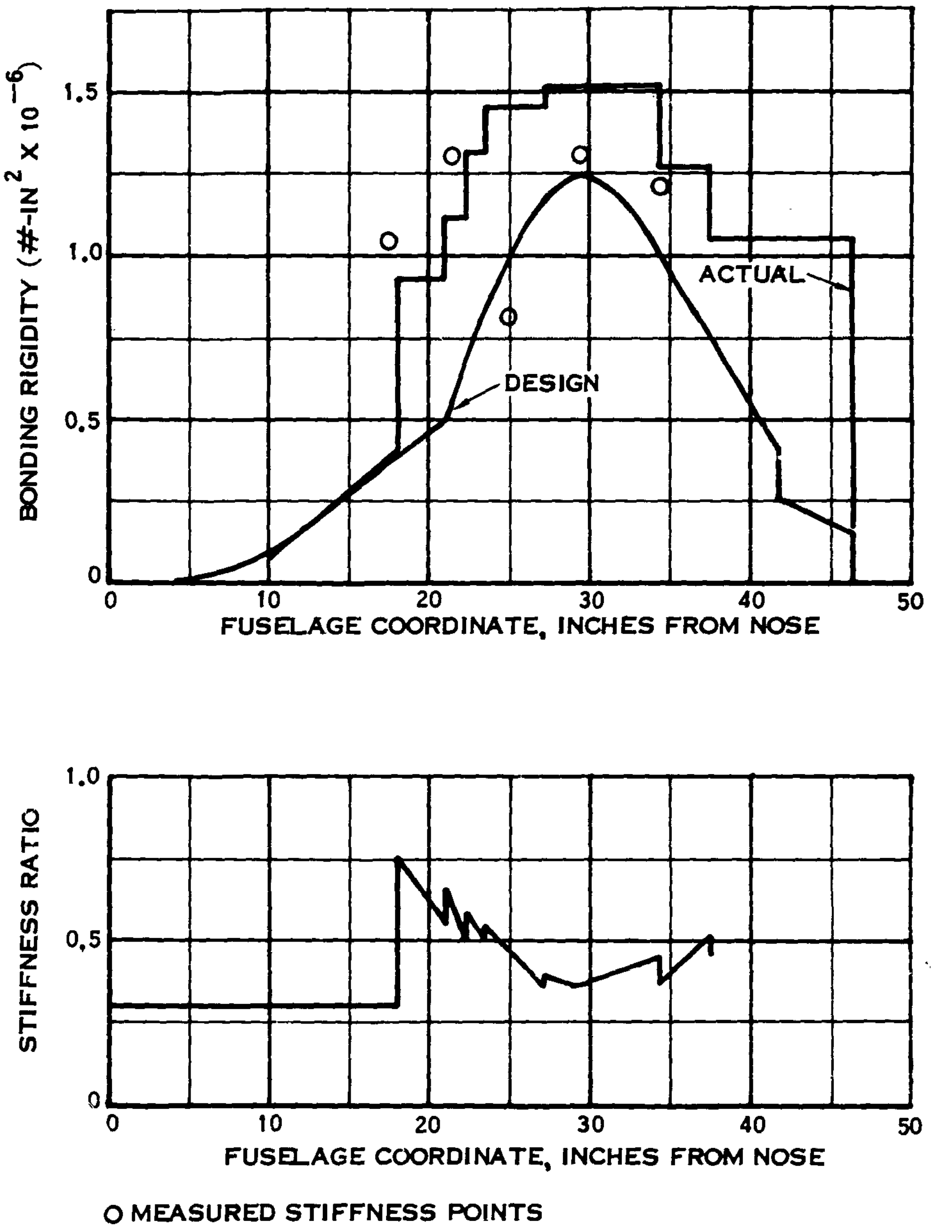

Figure 5. Comparison of Fuselage Model Stiffness Distribution with Target Stiffness Distribution

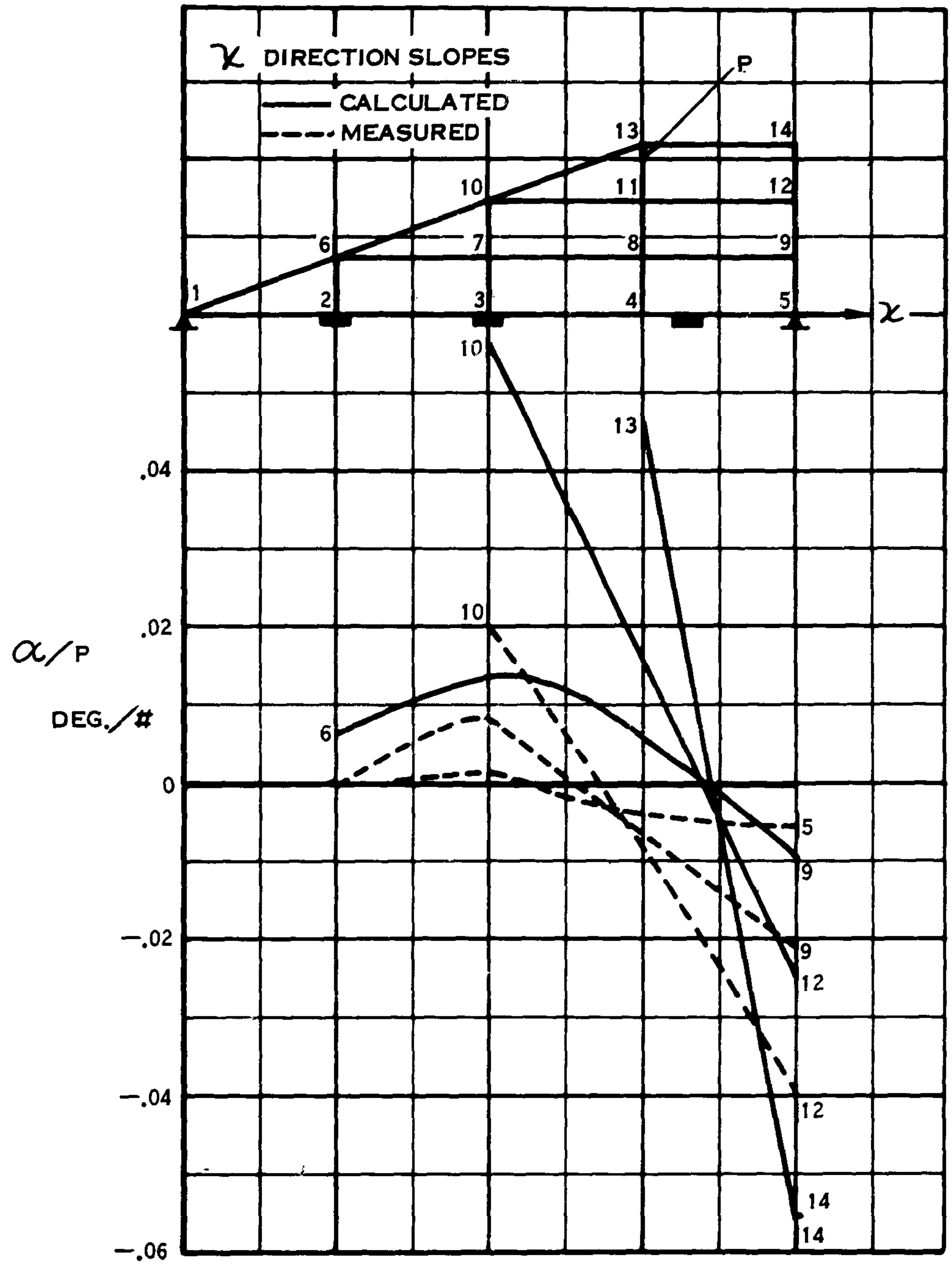

Figure 6. Angular Influence Coefficients for Stabilizer Compared with Calculated Values in the Chordwise Direction

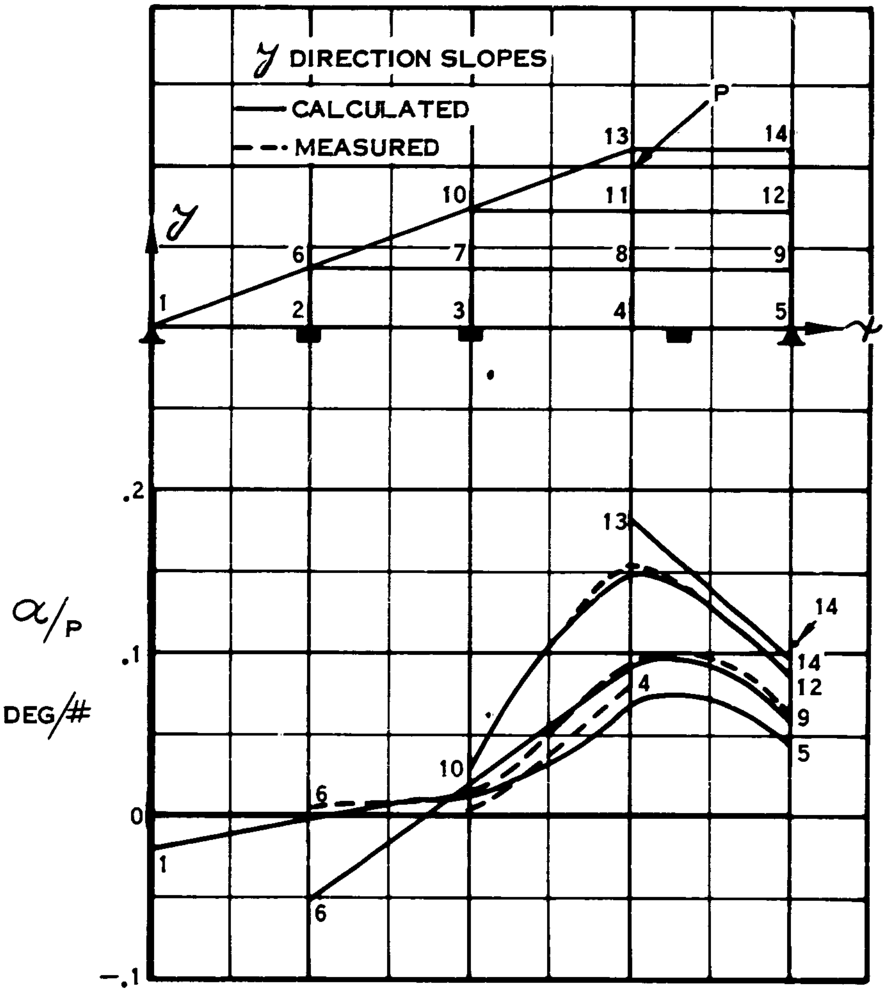

Figure 7. Angular Influence Coefficients for Stabilizer Compared with Calculated Values in the Spanwise Direction

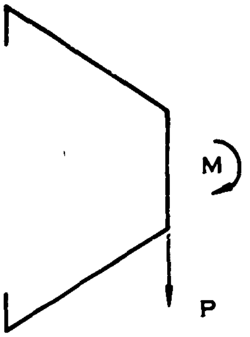

DESIGN

$$\begin{Bmatrix} \delta \\ \theta \end{Bmatrix} = \begin{bmatrix} 1.735 \times 10^{-4}, & -3.73 \times 10^{-4} \\ -3.73 \times 10^{-4}, & 13.33 \times 10^{-4} \end{bmatrix} \begin{Bmatrix} P \\ M \end{Bmatrix}$$

$$\begin{Bmatrix} \delta \\ \theta \end{Bmatrix} = \begin{bmatrix} 1.7 \times 10^{-4}, & -3.98 \times 10^{-4} \\ -4.98 \times 10^{-4}, & 12.1 \times 10^{-4} \end{bmatrix} \begin{Bmatrix} P \\ M \end{Bmatrix}$$

Figure 8. Comparison of Calculated and Measured Flexibility Matrices for the Stabilizer Model Root Springs

CONFIDENTIAL

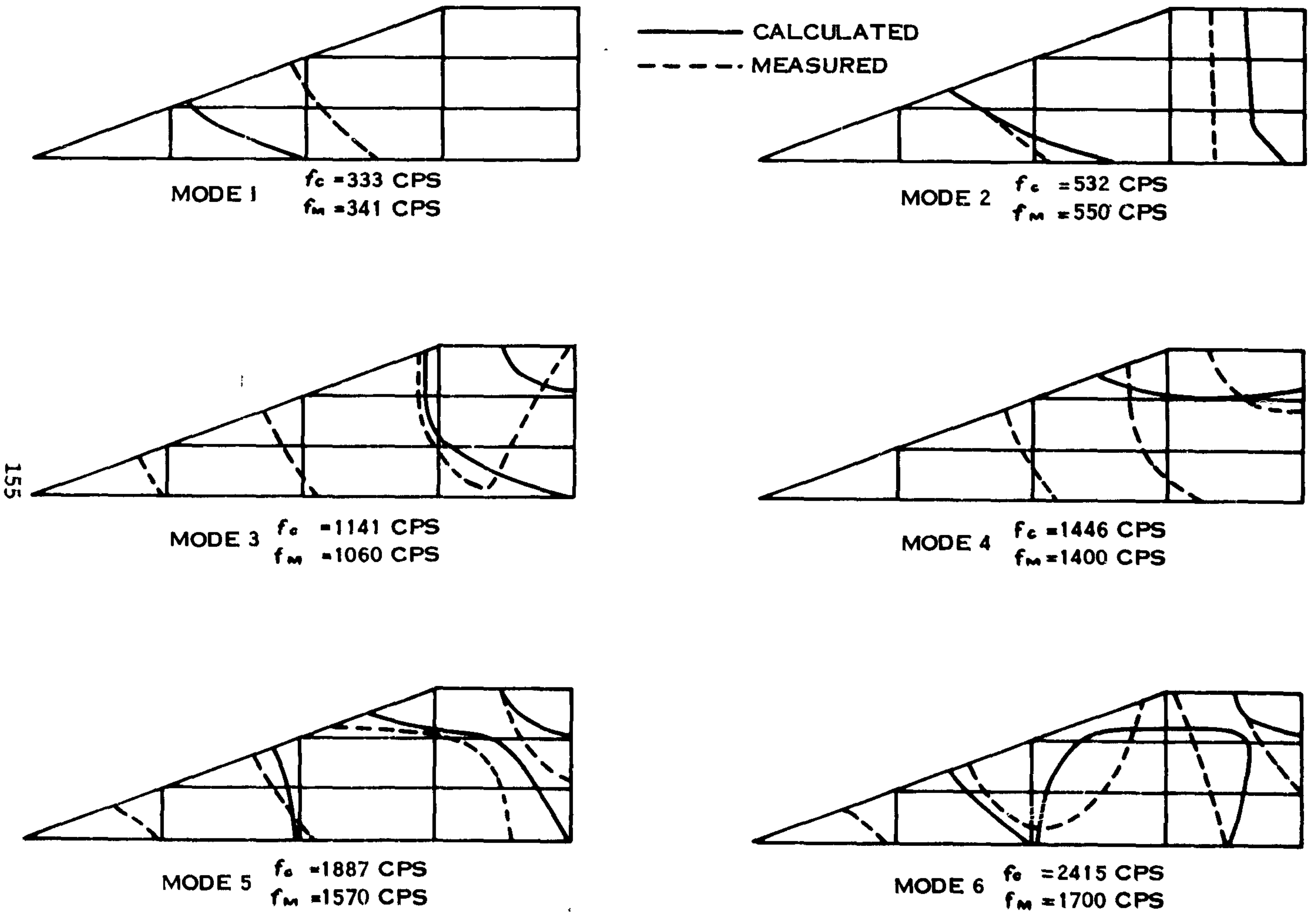

Figure 9. Stabilizer Node Lines and Frequencies for Cantilever Root Restraints

CONFIDENTIAL

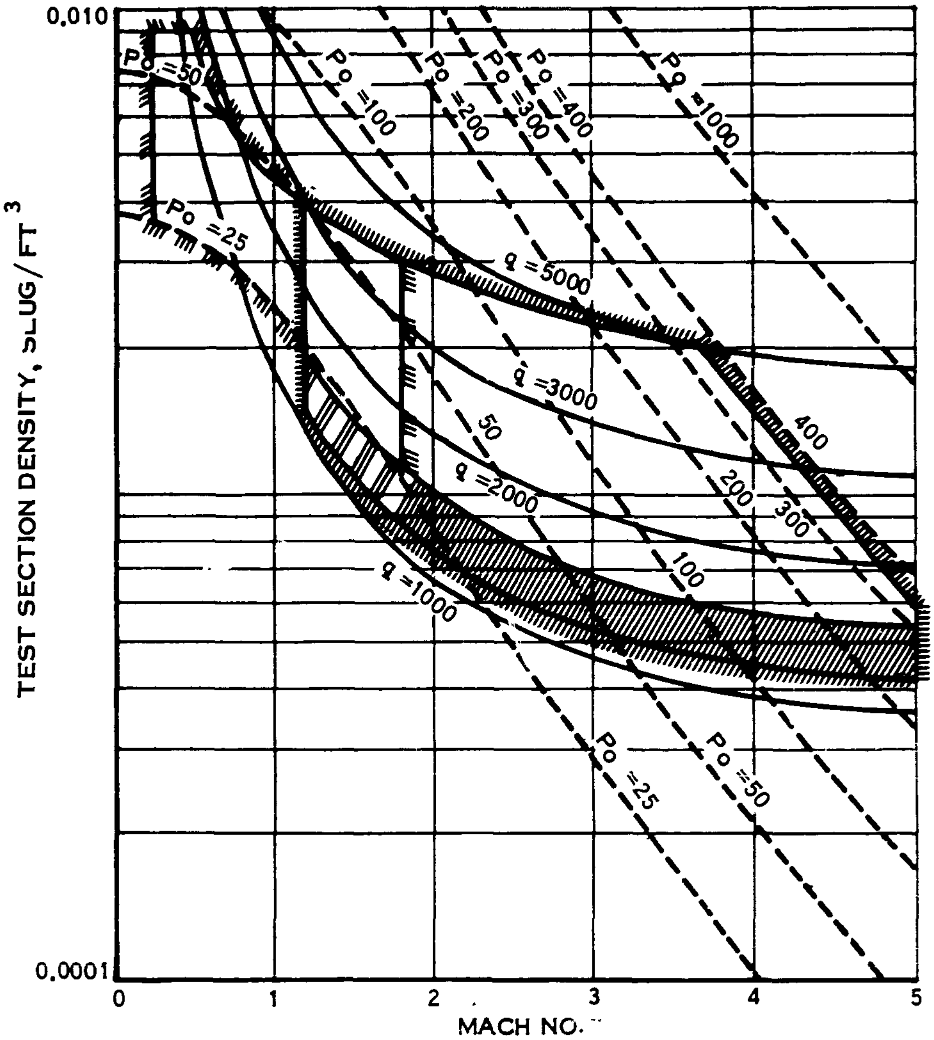

―――――― CONSTANT DYNAMIC PRESSURE, q , PSF

– – – – – CONSTANT STAGNATION PRESSURE, Po , PSIA

////////////////// SUPERSONIC SECTION OPERATING LIMITS

//// //// //// // TRANSONIC SELECTION OPERATING LIMITS

OPERATIONAL CHARACTERISTICS
OF CHANCE VOUGHT 4′ X 4′
HIGH SPEED WIND TUNNEL
DENSITY—MACH NUMBER ENVELOPE
AT STAGNATION TEMP OF 100° F

Figure 10. CVC High Speed Wind Tunnel, Test Section Density Variation as a Function of Mach Number

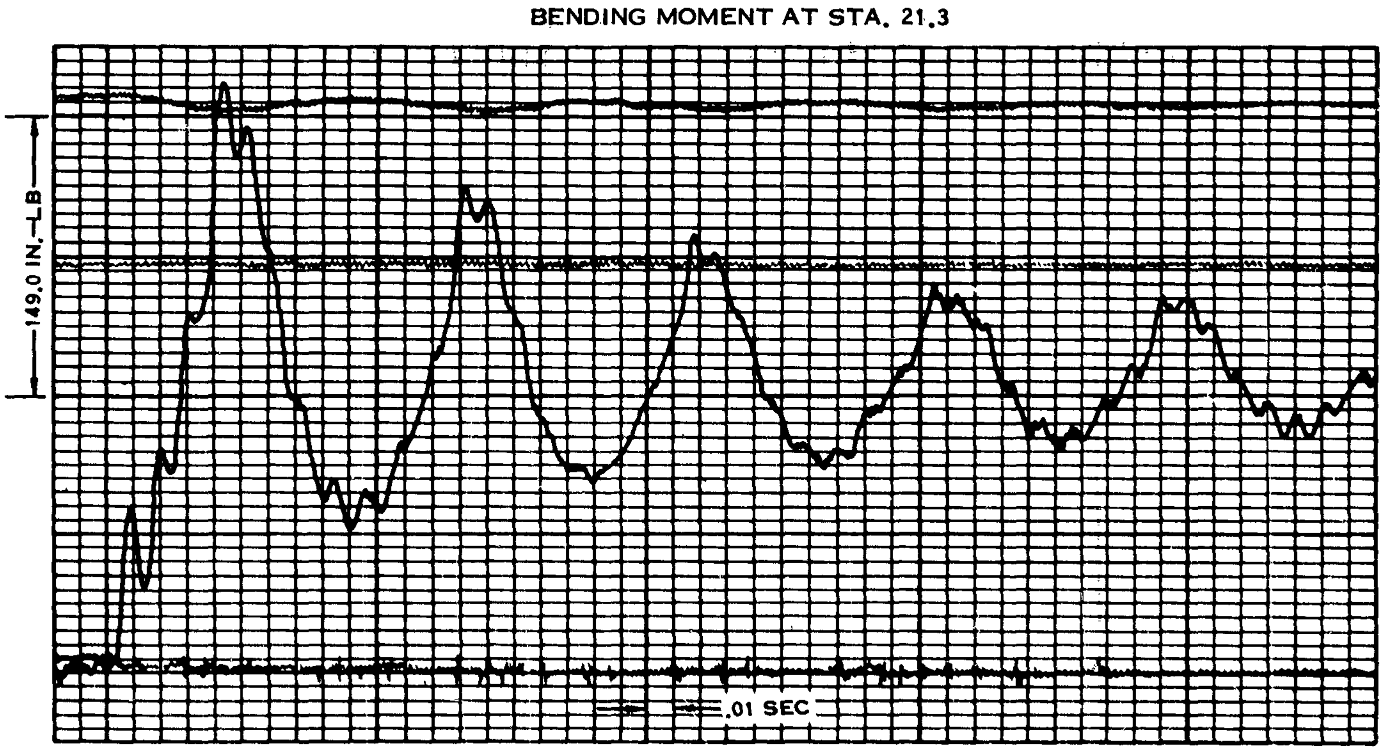

Figure 11. Typical Data Trace for Elevator Inputs (M = 3.0)

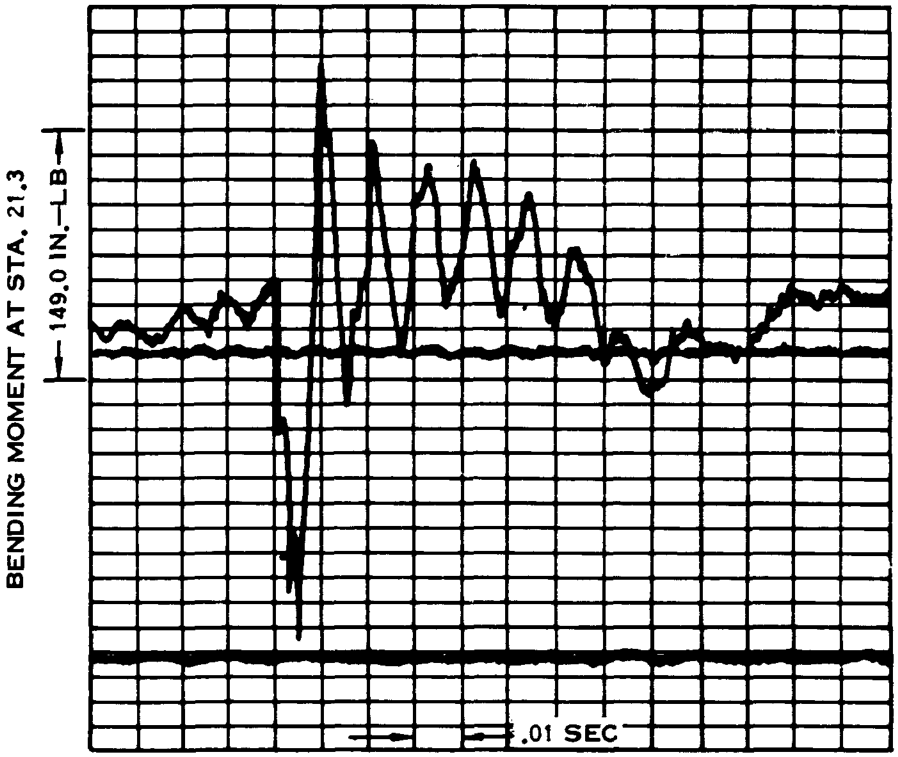

Figure 12. Typical Data Trace for Store Ejection (M = 3.0)

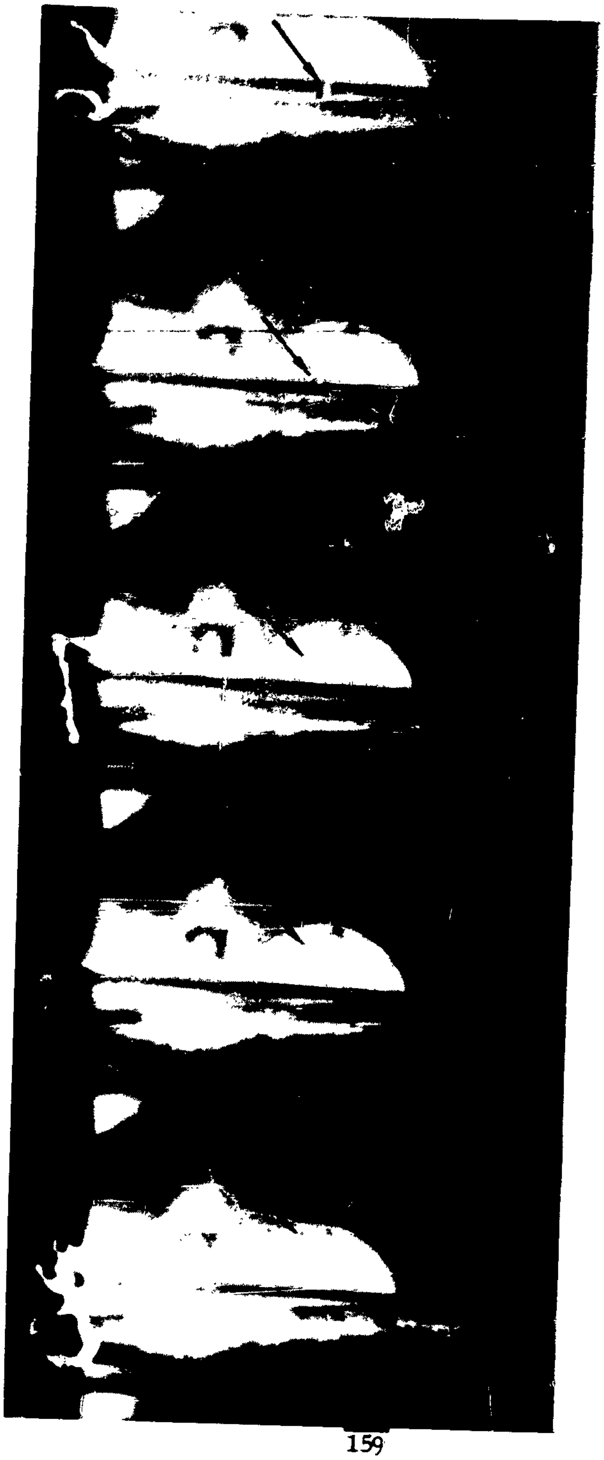

Figure 13. Time Sequence for Store Trajectory at $M = 3.0$

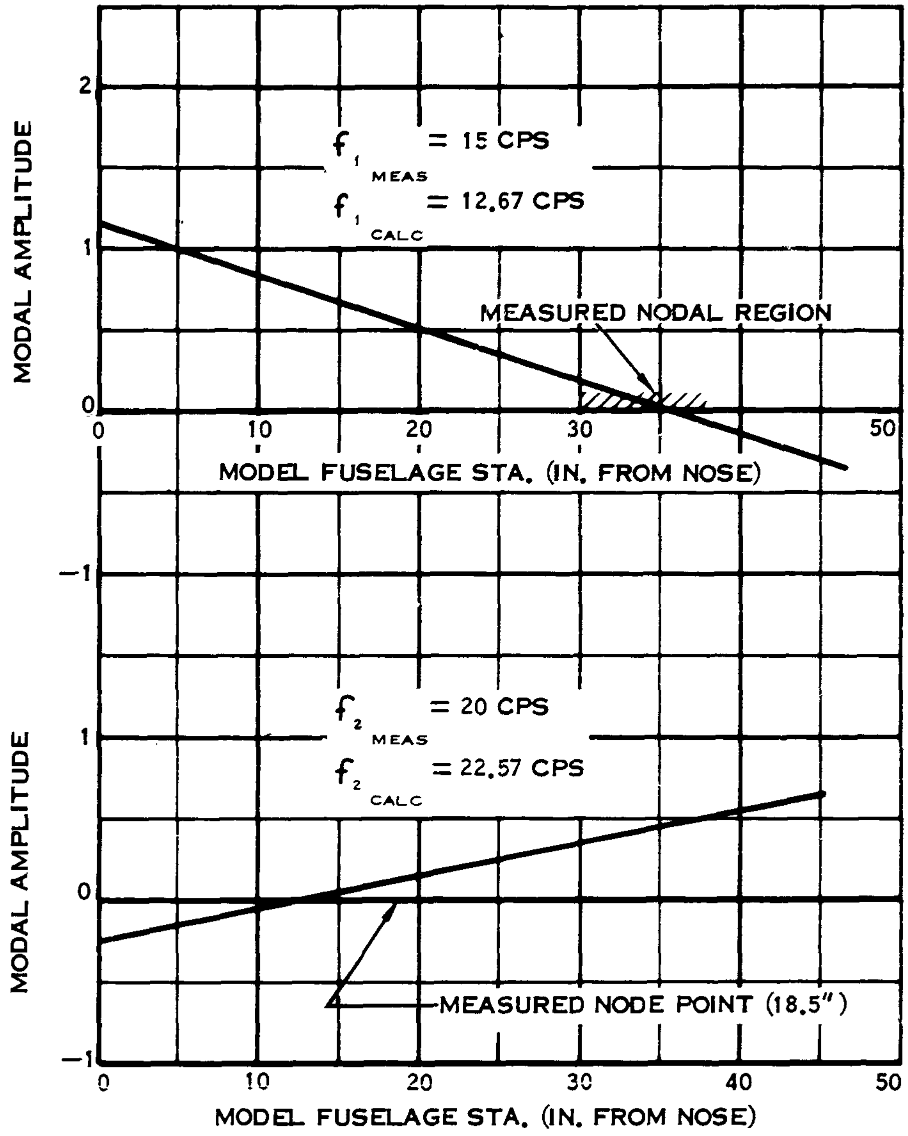

Figure 14. Calculated Rigid Body Mode Shapes for the Fuselage Model as Installed on Tunnel Sting

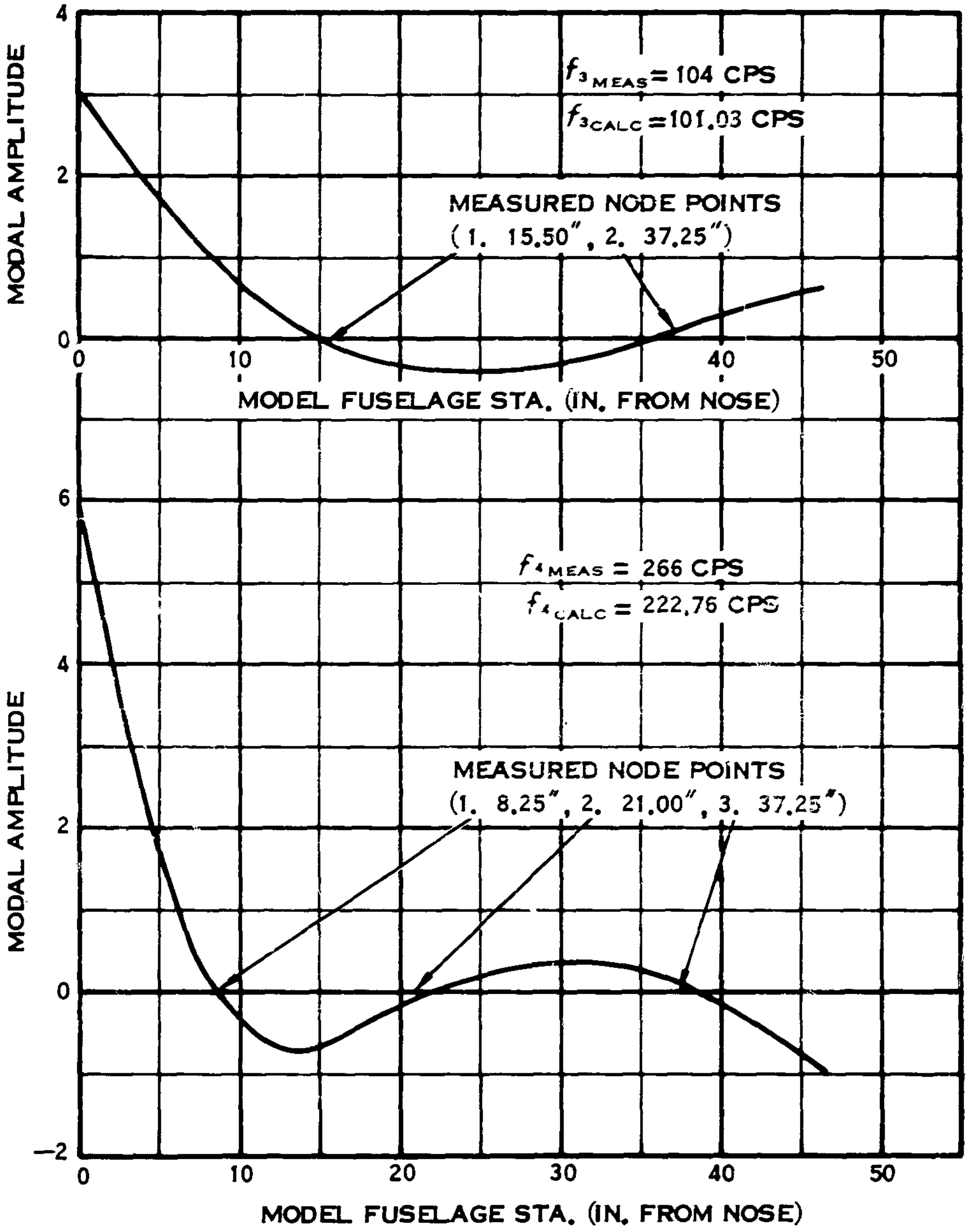

Figure 14.A Calculated Elastic Mode Shapes for the Fuselage Model as Installed on Tunnel Sting (Continued)

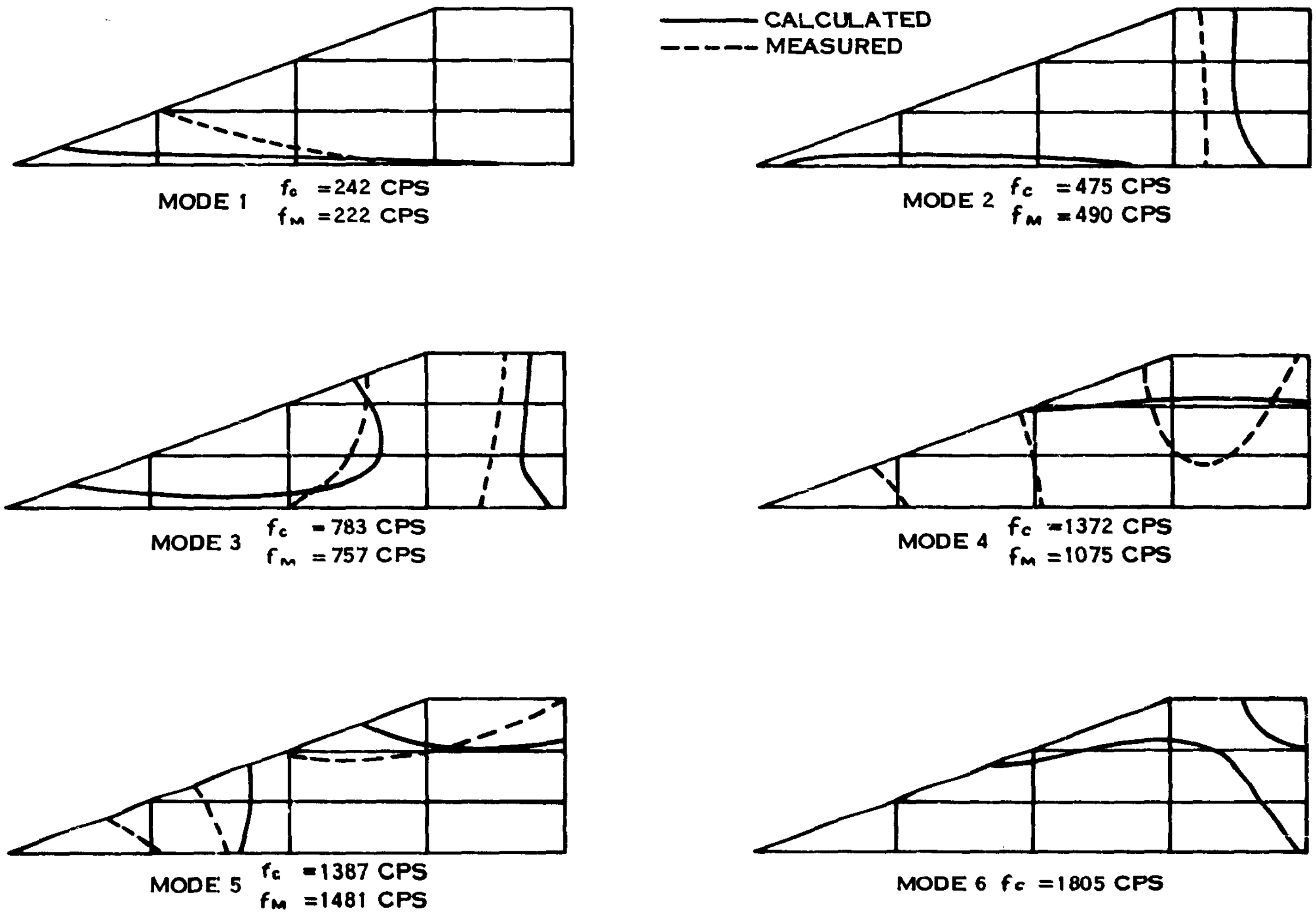

MODE 1 f_c =242 CPS f_M =222 CPS

MODE 2 f_c =475 CPS f_M =490 CPS

MODE 3 f_c =783 CPS f_M =757 CPS

MODE 4 f_c =1372 CPS f_M =1075 CPS

MODE 5 f_c =1387 CPS f_M =1481 CPS

MODE 6 f_c =1805 CPS

Figure 15. Stabilizer Node Lines and Frequencies for Design Root Restraints

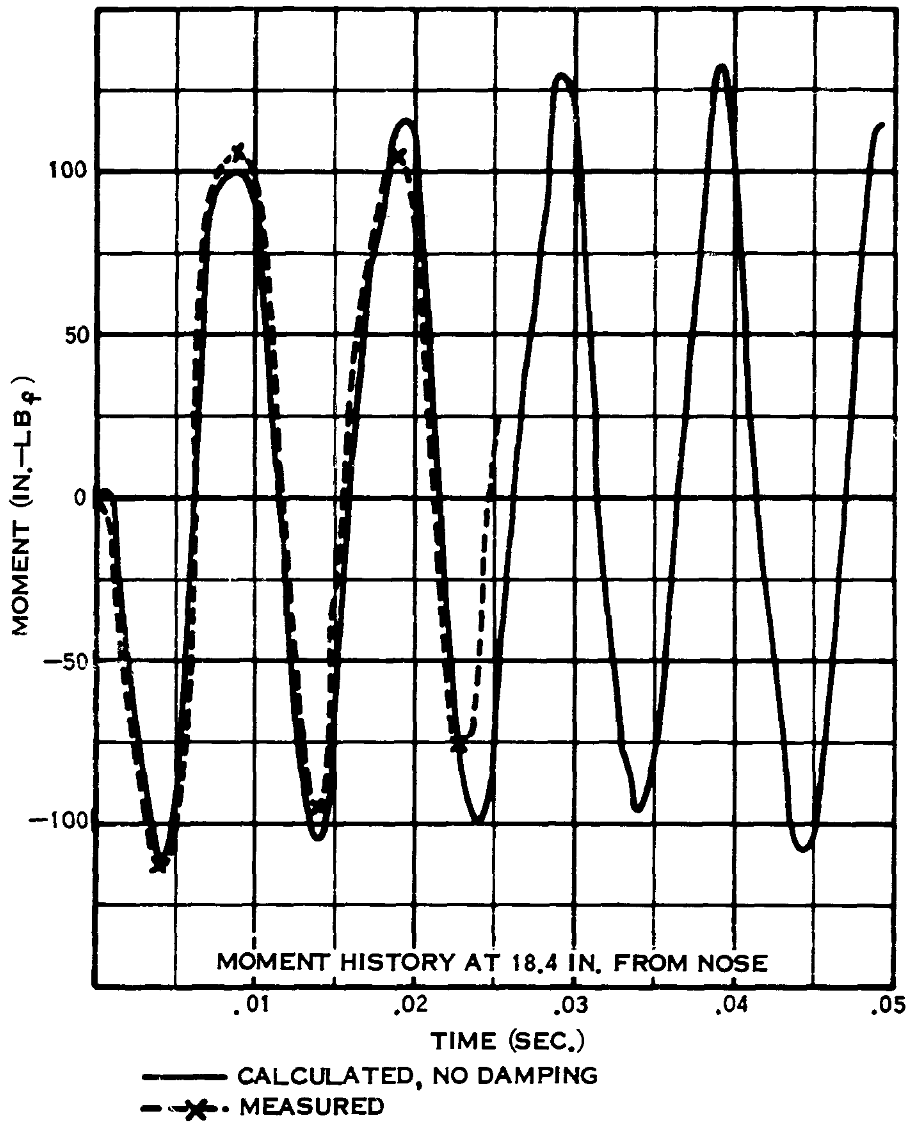

Figure 16. Comparison of Calculated and Measured Bending Moments for a Zero Airspeed Store Ejection

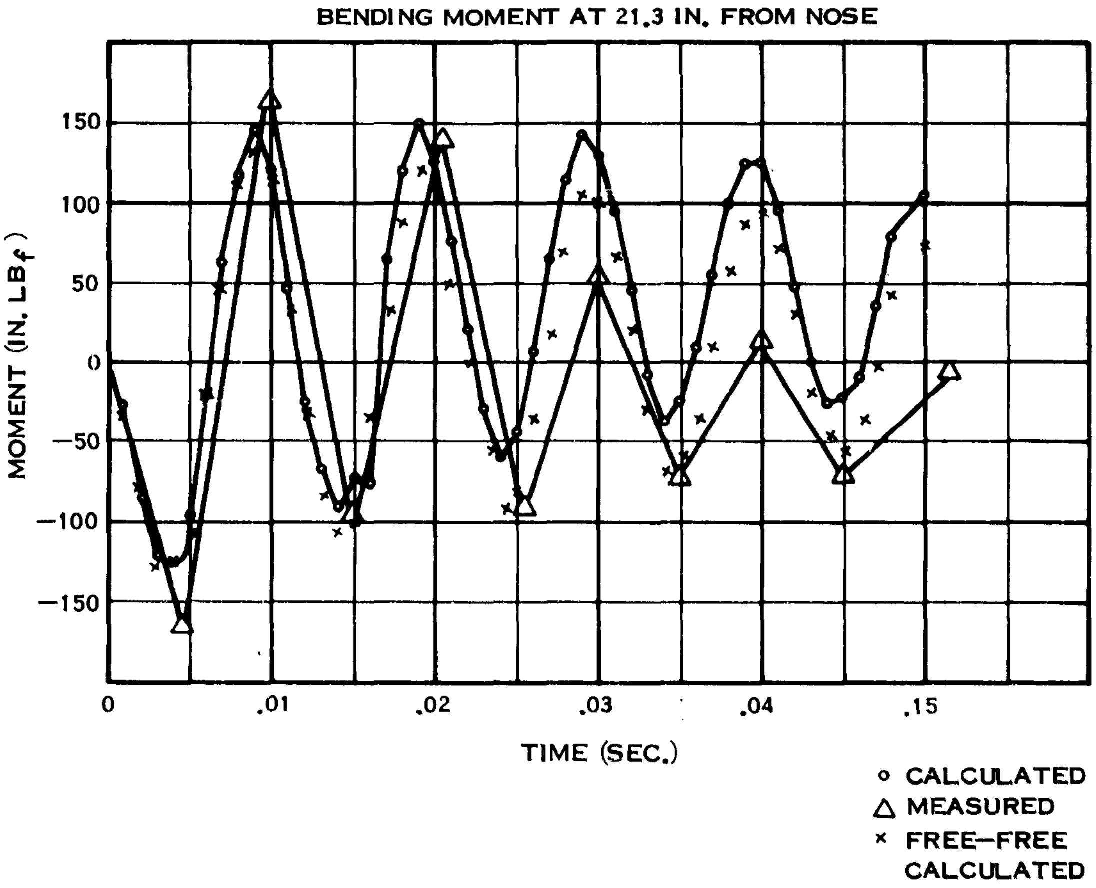

Figure 17. Comparison of Calculated and Measured Bending Moments for Store Ejection Input

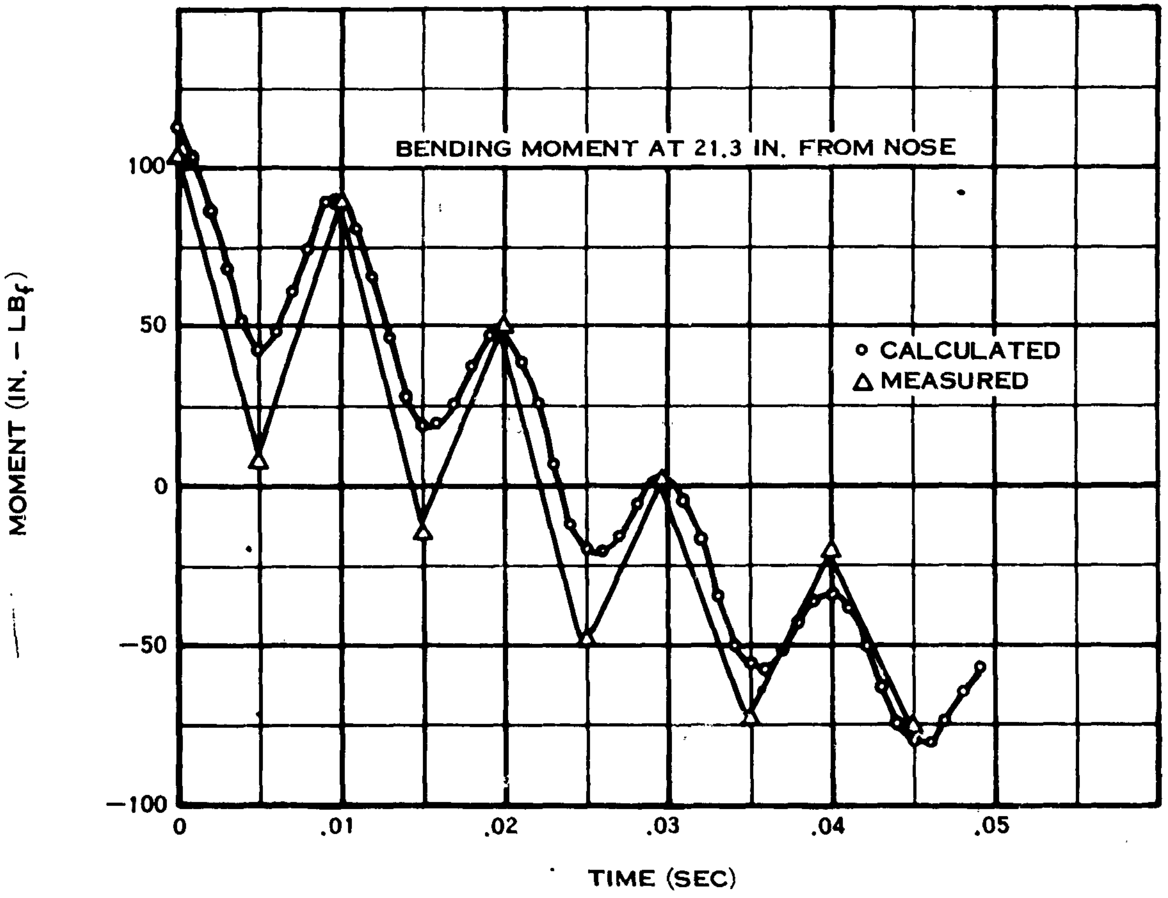

Figure 18. Comparison of Calculated and Measured Bending Moments for Elevator Input

Table 1. Comparision of the Calculated "Free-Free" and the Calculated As-Installed-On-The-Sting Frequencies of the Complete Fuselage-Stabilizer Model

	FREE—FREE FREQUENCIES CPS	STING MOUNTED FREQUENCIES (CALC) CPS
1	0	12.67
2	0	22.57
3	100.46	101.03
4	222.57	222.76
5	313.17	313.68

Table 2. Summary of Complete Model Inertial Data

	MASS (GM)	C.G. (IN FROM NOSE)	I_{CG} GM IN^2	MASS RATIO	FREQ RATIO	STIFFNESS RATIO
MODEL	3250	30.3	3.25×10^6	1.03	0.606	[illegible]
DESIGN	3124	29.47	3.22×10^6	1.00	0.548	[illegible]

Table 3. HSWT Test Points

RUN NO.	MACH NO.	EJECTION DATA Q (PSI)	ELEVATOR DATA [illegible]
1	3.0	—	[illegible]
2	3.0	27.56	[illegible]
3	3.0	34.38	—
4	3.2	27.65	[illegible]
5	2.8	24.26	24.26
6	2.8	—	—
7	2.8	32.34	[illegible]
8	3.2	—	—
9	2.6	20.71	[illegible]